NORTHWESTERN UNIVERSITY

Structure, Morphology and Chemistry of Catalytic Transition Metal Oxides

A DISSERTATION

SUBMITTED TO THE GRADUATE SCHOOL
IN PARTIAL FULFILLMENT OF THE REQUIREMENTS

for the degree

DOCTOR OF PHILOSOPHY

Field of Materials Science and Engineering

By

Natasha Erdman

EVANSTON, ILLINOIS

December 2002

ABSTRACT

Structure, Morphology and Chemistry of Catalytic Transition Metal Oxides.

Natasha Erdman

Surface structures are vital for understanding a variety of technologically important processes such as catalysis, thin film growth and essentially any other reaction that occurs at the interface between a solid and a liquid or gas phase. The research approach described in this manuscript involves a combination of computational (Direct Methods) and experimental (TEM) methods for investigation of the oxide surface structures.

The NiO(111) p(2x2) structure has been solved using Direct Methods applied to grazing incidence X-ray diffraction data. The resulting structure can be described as a complex arrangement of octopolar units on the surface.

Several reconstructed and faceted $SrTiO_3$ (001) surface structures were experimentally obtained and studied by TEM. The (2x1) and the (4x2) surface structures were solved by a combination of Direct Methods analysis, HREM imaging and DFT calculations. Rules for the formation of $SrTiO_3$ surface reconstructions were formulated.

TEM and XPS experiments provided insight into changes in surface stoichiometry and morphology of the $Mg_3(VO_4)_2$ single crystal surfaces upon annealing.

ACKNOWLEDGEMENTS

First of all, I would like to thank my research advisors, Prof. L.D. Marks and Prof. K.R. Poeppelmeier, for their continuous guidance and support. I would also like to thank my committee members, Prof. M. Asta, Prof. M. Olvera, Prof. P.C. Stair and Dr. W. Sinkler, for fruitful discussions and advice.

This research project was supported by the EMSI program of the National Science Foundation and the U.S. Department of Energy Office of Science (CHE-9810378) at the Northwestern University Institute for Environmental Catalysis.

The DFT calculations presented in this manuscript were performed by Dr. O. Warschkow, Prof. D.E. Ellis and Prof M. Asta. This collaboration has proved to be very successful and productive, and I would like to express my sincere gratitude to all of the people involved in this research project.

I would like to thank Dr. R. Csencsits and J. Hiller for their wonderful reception and assistance in using electron microscope facilities at Argonne National Lab.

I would like to thank Dr. A. Barbier for providing X-ray data that was subsequently used for solution of the NiO(111) – p(2x2) structure.

Investigation of the $Mg_3(VO_4)_2$ single crystal surfaces has been a fruitful collaboration with J.D. Pless in Prof. K.R. Poeppelmeier's lab. I would like to thank him for growing single crystals that were imperative for the progress of this research, and I am also grateful for his discussion of the obtained results. I would also like to

acknowledge Dr. C.Y. Kim in Prof. M.J. Bedzyk's lab for his help with the use of XPS equipment and Dave Rowenhorst for his help with EBSD.

I would like to thank Prof. L.D. Marks, Dr. M.M. Disko and Dr. D.L. Dorset for arranging my summer internship at ExxonMobil.

I express my sincerest gratitude to the former and present members of Prof. L.D. Marks' and Prof. K.R. Poeppelmeier's groups for their guidance and help over the years - you have made my graduate school experience very rewarding.

Last, but not least I would like to thank my family and friends (here and back in Israel) for being my support net during the last 4 years. Your love and caring has always been an incredible inspiration.

CONTENTS

ILLUSTRATIONS

Figure Page

TABLES

CHAPTER 1

INTRODUCTION

The Surface Chemistry of Catalysis

A catalyst, by definition, is a substance that increases the rate at which a chemical reaction reaches equilibrium by decreasing the activation energy barrier height, without being consumed itself during the reaction. At present, catalysis is an essential process technology for the production of most chemicals and for the treatment of emissions – more than 80% of the industrial chemical processes currently used employ catalytic reactions (Thayer 1992). Suitable catalysts can allow various chemical reactions of great importance to proceed at rates high enough to allow commercial exploitation as well as environmental benefits. By choosing an appropriate catalyst, one can increase the selectivity of a given industrial process towards a more desirable or more environmentally-friendly product.

Technological progress and the industrial use of catalysts have generally outpaced our knowledge of the science behind catalytic reactions; nonetheless, major advances in the area of catalysis inspired and motivated research efforts in this field to gain a better understanding of these processes and subsequently develop more efficient catalysts. While technological developments in the area of heterogeneous catalysis have traditionally required grueling studies based on trial and error, the development of surface sensitive techniques over the last decades has allowed a more basic understanding of the

underlying catalytic processes. Moreover, the rise of fundamental surface science research has led to the discovery of new catalysts that have dramatically improved existing technology (Sinfelt 1986).

An important step in understanding a reaction on the surface of a catalytic material is to identify the catalytically active sites. This issue is particularly crucial when studying multicomponent systems such as complex transition metal oxides. The vast majority of the catalysts used in the chemical industry are oxides, with transition metal oxides being an essential element in the process of selective oxidation of hydrocarbons. From both theoretical and practical viewpoints, catalytic oxidation has been one of the most important processes in the petrochemical industry. The field reached an especially significant milestone in the early 1960's with the introduction of gas phase oxidation of propylene to acrolein and the ammoxidation to acrylonitrile over bismuth molybdate catalysts; this process provided an abundant supply of inexpensive and useful chemical intermediates (Callahan 1970). Today, catalytic oxidation is used in the production of almost all monomers used in the manufacturing of plastics, synthetic fibers and a variety of other products. The continuing decrease in the supply of cheap hydrocarbons and increase in energy costs has prompted a significant scientific effort to better understand and further develop catalytic oxidation processes. Much of this work has aimed to develop new catalytic materials based on knowledge of their surface properties. In the "Catalyst Technology Roadmap Report"[1] from a workshop held in March 1997 and

[1] http://www.chem.purdue.edu/ccr/v2020/cat.html

sponsored by the Council on Chemical Research, the U.S. Department of Energy, and the American Chemical Society, the process of selective oxidation was ranked as the most important technology for the improvement of catalytic processes. The research strategy described in this manuscript essentially targets the challenge of understanding oxidation reactions that occur on the surfaces of solid transition metal oxides by elucidating the surface structures and determining the active surface sites of various oxide materials.

The appeal of oxides for catalysis lies in their ability to take part in the exchange of electrons, as well as oxide ions and protons making them suitable for both redox and acid-base reactions. Over the years, the catalytic activity of oxide surfaces has been attributed to surface defects (including oxygen vacancies, dislocations, adsorbed species and reduced/oxidized metal atoms), but the exact nature of these defects for most oxide materials is ambiguous. Thus, prediction of the surface structure of an oxide and the governing factors in its formation has become an important frontier in solid-state inorganic chemistry. To date, comparatively little is known about the exact atomic arrangements at oxide surfaces, and there has been considerable discussion concerning the forces that control them. One of the well recognized and accepted models suggests that the dominant factor in surface rearrangement is a reduction of Coulomb forces (Wolf 1992); another model favors minimization of "dangling bonds" via charge transfer to states below the Fermi energy (Pashley 1998).

Transition metals can assume different oxidation states and coordination numbers and consequently can create versatile oxide compounds. The bulk structure and properties

of simple binary and ternary oxides are relatively well understood, with several comprehensive reviews and books available addressing the issues in terms of thermodynamics (Johnson 1982), non-stoichiometry (Sorensen 1981) and spectroscopy (Hamnett and Goodenough 1984). On the other hand, despite numerous theoretical and experimental efforts, rather little is known about the surfaces of oxides. A comprehensive review by Henrich and Cox (1994) addresses the present knowledge on structural and electronic properties of oxide surfaces, while a review by Freund, Kuhlenbeck and Staemmler (1996) provides a summary of results of observations of surface states by scanning tunneling spectroscopy (STM) and oxide thin film studies. The current work will demonstrate results obtained for several different oxide systems while discussing the importance of each material as well as its structural and electronic properties in the corresponding chapters.

Over the last several decades, a number of ultra-high vacuum (UHV)-based surface science techniques have become available for detailed investigation of surface structure on the atomic level. Low energy electron diffraction (LEED) allows identification of surface phases and their periodicities; X-ray photoelectron (XPS) and Auger electron (AES) spectroscopy allow identification of surface adsorbates and follow changes in oxidation states under reaction conditions. Recent developments in STM and atomic force microscopy (AFM) make possible observations of surface structure and morphology with atomic resolution, although in the case of oxide surfaces the interpretation of results can be somewhat ambiguous (Bonnell 1998). All of these

techniques (with the exception of AFM that can operate in air) require UHV conditions that, on one hand, provide scientists with very precise control of the surface and its environment. On the other hand, the UHV environment is very far from the industrial reaction conditions used for real catalysts, thus creating what are commonly referred to as the 'pressure and material gaps'. The 'pressure gap' has been bridged in several studies by combining single crystal analytical studies with kinetic measurements using the same instrument (Somorjai and Zaera 1982; Rodriguez and Goodman 1991). The use of single crystal surfaces in these studies enables control of the surface structure and stoichiometry and provides a feasible model system for a site or set of sites existing on a real high-pressure catalyst. There is, however, still much to be done to seal the 'material gap', i.e. relating the single crystal results to real catalytic systems that are usually used in the form of high surface area powders and metal particles on oxide support.

Transmission Electron Microscopy of Surfaces

Transmission electron microscopy (TEM) is rarely considered a surface sensitive tool of choice. Even though researchers have seen surface structure contributions to the contrast of their images for many years, it has been considered more of a nuisance and artifact than a source of viable structural and morphological information about surfaces. Nonetheless, recent developments in UHV microscopy have allowed better control over the surface composition and experimental environment, and the typical resolution of the

instrument (~2Å) makes it an ideal probe for direct imaging of atomic structure. One of the major advantages of TEM over other techniques is the opportunity it offers to obtain morphological (through bright/dark field imaging) and structural (diffraction) information simultaneously. While other electron diffraction based surface characterization techniques - LEED and reflection high-energy electron diffraction (RHEED) - are limited to only the first few layers of the specimen, transmission electron diffraction (TED) can probe surface and bulk structures, and the interaction between them, at the same time.

Images obtained using TEM can provide very useful structural information (Cowley 1986; Williams and Marks 1995). The two most common imaging techniques employed for surface studies in TEM mode are plan view and profile view imaging.

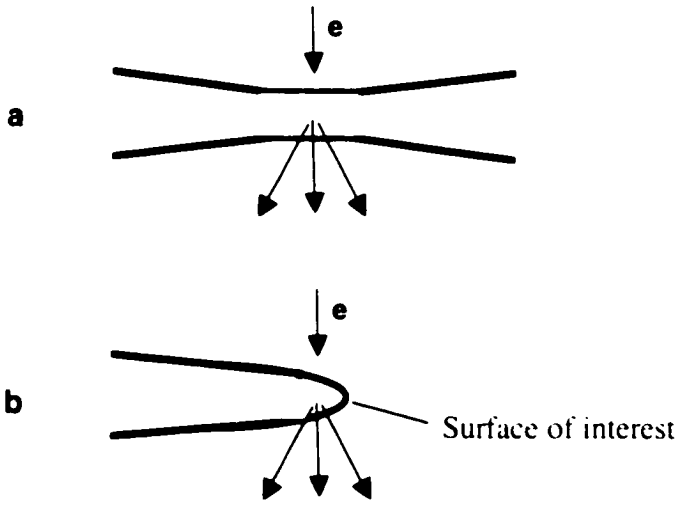

Fig. 1: HREM imaging techniques employed for surface studies: (a) plan view and (b) profile view.

In plan view imaging (Figure 1a) the top and the bottom surfaces along with the bulk material between them are probed. In this case the beam is perpendicular to the surface and the technique can be used in either the on- or off-zone axis configuration (Dunn et al. 1991; Marks et al. 1992; Erdman et al. 2002). In profile imaging (Figure 1b), the beam is parallel to the surface of interest and the structure of the side surface is revealed (Marks 1983; Marks and Smith 1983). This latter technique can be very powerful for obtaining direct images of atomic positions on the surface; however, reproducibility of the results is somewhat of an issue owing to the thermodynamical instability of a thin TEM specimen edge. Although high-resolution plan-view imaging is an excellent technique for obtaining atomic scale information about surface structure, a combination of bright field, high-resolution dark field imaging and TED can be a powerful source of additional information about the surface.

Unlike LEED and RHEED, where data analysis can get complicated because of various dynamical effects, TED can be assumed to be approximately kinematical when the sample is tilted off-zone (Tanishiro and Takayanagi 1989; Twesten and Gibson 1994) since the off-zone axis configuration significantly increases the surface signal relative to the otherwise overwhelming bulk signal. The data collection process in TED is relatively simple and fast; the diffraction patterns are recorded in series of exposures onto photographic film, yielding the intensities of the diffraction spots as well as some information about the unit cell periodicity and symmetry (Marks 1992; Xu and Marks 1992). Reduction of the diffraction data to overcome the low signal to noise ratio of the

surface diffraction intensities as well as the presence of diffuse scattering is achieved by using a cross-correlation method (Xu, Jayaram and Marks 1994). It is important to remember that TED data are two-dimensional in nature, and therefore only the atomic arrangements in the plane of the surface can be calculated. This aspect makes TED quite different from an X-ray diffraction experiment conducted in grazing incidence configuration (GIXD), where several surface layers are probed at once providing both in and out of plane information about bulk/surface relaxations (Robinson and Tweet 1992; Feidelhans'l 1989).

Over the last decade, using a combination of TED or GIXD data and Direct methods analysis (the details of the analysis are given in Chapter 2) L.D. Marks' group at Northwestern University has solved several different surface structures. Summary of these results is presented in Table 1.

The level of success achieved over the last decade in determination of various semiconductor surface structures using TED (Table 1) prompted investigations of other, more complex systems, such as mixed metal oxide catalysts, in which surface structure can play a crucial role. Knowledge of the atomic-scale structure of catalytically active surfaces and of the adsorbed reactants and intermediates under reaction conditions is crucial for an understanding of catalytic reactions at the molecular level and will subsequently create possibilities for faster development of new catalysts, improve their performance on industrial level, and lower the costs associated with processing.

Table 1a: List of surface structures solved at Northwestern University by Direct Methods in two dimensions. Structures with * were analyzed as calibration tests.

Surface structure	Type of data	Reference
Si(111) – (√3x√3)R30°Au*	Electron	Marks et al. 1997
Si(111) – (5x2) Au*	Electron	Marks et al. 1997
Si(111) – (7x7)*	Electron	Gilmore et al. 1997
Si(111) – (4x1)In	Electron	Collazo-Davila et al. 1997
Si(111) – (6x6)Au	X-ray	Marks et al. 1998a
TiO_2 (100) – (1x3)	X-ray	Landree et al. 1998
Si(111) – (3x1)Ag	Electron	Collazo-Davila et al. 1998a
Si(111) - (√3x√3)R30°Ag*	Electron	Grozea et al. 1999
Ge(111) – (4x4)Ag	X-ray	Collazo-Davila et al. 1998b
MgO(111) - (√3x√3)R30° MgO(111) - (2x2) MgO(111) - (2√3x2√3)R30°	Electron	Plass et al. 1998
Ge(111) – (3x1)Ag	Electron	Grozea et al. 1999
$SrTiO_3$(001) – (2x1)	Electron	Erdman et al. 2002a
$SrTiO_3$(001) – (4x2)	Electron	Erdman et al. 2002b

Table 1b: List of surface structures solved at Northwestern University by Direct Methods in three dimensions. Structures with * were analyzed as calibration tests.

Surface structure	Type of data	Reference
NiO(111) – (2x2)	X-ray	Erdman et al. 2000
InSb(001) – c(2x8) GaAs(001) – c(2x8) InAs(001) – c(2x8)	X-ray	Kumpf et al. 2001

It is well established that the rate-limiting step in TEM studies of single crystals and their surfaces is the specimen preparation procedure. Sample preparation requires relatively large single crystals (at least 3 mm in diameter), and involves some combination of mechanical polishing, dimpling and ion-milling (or in some cases chemical polishing) to obtain an electron transparent specimen. Oxide surfaces also require subsequent annealing at relatively high temperatures to eliminate the surface damage (due to ion-milling) and produce a well ordered or reconstructed surface. Although the annealing temperatures must typically be high enough to induce significant surface diffusion and ordering, bulk diffusion must be limited (to prevent sample coarsening); therefore, the bulk defects do not necessarily disappear as a result of the annealing process and the near surface region can be somewhat disordered compared to the surface. For instance, in a study by Dunn et al. (1992) the defect concentration

observed on the reconstructed surfaces of Ir(001), Si(111) and Au(001) samples was about 10^{11}-10^{13} cm^{-2}. Another relevant issue in the TEM studies of oxide surfaces is the possibility of radiation damage to the surface (Buckett 1991; Ai 1992); such damage can effectively change the surface composition during a TEM experiment and therefore complicate high-resolution and diffraction analysis. These issues will be addressed in further detail for each of the systems under investigation in the following chapters.

The objective of the presented work is to develop and apply the available experimental transmission electron microscopy and computational techniques to improve understanding of the surface structure and morphology of three transition metal oxide systems – $SrTiO_3$, NiO and $Mg_3(VO_4)_2$ - under different environmental conditions. While $SrTiO_3$ has little direct importance in catalysis (albeit some research has been done in the areas of photocatalysis (Mavroides, Kafalas and Kolesar 1976) and interaction of formic acid and water with $SrTiO_3$ surface (Wang 2000; Wang, Ferris and Herman 2002)), it was chosen primarily as a model system for oxides with a perovskite structure. The latter two systems have been selected specifically due to their possible catalytic application. The current work will show that, as expected, surface rearrangements in oxides are quite different from their respective bulk structures. The results also suggest that many of the concepts of bulk chemistry can be applied to surfaces when coupled with the additional constraints to minimize surface dipole moments and maximize coordination.

The following chapters will describe in detail the experimental approach that was taken (Chapter 2) and address the results obtained for each of the three oxide system

surfaces – NiO (111) in Chapter 3, $SrTiO_3$ (001) in Chapter 4 and $Mg_3(VO_4)_2$ in Chapter 5. Conclusions of these studies and suggestions for future work will be presented in Chapter 6.

CHAPTER 2

EXPERIMENTAL TECHNIQUES AND PROCEDURES

This chapter provides details of experimental procedures and various types of instruments used in this study. Transmission electron microscopy and electron diffraction were used to characterize structure and morphology of oxide surfaces. The surface diffraction (electron or X-ray) data were analyzed using Direct Methods. Additional supplemental techniques were employed to obtain surface composition (X-ray photoelectron spectroscopy (XPS)) and crystallographic information (electron backscattered diffraction (EBSD)).

TEM Sample Preparation

TEM studies were conducted on both $SrTiO_3$ and $Mg_3(VO_4)_2$ single crystals with different orientations, and the following TEM sample preparation procedure is applicable to both materials. Single crystal wafers of $SrTiO_3$ were supplied by MTI Corporation (99.9% purity); $Mg_3(VO_4)_2$ single crystals were grown by J.D. Pless using a floating zone technique (for further details see Pless et al. 2002). The single crystals were cut using an ultrasonic cutter to obtain 3mm discs, the nominal size of a TEM sample. The discs were then mechanically polished to a thickness of about 120 μm, dimpled and subsequently

ion milled with 5 kV Ar^+ ions using a Gatan Precision Ion Polishing System (PIPS) to produce an electron transparent sample.

In order to obtain a flat and reconstructed surface and eliminate ion-milling damage, the samples were annealed in a tube furnace with a flow of high-purity oxygen over the sample. In the case of $SrTiO_3$ crystals the temperature range was between 850° and 1100°C; for $Mg_3(VO_4)_2$ crystals the temperature was between 450° and 750°C. The annealing temperature was chosen to be in the range of $^1/_3$ to $^1/_2$ of the melting temperature in order to assure a significant amount of surface diffusion but limit bulk diffusion.

Several issues should be considered to assure a successful annealing experiment. A critical point to be addressed before the annealing is the cleanliness of the apparatus being used, i.e. the alumina crucible and the quartz or alumina tube. Both the crucible and the tube should be cleaned prior to annealing using an *aqua regia* solution (HCl + HNO_3), washed thoroughly with deionized water and dried using acetone. It is advisable to burn off the carbonaceous residue left on the inside of the tube at 300°C for approximately an hour prior to use. This procedure will ensure minimal contamination of the sample during the annealing.

Other points to consider are the ramp up/down rates, duration of the annealing process and adequate annealing temperature. Poorly chosen annealing conditions might cause coarsening of the TEM sample, which could result in it being too thick and thus unsuitable for a surface diffraction experiment. Sometimes such coarsening effect can actually create a very useful sample for plan-view HREM: a theoretical study by

Srolovitz (1986) showed that development of instability during the annealing can lead to formation of a thin region just behind a thick outer edge, which is ideal for TED and HREM studies (this effect has been routinely observed experimentally following the annealing). In the experiments described here the ramp up/down rate was 120°C/hr, which proved to be acceptable for making adequate thin TEM samples. A prolonged annealing time could thicken the sample as well; however, it is important to consider a need to equilibrate the surface which could also be a function of annealing time. Whereas in the case of $SrTiO_3$ crystals the surface rearrangement was governed mainly by the annealing temperature, and therefore a relatively short annealing time was used (0.5 – 3 hrs), the $Mg_3(VO_4)_2$ crystals were annealed for short and long periods of time (from 2 to 10 hrs) to study both thermodynamic and kinetic effects of the annealing process on the surface restructuring.

Surface Diffraction Analysis

Off zone-axis electron diffraction patterns, necessary for surface diffraction data analysis, along with bright-field images of $SrTiO_3$ single crystal samples were obtained using the UHV-H9000 Hitachi electron microscope at Northwestern University (Collazo-Davila et al. 1995), operated at 300kV. The H8100 Hitachi electron microscope operated at 200kV in EPIC facility at Northwestern University was used to examine the $Mg_3(VO_4)_2$ crystals.

A series of negatives with exposure times varying from 0.5 to 120 s were recorded for a particular $SrTiO_3$ surface reconstruction using strategies that were developed in the Marks' group at Northwestern University over the last decade (Xu and Marks 1992; Collazo-Davila, Grozea and Marks 1998). The negatives were digitized to 8 bits with a 25 μm pixel size using an Optronics P-1000 microdensitometer. The intensities were extracted using a cross-correlation technique (Xu, Jayaram and Marks 1994) and then averaged using specific plane group symmetry to yield independent diffraction intensities. Under the exposure conditions used the intensity readout from the microdensitometer was proportional to the true intensities of the diffraction spots.

Direct Methods Analysis

Diffraction techniques provide a powerful tool for the solution of surface structures and refinement of atomic positions; however, they require an initial model that is relatively close to the 'true' structure for the refinement to work. Information about the phases of the structure factors that is lost in a diffraction experiment is necessary to restore the charge density or scattering potential (X-ray or electron diffraction, respectively). In a diffraction experiment, the amplitudes of the reflections are recorded, but the phase information is lost, thus preventing a direct Fourier inversion of the data. The measured amplitudes allow calculation of the Patterson function (Schwartz and Cohen 1987), which provides interatomic vector information. Unfortunately a Patterson

function analysis is often problematic owing to ambiguities in picking out individual interatomic vectors and the presence of artifacts. The latter is a severe problem for surfaces where only a limited number of reflections are measured.

This problem has been solved for bulk X-ray diffraction using an approach called Direct Methods. In the last few years, our group has successfully applied the direct methods approach to 2D electron and X-ray diffraction data to solve surface structures (e.g. Marks et al. 1998; Marks, Erdman and Subramanian 2001), and more recently to 3D data (Marks 1999; Erdman et al. 2000; Kumpf et al. 2001). This approach solves the phase problem by exploiting probability relationships between the amplitudes and the phases of the diffracted beams. Effectively, a set of plausible solutions for the structure is generated, starting only from the intensity data.

The method used to obtain surface structure solution involves a minimum relative entropy algorithm combined with a genetic algorithm for global optimization (for more details, see Marks et al. 1998; Marks, Sinkler and Landree 1999). The algorithm searches for the set of phases with the lowest figures of merit (FOM). The solutions with the lowest FOMs are used to create electron density maps that obey the imposed symmetry. If the experimental errors are very small or nonexistent, these maps can approach an accurate charge density restoration. However, sometimes only a part of the structure can be identified in the initial analysis, owing to measurement errors or insufficient information on the symmetry of the structure. Final structure refinement was performed based on R-factor and χ^2 measures of agreement, defined as:

$$R = \Sigma \mid I_{meas} - I_{calc} \mid / \Sigma I_{meas} \quad (1)$$

$$\chi^2 = 1/(N-M)\, \Sigma((I_{meas} - I_{calc})/\sigma)^2 \quad (2)$$

where I_{calc} is the calculated intensity, I_{meas} the measured intensity, N the number of data points, M the number of variable parameters, and σ the measurement error.

Supplementary Techniques

Electron Backscattered Diffraction

Electron backscattered diffraction (EBSD) in a scanning electron microscope (SEM) has been routinely used as a viable technique for determination of crystal orientations in polycrystalline materials with high spatial resolution (Venables and Harland 1973; Isabell and Dravid 1997). Venables and Harland (1973) demonstrated in their experiments using a field emission SEM that the resolution limit might be as high as 20 nm laterally and 60 nm along the sample in the direction of the beam – the difference between the two figures is due to the elongation of the electron beam along the steeply inclined surface of the specimen.

Fig. 2 illustrates a general setup of the instrumentation required to collect an EBSD pattern. An electron beam in this case is stationary and incident to the surface of the sample at a glancing angle of less than 35°. This geometry is maintained to ensure a high backscattered signal coefficient. The resulting pattern is collected on a phosphorous screen or directly into a computer for direct online indexing.

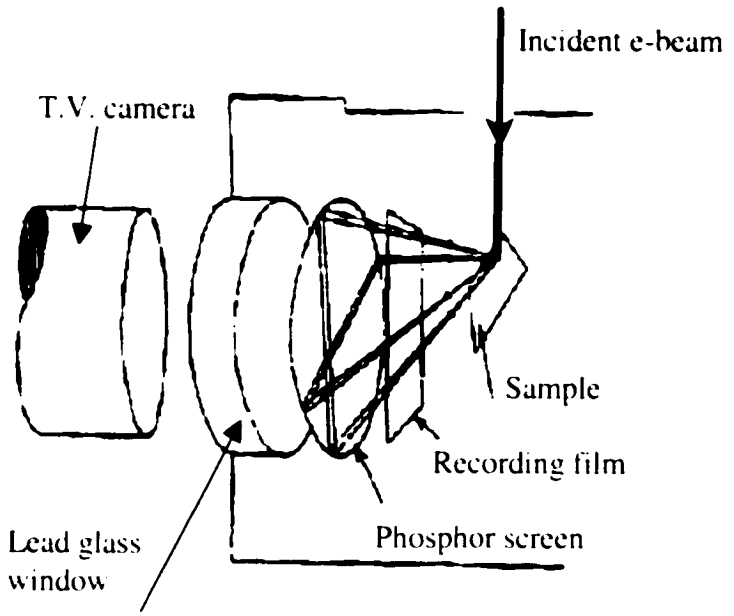

Fig.2: Schematic diagram for detection of electron backscattered diffraction (EBSD) patterns (from Dingley and Field 1997).

EBSD has been chosen in this study to determine crystallographic orientation of naturally occurring facets on $Mg_3(VO_4)_2$ single crystals. The sample preparation for EBSD is crucial since the diffraction information originates in approximately a 20 nm layer at the surface, corresponding to the penetration depth for back-scattered electrons. Naturally forming facet on the $Mg_3(VO_4)_2$ single crystals was identified by visual inspection and the crystal surfaces were polished to investigate those facets. The samples were then ultrasonically cleaned in methanol and coated with ~50 Å of carbon to prevent

charging effects in the SEM. The EBSD patterns were collected using a Hitachi S-570 SEM with a LaB_6 source equipped with TexSEM Laboratories EBSD equipment. The SEM was performed at operating voltage of 20 kV. During data analysis, first a background signal from a larger area was collected (continuous subtraction of the background signal proved to significantly improve image quality, see Dingley et al. 1987; Dingley and Field 1997). Afterwards the beam was focused on a specific area of interest and an electron back-scattered diffraction pattern was obtained. The resulting Kikuchi map was analyzed according to the known space group and crystal system of the material: the angles between the different Kikuchi lines were used to calculate the crystallographic orientation. For orthorhombic crystals, the angle between two different crystal directions can be determined using:

$$\cos\rho = \frac{a^2u_1u_2 + b^2v_1v_2 + c^2w_1w_2}{\left\{(a^2u_1^2 + b^2v_1^2 + c^2w_1^2)(a^2u_2^2 + b^2v_2^2 + c^2w_2^2)\right\}^{\frac{1}{2}}} \qquad (3)$$

where ρ is the angle; $[u_iv_iw_i]$ are the indices of crystallographic directions; a,b,c are the lattice parameters of the structure.

X-ray Photoelectron Spectroscopy

In X-ray photoelectron spectroscopy (XPS) the surface composition is examined by irradiating the sample with monochromatic soft X-rays and analysis of the detected electrons. These photons interact with the specimen in the surface region and cause the electrons to be emitted through photoelectric effect with kinetic energy of:

$$E_K = h\nu - E_B - \varphi \quad (4)$$

where E_K is the measured kinetic energy, hν the photon energy, E_B the binding energy of the atomic orbital from which electron is emitted and φ is the spectrometer work function. The photo-electrons can only escape from the near surface region of the sample, therefore they carry chemical information specific to the top few atomic layers. Since each element has a unique set of binding energies, XPS technique can be used to identify the elements on the surface of the specimen and their respective concentrations.

XPS setup in Prof. M. Bedzyk's lab (hemispherical PHI Model 10-360 Precision Energy Analyzer) has been used to analyze the surface composition of $Mg_3(VO_4)_2$ single crystals after various annealing experiments with the help of Dr. C.Y. Kim. Al Kα (1486 eV) X-rays were used for analysis, with typical scan step size of 0.5 eV.

CHAPTER 3

SOLUTION OF THE p(2x2) NiO (111) SURFACE STRUCTURE USING DIRECT METHODS

The NiO (111) surface is known to exhibit important physical and chemical properties - NiO is antiferromagnetic at low temperature (Men'shikov et al. 2000) and a catalytic compound (Christoskova et al. 1995; Mitsui et al. 1999). The alternating layers of Ni^{2+} and O^{2-} ions produce a non-vanishing dipole moment perpendicular to the surface, resulting in an unstable bulk terminated NiO (111) polar surface with a nominally infinite surface energy (Bertaut 1958). Theoretical calculations for ionic crystals with NaCl-type structures have predicted two similar solutions to this problem: either the clean unreconstructed (111) surface will facet into neutral {100} type planes upon annealing, or a reconstruction of the surface will occur (i.e. faceting on an atomic scale) (Gibson, Haydock, and LaFemina 1992). Some of these results (Shi and Wortis 1988; Wolf 1992) indicate a possible 'octopolar' termination of the NaCl (111) surface, which should be stable at zero temperature. The basic structural unit of such a surface will be a simple cubic $(NaCl)_4$ octopolar unit, instead of the conventional face-centered cubic (fcc) lattice with a dipolar Na^+-Cl^- basis (see Fig. 3). Using atomistic modeling techniques, Oliver, Parker and Mackrodt (1993) investigated the changes in NiO surfaces energy with respect to surface oxidation (i.e. concentration of Ni vacancy/electron hole aggregates). They

found an oxidized nickel-terminated NiO (111) surface to be energetically more stable than an unoxidized surface.

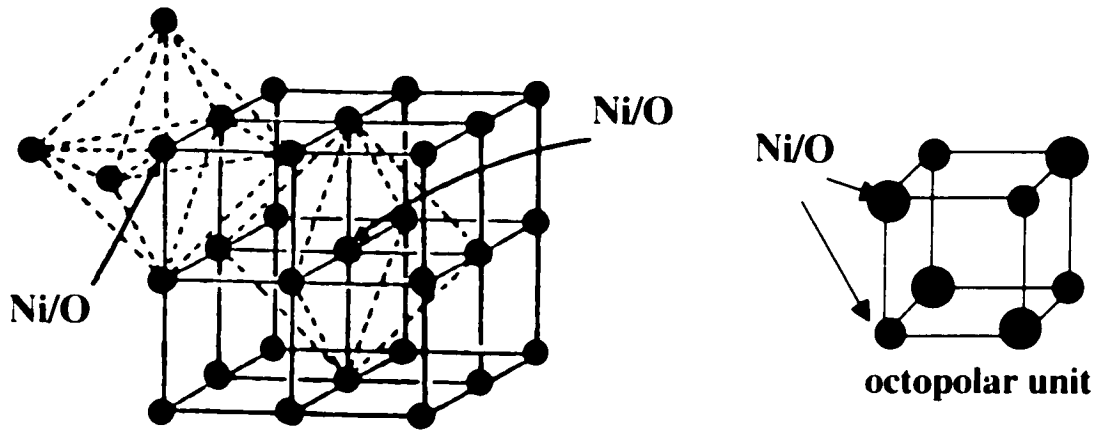

Fig. 3: Bulk structure of NiO and a typical octopolar unit.

Recent investigations indeed indicate that a stable NiO (111) surface can be obtained experimentally. Ventrice et al. (1994) reported a stable p(2x2) reconstruction for NiO films grown on Au (111) at 550 K using LEED and STM. The STM images showed a stable reconstruction characterized by relatively flat (corrugation <0.2 Å) terraces with a step height of ~2.4 Å and several missing-atom point defects. The images showed features that were interpreted as micropyramidal structures (three-atom clusters with the atom of opposite charge located above each cluster) on the surface; however, the authors were not able to conclude whether the micropyramids were oxygen- or nickel-terminated. Barbier et al. (1999, 2000) investigated the p(2x2) NiO (111) reconstruction on both a single crystal surface and a 5 monolayer thick NiO (111) thin film grown on Au (111)

using GIXD. For a single crystal p(2x2) reconstructed surface, the authors proposed a model with a Ni-terminated octopolar reconstruction and double steps. The thin film exhibited different structural features and the proposed model had an equal combination of Ni-terminated and O-terminated octopolar terraces on the surface separated by single steps, leading to coexistence of two different surface phases. Unfortunately, the thin film reconstruction model contradicts the previous STM results by Ventrice et al. (1994) that showed a single structure. Furthermore, as will be discussed in more detail below, we were unable to reproduce their reported fit to the experimental data.

Here direct methods were applied to determine the atomic structure of the p(2x2) surface using the thin-film GIXD data obtained by Barbier et al. (2000). First principles density functional (DF) calculations were carried out by O.Warschkow on the proposed surface structure in order to understand the local electronic properties and these were compared to similar calculations on atomistically relaxed octopolar reconstructions with Ni- and O-termination. For the detailed description of the DFT calculations and discussion of the electronic structure of the p(2x2) surface refer to Erdman et al. (2000).

Methodology

For this analysis, the X-ray diffraction data collected for the NiO (111) film grown on an Au (111) surface were used. Details of the sample preparation and the collection of the GIXS data have been reported elsewhere (Barbier et al. 2000). A total of 25 independent intensities in the two-dimensional *p6mm* (Patterson) plane group and in

3-D 296 independent reflections in *p3m1* symmetry were considered for the direct methods calculations. Since *p6mm* Patterson symmetry may correspond to *p3*, *p3m1*, *p31m* or *p6mm* plane group symmetries, all of those were considered in the calculations.

Full 3D Direct Methods calculations were also performed, followed by refinement by replacing peaks in the maps with atoms and allowing the positions of these atoms to vary. In the final step, the atomic positions were refined using the least-squares method with the SHELX-97 program (Sheldrick 1997). The agreement between the measured and calculated intensities was calculated using two different parameters. The R-factor is defined as:

$$R = \Sigma| |F_o| - |F_c| |/\Sigma|F_o| \quad (5)$$

where F_o is the measured structure factor, F_c is the calculated structure factor. In addition, the χ^2 value was calculated:

$$\text{Goodness of Fit} = \chi^2 = \{\Sigma[\ w(F_o^2-F_c^2)^2\ ]/(n-p)\} \quad (6)$$

where n is the number of reflections and p is the total number of parameters refined. The effect of lattice vibrations on the diffracted beam amplitudes, and therefore on the final solution, was included in the final steps of the refinement fixing the Debye-Waller factors for the subsurface atoms to those of the NiO crystal lattice. Isotropic Debye-Waller factors for NiO which have previously been determined via a polynomial expansion with temperature (Gao, Peng, and Zuo 1999) in the form:

$$B(T)=a_0+a_1T+a_2T^2+a_3T^3+a_4T^4 \quad (7)$$

where T is in Kelvin, B is given in Å, and a_i are polynomial fitting parameters, were used in the calculation. The temperature factors used here were calculated for 300K.

A few points need to be made about the experimental data, which in raw form was the same as that used previously by Barbier et al. (1999, 2000). We received three X-ray diffraction data sets from Dr. Barbier for the (2x2) reconstruction of NiO (111) surface. The first set was data from a single crystal surface reconstructed after annealing in air. According to Dr. Barbier, only the in-plane measurements were reliable, a total of 16 reflections. The second data set (a single crystal after UHV annealing) consisted of 9 in-plane and 39 out-of-plane reflections (the latter were not averaged and were collected along only 2 different rods). Neither of these two data sets contained enough reflections to be used to attempt a structure determination. The third data set (a 5ML NiO (111) thin film grown on Au (111)) was the most complete with 321 measurements, and the results of the Direct Methods calculations for this data set are presented here (for the complete dataset see Appendix I). The two-dimensional symmetry of NiO (111) is *p3m1*, so the Patterson symmetry (i.e. the symmetry of the intensities) should be *p6mm* in the plane; the 3D symmetry is P3(bar)m1. The raw data contained large deviations from this required symmetry, which we averaged out by applying the required symmetry operations. (Even if the surface is of lower symmetry, then it is impossible not to have the full symmetry in the intensities, unless there is strong preference for a particular domain owing to a miscut surface.) It should be noted that the use of *p3m1* symmetry for intensity data analysis as was done by Barbier et al. (1999, 2000) is incorrect.

Surface Structure Solution and Discussion

The charge density maps calculated using 2D diffraction data showed plausible solutions only for the *p3* and *p3m1* plane groups (see Fig. 4). Full 3D calculations were performed for both of these groups and are shown in Fig. 5. The data set (296 independent reflections) was refined using 21 parameters to describe the model. The corresponding R-factor is 0.17, and the χ^2 value is 1.82. The top surface layer is nickel-terminated, with $^3/_4$ of the nickel atoms missing, the next (oxygen) layer is completely full, and the third (nickel) layer has $^1/_4$ of its nickel atoms missing. Atomic positions for both Ni and O are shown in Table 2, and the final model for the p(2x2) surface structure is presented in Fig. 6. The surface atoms exhibited only very small relaxation from bulk interatomic distances. The surface layer Ni-Ni distance is 2.9±0.1Å, and the Ni-O distance 2.0±0.1Å. The bond angles are almost exactly the same as in the bulk structure.

Comparison between the experimental and calculated intensities for various diffraction rods is shown in Fig. 7. Note that for some of the rods (e.g. –45L), the intensities observed close to the origin were relatively small; application of an appropriate scaling factor for the intensities in this case has some justification and would have improved the fit (we did not attempt to rescale the rods). We attempted to reproduce the fit reported by Barbier et al. (2000) to the (same) experimental data using octopoles, using both the standard SHELX code as well as the Rods code. While it was possible to obtain a reasonable value for χ^2, the R-factor was exceedingly high (about 0.7) even when domains of Ni and O terminated octopoles were considered. With large experimental errors, it is possible to overfit weak intensities and poorly fit the strong ones

obtaining a misleadingly small value of χ^2 but a large value for the R-factor. All refinement attempts using the octopole atomic locations as a starting point were completely unstable and led to major changes in the atomic positions. It can be concluded that the good fit previously reported by Barbier et al. (2000) is an error, probably due to incorrect treatment of the symmetry requirements.

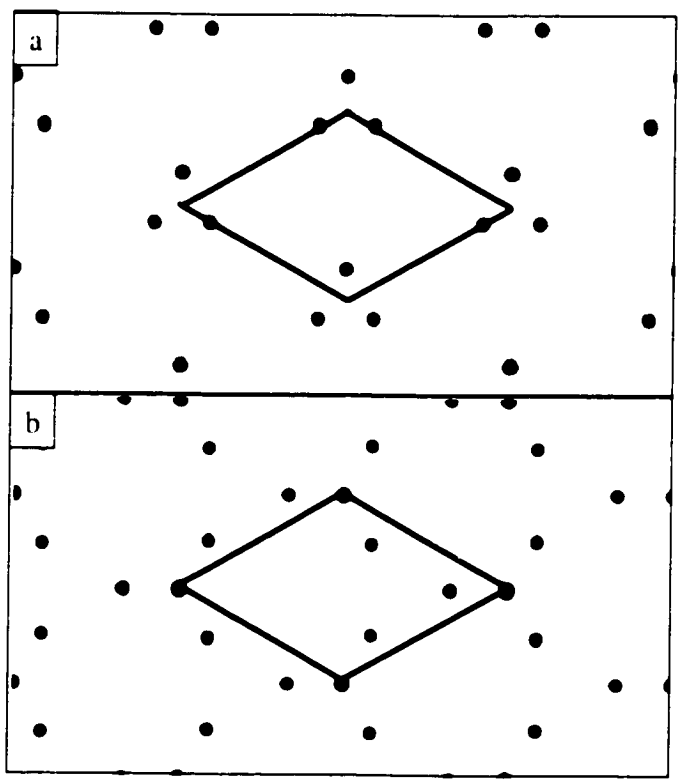

Fig. 4: Charge density maps calculated using the 2D code corresponding to (a) *p3* and (b) *p3m1* symmetries. The primitive unit cell is indicated with solid lines (a=b=5.8970Å, γ=120°). Black regions correspond to high charge density, possible atoms locations.

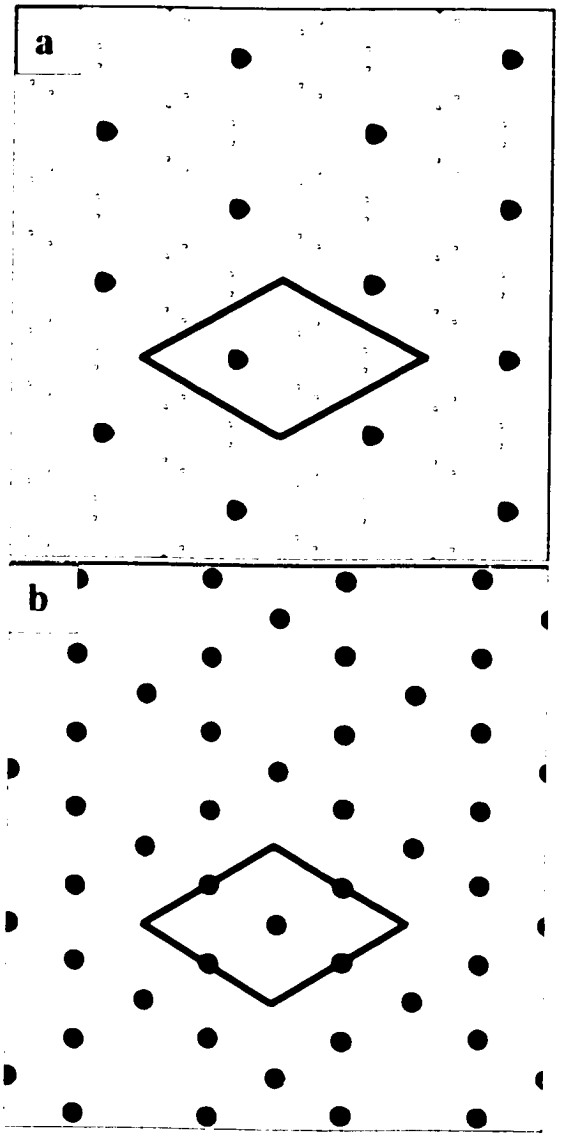

Fig. 5: Contour maps obtained using the 3D code for *P3m1* symmetry. Shown are two out of 39 'slices' along the z-axis, separated by 2.257Å; (a) shows the top (1st) Ni layer with ¾ of the Ni atoms missing, and (b) shows the underlying (3rd) Ni layer with ¼ of the Ni atoms missing. The primitive unit cell is indicated with solid lines (a=b=5.8970Å, γ=120°). The dense contour regions (black) are the sites of the Ni atoms.

Table 2: Atom positions for the solution in terms of p(2x2) unit cell in *p3m1* plane group with a=b=5.8970 Å, c=72.226Å, $\alpha=\beta=90°$, $\gamma=120°$.

Layer	Atom	x	Y	z (Å)
1 (surface)	Ni1	*2/3*	*1/3*	*0*
2 (surface)	O1	*1/3*	*2/3*	-1.2109(4)
	O2	0.3160(120)	0.1580(60)	-0.6313(4)
3 (surface)	Ni2	0.5008(5)	0.4992(5)	-2.2951(5)
4 (bulk)	O3	*2/3*	*1/3*	-3.4457(9)
	O4	0.1640(30)	0.3290(60)	-3.4992(8)
5 (bulk)	Ni3	*1/3*	*2/3*	-4.7388(4)
	Ni4	0.3261(7)	0.1631(4)	-4.6831(4)
6 (bulk)	O5	*0*	*0*	-5.5429(5)
	O6	0.4895(18)	0.5105(18)	-5.4295(3)

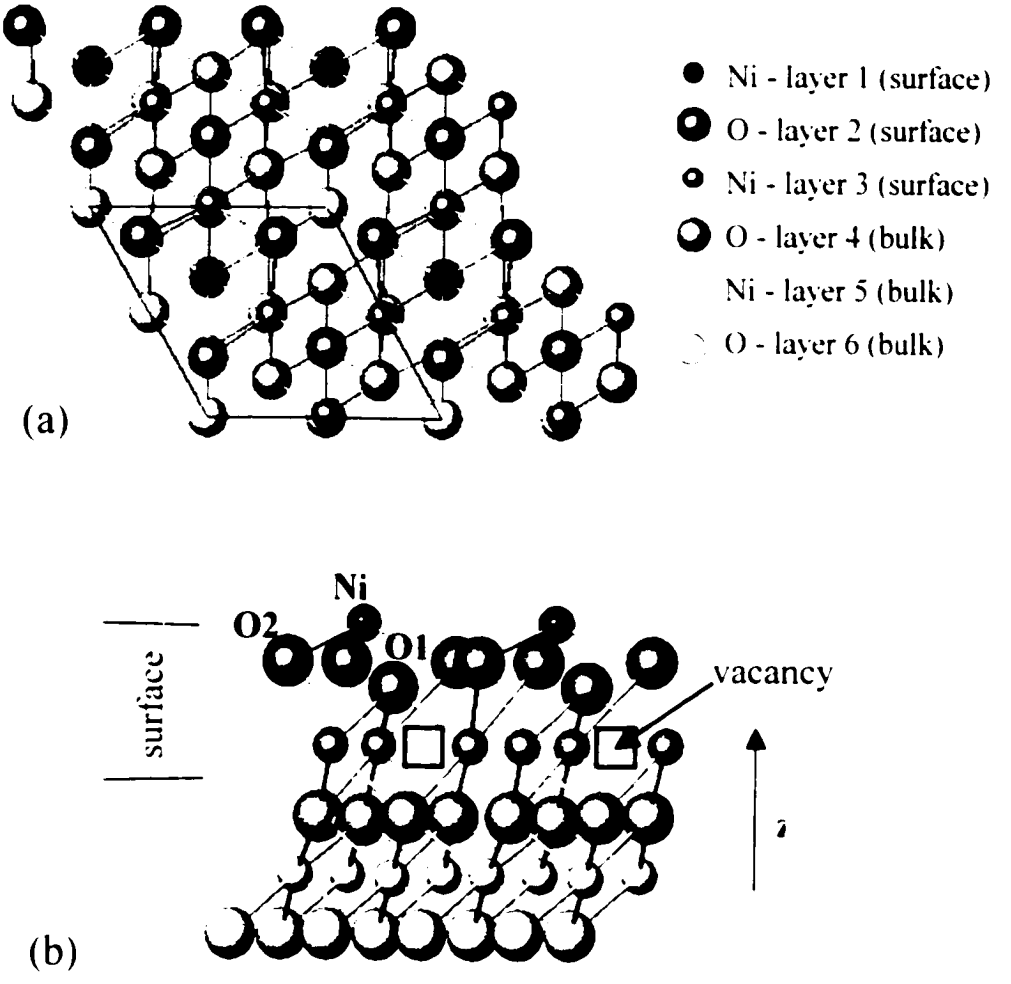

Fig. 6: (a) Top view of the p(2x2) NiO(111) surface structure obtained by Direct Methods analysis. (b) Side view of the structure. The solution is characterized by ¼ of the Ni atoms removed from the second layer and put on the surface in a 2x2 configuration (Schottky defect formation).

If one considers our reconstruction to be made up solely of Ni^{2+} and O^{2-} building blocks, simple charge accounting reveals that 4 electrons per p(2x2) surface unit would have to be removed from the system in order to attain a zero surface charge. Formally, this charge balance can be accomplished by raising the oxidation state of four atoms per surface unit, e.g. Ni^{2+} to Ni^{3+} or O^{2-} to O^{-}, as has been done in recent empirical potential models of the NiO (111) surface reconstruction (e.g. Oliver, Parker and Markrodt 1993). However, in a more adequate description, the distribution of these surface holes around surface atoms is more "fluid", with non-integer changes in partial atomic charges. Insights into the peculiarities of this distribution can be gained from electronic structure calculations performed by Dr. O. Warschkow. The calculated partial atomic charges and magnetic moments for the surface slab model are listed in Table 3. One can see that charges and magnetic moments in the deep layers are almost identical to those calculated for the bulk. The surface effects are localized in the top five atomic layers, with the two oxygen atom types (O1 and O2) in the second layer exhibiting large reductions in ionicity and surprisingly large magnetic moments, especially on the comparatively exposed O1 site. Thus, it appears that the electron holes required to neutralize the surface are located largely on the oxygen atoms in the second layer, opening up the formally closed shell of the oxide anion and revealing magnetic polarization in the process. The Ni atom in the top layer (Ni1) – sited exposed on top of a triangle of oxygen atoms (O2 sites) – also exhibits a fair reduction of its partial charge.

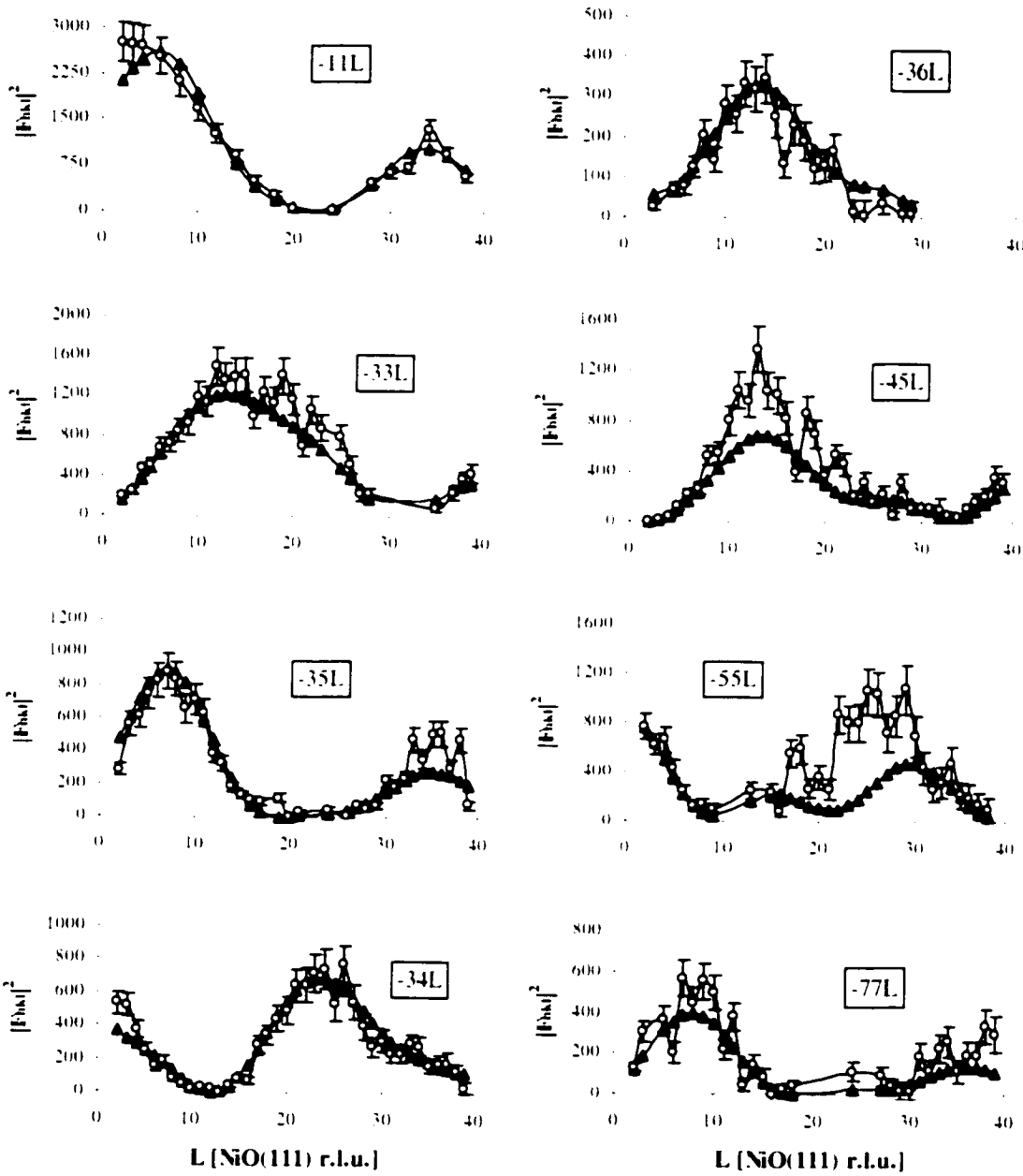

Fig. 7: Comparison of measured (○) and calculated (▲) intensities for various diffraction rods for the p(2x2) reconstruction. The *h* and *k* indices are expressed in the (2x2) r.l.u.

Table 3: Calculated partial charges and magnetic moments for the Schottky-defect NiO (111) p(2x2) reconstruction.

Layer	Atom		Charge / e (Moment / μ_B)	
1 (surface)	Ni1	(1x)	+1.37	(+1.24)
2	O1	(1x)	-1.19	(-0.83)
	O2	(3x)	-0.83	(-0.60)
3	Ni2	(3x)	1.59	(-1.59)
4	O3	(1x)	-1.67	(+0.12)
	O4	(3x)	-1.56	(+0.10)
5	Ni3	(1x)	+1.80	(+1.55)
	Ni4	(3x)	+1.83	(+1.76)
6	O5	(1x)	-1.75	(-0.01)
	O6	(3x)	-1.72	(-0.04)
7	Ni5	(1x)	+1.75	(-1.72)
	Ni6	(3x)	+1.73	(-1.72)
8	O7	(1x)	-1.73	(+0.01)
	O8	(3x)	-1.73	(+0.01)
9	Ni7	(1x)	+1.74	(+1.71)
	Ni8	(3x)	+1.73	(+1.71)
Bulk	Ni		+1.73	(±1.71)
Bulk	O		-1.73	(±0.00)

We suggest that this effect is largely due to an increased covalence, since the Ni1 atom has lost three out of six of its nearest oxygen neighbors. Through increased covalence Ni1 effectively gains electrons, largely at the expense of the O2 site. This is evident from the comparison between the partial charges of O1 and O2 sites – the O2 site has a smaller partial charge than the O1 site (-0.83 vs. -1.19 e). The third (Ni2), fourth (O3, O4) and fifth (Ni3, Ni4) layers show significantly smaller fluctuations in charges and moments of atoms. For example, Ni2 has a complete set of six nearest oxygen neighbors, thus its partial charge is only slightly reduced with respect to the bulk (+1.59 vs. +1.73 e) and its electronic structure is very close to that of Ni in bulk NiO.

Similar DFT electronic structure calculations as well as atomistic simulations were performed on the Ni- and O-terminated octopolar reconstructions proposed by Barbier et al. (1999, 2000). Calculated partial atomic charges and magnetic moments for the first few atomic layers of Ni- and O-terminated octopolar reconstructions are listed in Table 4. In comparison to what was found for our solution (Table 3), the calculated atomic charges for the octopolar surfaces exhibit a considerably smaller surface effect. No electron holes are required for charge neutrality of these surfaces and the only surface effects are due to changes in degree of covalence and charge transfer between atoms due to reduced coordination or changes in bond lengths.

Moreover, the calculated geometries for Ni- and O-terminated octopolar reconstructions are very similar, and for further discussion only the Ni-terminated octopolar reconstruction is presented. The relaxed positions for the resulting structure are presented in Table 5.

Table 4: Atomic partial charges and magnetic moments (in brackets) calculated for the top five layers of atomistically relaxed Ni- and O-terminated octopole reconstructions.

	Ni-terminated				O-terminated			
Layer	Element		Charge/e (Moment/μ_B)		Element		Charge/e (Moment/μ_B)	
1	Ni1	(1x)	+1.49	(+0.89)	O1	(1x)	-1.53	(+0.33)
2	O2	(3x)	-1.60	(-0.11)	Ni2	(3x)	+1.60	(+1.20)
3	Ni3	(1x)	+1.82	(-1.33)	O3	(1x)	-1.67	(+0.18)
	Ni4	(3x)	+1.59	(-1.32)	O4	(3x)	-1.65	(-0.08)
4	O3	(1x)	-1.72	(-0.19)	Ni3	(1x)	+1.73	(-1.67)
	O4	(3x)	-1.67	(-0.04)	Ni4	(3x)	+1.69	(-1.36)
5	Ni5	(1x)	+1.74	(+1.70)	O5	(1x)	-1.71	(+0.12)
	Ni6	(3x)	+1.74	(+1.65)	O6	(1x)	-1.71	(+0.11)

Table 5: Atomistically relaxed atom positions calculated for the Ni-terminated octopole structure in terms of p(2x2) unit cell in *p3m1* plane group with a=b=5.8970 Å, c=40.0 Å, $\alpha=\beta=90°$, $\gamma=120°$.

Layer	Atom		x / frac	y / frac	z / Å
1	Ni1	(1x)	*0*	*0*	0.000
2	O2	(3x)	0.306	0.153	0.829
3	Ni3	(1x)	*2/3*	*1/3*	1.194
	Ni4	(3x)	0.160	0.320	2.050
4	O3	(1x)	*0*	*0*	3.166
	O4	(3x)	1.023	0.511	3.033
5	Ni5	(1x)	1/3	2/3	4.269
	Ni6	(3x)	0.829	0.658	4.214

The Ni-terminated octopolar structure exhibits significantly reduced Ni3-O2 bond length (1.9 Å) as well as much expanded Ni3-O4 bond length (2.6 Å). Closer inspection of the structure reveals that in the third layer Ni3 and Ni4 atoms exhibit significant splitting in z direction with Ni3 almost merging into the second (O2 atoms) layer. These rather large changes in the atomic positions away from those reported by Barbier et al. (1999, 2000) support the conclusion based upon fitting of the intensity data that simple Ni- or O-terminated octopoles are not the correct structure of this surface.

Our proposed reconstruction is very simple and can be characterized by alternating close-packed layers of oxygen and nickel atoms. The top surface layer is nickel-terminated, with $^3/_4$ of the nickel atoms missing, the next oxygen layer is completely full, and the third (nickel) layer has $^1/_4$ of its nickel atoms missing. This structure can also be described in terms of defect chemistry: consider an oxygen-terminated bulk NiO (111), then introduce a Schottky type defect into the lattice using $^1/_4$ of the available Ni^{2+} sites in the next close-packed layer; i.e., create a vacancy by removing one positive ion (Ni^{2+}) and placing it on the surface.

This structure exhibits the features observed by the STM study (Ventrice et al. 1994) - several missing-atom point defects and a nanofacet structure (with in effect three {100} type facets) created by the octopolar units on the surface (Fig. 8).

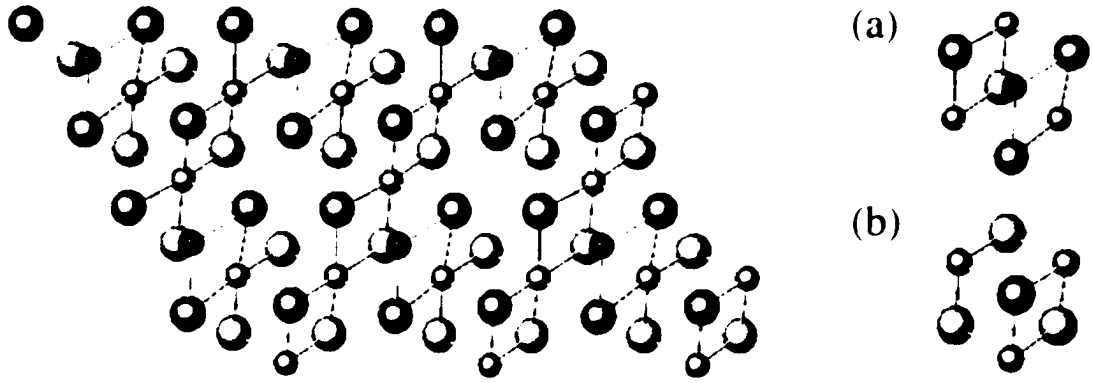

Fig. 8: Top view of the p(2x2) NiO(111) reconstruction with only top three (surface) layers shown (the structure is rotated 6 deg. about *z*-axis from configuration in Fig. 5). The surface can be constructed using (a) Ni-terminated and (b) O-terminated octopolar blocks.

The STM images showing atomic trimers in a (2x2) arrangement were taken at a negative sample bias (Ventrice et al. 1994); i.e., electrons tunneling from the sample to the STM tip, thus imaging - as conventional wisdom holds - the valence- (oxygen-) band. This observation is consistent with the oxygen trimer underneath a single nickel atom in our structure. At lower negative bias only a single atom is visible which corresponds to the exposed single Ni atom in the top layer of the surface.

Our surface structure differs in some aspects from other (2x2) reconstructions reported in the literature for NaCl-type polar oxide surfaces, specifically from the atomically facetted octopole surface structures (Shi and Wortis 1988; Wolf 1992). In particular, this reconstruction is clearly different from the coexisting Ni- and O-terminated octopolar reconstructions proposed by Barbier et al. (1999, 2000) through

Patterson analysis of the thin film GIXD data. The nearly identical surface energies and atomic positions from the atomistic model for Ni- and O-terminated octopolar reconstructions are in support of the coexisting octopolar surface model; however, it appears to be contradicted by the STM observation of a single-phase material (Ventrice et al. 1994). It should be pointed out, that the strong vertical displacement of the Ni3 layer away from Ni4 towards the O2 layer (for Ni-termination, and similar for O-termination), is not observed in the experimental relaxations found by Barbier et al. (2000). As will be argued below, we consider the merging of Ni3 and O2 layers an important aspect of structural stability.

It is well established that one of the driving forces behind surface reconstruction is that the surface seeks to minimize its internal energy, which in an ionic material is largely of electrostatic origin. The octopolar model is largely based on the argument that a simple cubic, or 'octopolar', arrangement of eight atoms (two sets of four atoms each of opposite charge, see Fig. 3) has a rapidly decaying interaction potential with other octopoles (Wolf 1992). Octopolar model presents a solution to the Madelung problem (Madelung 1919), i.e. the divergence of Coulomb potential associated with r^{-1} term (where r is the distance between two ions); Wolf (1992) calculated that the interaction between complete octopolar units given by effective Coulomb potential decays as r^{-5} at zero temperature. The {100} faceted octopolar reconstructions proposed in the literature (Wolf 1992; Barbier et al. 1999, 2000) for the NiO (111) surface are based on that model. A stability argument for the present Schottky-defect surface has to address the fact that it is constructed not only from $(NiO)_4$ building blocks but also some "left-over" atoms. In

addition, this surface is characterized by the presence of electronic defects (electron-holes) near the surface. The precise location of these (positively charged) electron holes is clearly very relevant to any discussion of electrostatic stability.

Interesting in this context is that the atomistically relaxed octopolar reconstruction has the Ni3 site vertically relaxed towards the second O2 layer. This being the case, one may consider Ni4 forming its own separate layer, while Ni3 almost merges into the O2 layer; i.e., the stacking is more adequately described as Bulk–Ni_4–O_4–Ni_3–(Ni_1O_3)–Ni_1 as opposed to Bulk–Ni_4–O_4–Ni_4–O_3–Ni_1. The merit of such a reformulation is that now the electrostatics of the Ni-terminated octopolar reconstruction can be directly compared to that of our reconstruction, which is characterized by the stacking sequence …–O_4–Ni_4–O_4–Ni_3–(O_4+4h)–Ni_1. In this, 4h denotes the presence of the 4 electron holes required for charge neutrality, which were found to be located in the second layer (see above). A comparison of electrostatic stability is possible because the stacking of these two reconstructions differs only in the second layer, where a (Ni_1O_3) stoichiometry is replaced by (O_4+4h), both having the same formal net-charge of –4. This kind of stacking of charged layers, although idealized, suggests a high degree of stability since all dipole components perpendicular to the surface vanish. Clearly, this electrostatic model is very simplified and idealized; however, we believe it provides a simple explanation for (a) the displacement of Ni3 atoms towards the O2 layer in the Ni-terminated octopolar reconstruction, (b) electron holes being located in the second (oxygen) atom layer of our reconstruction, and thus (c) suggests that our Schottky-defect surface structure and the octopolar reconstruction may be comparable in terms of electrostatic stability.

In conclusion, we find the termination of thin film NiO (111) by direct methods analysis of GIXD data, to be single-phase, Ni-terminated, and cation deficient with ¾ of top layer and ¼ of third layer atoms vacant. This reconstruction differs from the previously proposed two-phase octopolar reconstruction model (Barbier et al. 1999, 2000), but is in better agreement with the STM study of Ventrice et al. (1994).

CHAPTER 4

SOLUTION OF THE $SrTiO_3$ (001) SURFACE STRUCTURES USING TEM

$SrTiO_3$ is considered a standard model for oxides with a perovskite structure, perhaps the most studied class of oxides. Perovskites exhibit a remarkable range of compositions and structures (Mitchell 2002). They exhibit outstanding electrical properties such as colossal magnetoresistance and high-temperature superconductivity and include ferroelectric materials and high-dielectric constant materials. $SrTiO_3$ has been used as a substrate for epitaxial growth of superconducting thin films (Aruta 2001) and as a buffer layer for the growth of GaAs thin films on Si (Droopard et al. 2001). An excellent review of the literature on bulk properties of strontium titanate and its single crystal growth was conducted by Nassau and Miller (1988). The structure of $SrTiO_3$ can be described as a close-packed lattice of oxygen and strontium in a 3:1 ratio, with titanium in the octahedral interstitial sites (Fig. 9). For an ideal, bulk-terminated (001) surface, two configurations are possible: (a) Ti and O termination with a ratio of 1:2 (TiO_2 stoichiometry); or (b) Sr and O termination with a ratio of 1:1 (essentially SrO). However, since the valence and coordination numbers of transition metal oxides typically depend on environmental conditions (atmosphere, pressure and temperature), the picture becomes rather complicated. A large number of studies in recent years have used numerous surface science techniques in an effort to understand and determine surface structure variations in $SrTiO_3$ (001) under different experimental conditions and using

numerous available surface science techniques. A summary of literature results is presented in Table 6.

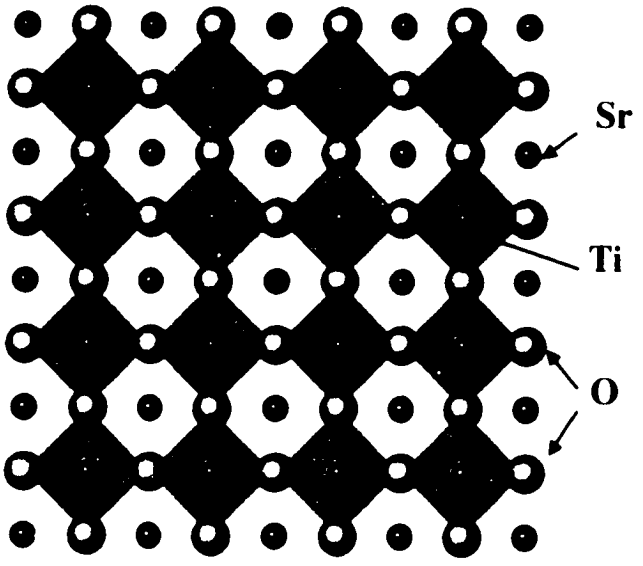

Fig. 9: Bulk structure of $SrTiO_3$ (a=3.905Å) viewed along (001) direction.

The results obtained by different groups are inconclusive and sometimes contradictory, and only a few of the studies have attempted to support their results with a feasible model for the surface structures. Cord and Courths (1985) investigated $SrTiO_3$ surfaces annealed in UHV and oxygen atmosphere by photoemission spectroscopy, LEED and Auger spectroscopy (AES). The oxygen annealed structures determined by LEED (2x1 and 2x2) were thermodynamically stable and stoichiometric; their electronic stability was attributed to formation of the Ti^{+3}-O vacancy complexes on the surface, in effect creating a TiO_x-rich surface. In STM and AFM studies, Liang and Bonnell (1993,

1994) observed that upon UHV annealing, a rearrangement of surface atoms results in the formation of row-like structures with spacing of 12 and 20Å. The authors proposed two structural reorganization mechanisms: (a) the formation of new phases on the surface upon reduction, accompanied by changes in the composition and geometry of the surface; and (b) an alteration of the surface morphology due to a reordering of oxygen vacancies. They attributed the observed ordering of the surface to an SrO-rich surface and to the formation of the so-called Ruddlesden-Popper phases (Ruddlesden and Popper 1958). This conclusion was based on an assumption of different sublimation rates for Sr, Ti and O at the surface, i.e. TiO_x has a higher sublimation rate than SrO at high temperatures in vacuum.A more recent AFM study by Szot and Speier (1999) suggested that oxidation above 900°C can also cause the $SrTiO_3$ (001) surface to become SrO-rich. These conclusions were based on measurements of step heights (consistent with unit cell dimensions of several Ruddlesden-Popper phases) from AFM images. The authors proposed that under oxidizing conditions at high temperatures, the near-surface region reconstructs via dismantling, transport and intercalation of SrO layers combined with a crystallographic shearing mechanism.

Other studies suggest that the vacuum annealed surface is depleted in SrO and is primarily covered by TiO_2 planes (Jiang and Zegenhagen 1996, 1999; Matsumoto et al. 1994). Jiang and Zegenhagen (1996, 1999) used STM to observe a well-ordered and atomically flat surface after annealing in vacuum at different temperatures. In the same experiment a change in Auger peak intensity ratios (O-to-Ti and Sr-to-Ti) was observed

Table 6: Summary of results obtained by different groups for different $SrTiO_3$ (001) surface reconstructions.

Surface structure	Sample Preparation	Reference
(1x1)	UHV annealing, T=1100K, 60 min	Cord et al. 1985; Nishimura et al. 1999; Liang et al. 1993, 1994; Jiang et al. 1999
(2x1)	1) Annealing in 10^{-5} mbar O_2	Cord et al. 1985
	2) UHV annealing, T=950°C, 2 hr	Jiang et al. 1999
	3) UHV annealing, T=600-800 °C,30 min	Castell 2002; Jiang et al. 1995
(2x2)	1) Annealing in 10^{-5} mbar O_2	Cord et al. 1985; Nishimura et al. 1999
	2) UHV annealing at 1200°C	Matsumoto et al. 1992
c(4x2)	UHV annealing in 10^{-5} mbar H_2, T=950°C 2 hr	Jiang et al. 1999; Castell 2002a, 2002b
c(6x2)	O_2 annealing, T=1100°C, 3 hr; followed by UHV annealing, T=950°C, 2 hr	Jiang et al. 1995, 1999; Castell 2002a, 2002b
(√5x√5)R26.6°	1) UHV annealing, T=900°C, 15hr; then flashing at T=1200°C, 2 min	Matsumoto et al. 1994
	2) UHV annealing, T=830°C, 120min	Martin-Gonzalez et al. 2000

for the 2x1, 4x2 and 6x2 surface structures. The Auger spectroscopy results suggested that the reconstruction with larger size unit cell tends to be richer in Ti. Further observations showed the existence of domains rotated by 90° with respect to one-another as well as formation of single unit cell high steps on the surface. In the same experiment a change in Auger peak intensity ratios (O-to-Ti and Sr-to-Ti) was observed for different surface structures. Formation of $Sr_{n-1}Ti_nO_{3n-1}$ - type phases on the surface was suggested as a possible explanation of the features obtained in STM images (Jiang and Zegenhagen 1996, 1999). The authors also proposed that the final structure of the surface is determined by two competing processes – bulk oxygen diffusion and oxygen desorption from the surface.

Castell (2002) used chemical etching and/or argon ion sputtering and subsequent UHV annealing to obtain 2x1, 4x2 and 6x2 structures on the $SrTiO_3$ (001) surface. The surface, inspected by LEED and STM, showed large surface steps with 0.4 nm step height. The author proposed a structural model based on a qualitative interpretation of the STM images, in particular step height measurements and periodicities of the surface features. The models for different structures are simple modifications of the bulk-like TiO_2-terminated surface: for each of the models the author proposed a removal of one or several rows of Ti atoms to match the periodicity observed in the STM images, in fact creating variations in surface stoichiometry (e.g. Ti_2O_3 for the 2x1 surface, TiO_2 for the 4x2 surface). The model suggests that the surface possesses an essentially a TiO_2

stoichiometry. Castell (2002a, 2002b) rejected the idea that impurity segregation is a governing factor in the formation of various $SrTiO_3$ surface structures.

Alongside the numerous experimental studies, a few researchers have presented theoretical calculations for the $SrTiO_3$ (001) surface, mainly addressing the issues of surface electronic band structure and surface relaxation. *Ab initio* calculations using the shell model (Heifets et al. 1998) showed that the surface energies of Sr-terminated and Ti-terminated (001) surfaces are nearly equal, implying that the two types of surfaces can coexist experimentally. Furthermore, it has been suggested (Padilla and Vanderbilt 1998) that the surface termination essentially depends on the growth conditions, and there is a slight preference for the TiO_2 termination.

STM and AFM observations collected by several groups have provided some insight into the morphological characteristics of reconstructed $SrTiO_3$ surfaces, while LEED and various spectroscopy techniques have provided supporting crystallographic and chemical information. This being said, there has not yet been a comprehensive study to provide researchers with a 'recipe' for consistent and reproducible preparation of various $SrTiO_3$ surfaces.

This chapter will concentrate on TEM studies of the (2x1), c(4x2) and c(6x2) $SrTiO_3$ (001) surface structures obtained under oxidizing conditions. By combining electron diffraction with bright/dark field imaging and high-resolution microscopy, TEM can be used to almost simultaneously characterize both the crystallography and morphology of a particular surface. This chapter is arranged in the following order: first,

the three different reconstructions observed under oxidizing conditions will be discussed. Following the structural information particular to each reconstruction, general morphological features common to all the observed $SrTiO_3$ reconstructed surfaces, as well as the effects of radiation damage on the surface structures in electron microscope, will be addressed. Finally, our comprehensive effort to obtain consistent and highly reproducible results for the various $SrTiO_3$ (001) surface terminations and determine the exact conditions for formation of these structures will be summarized with a phase diagram and phase formation rule.

Solution of the (2x1) Structure

The $SrTiO_3$ (001) single crystal TEM samples were annealed in a tube furnace at 950-1000°C with a constant flow of high-purity oxygen to eliminate damage caused by ion milling and to obtain the (2x1) reconstruction. These results were highly reproducible, indicating that the observed (2x1) structure is thermodynamically stable. Off zone-axis electron diffraction patterns, necessary for surface diffraction data analysis, and bright-field images were obtained using the UHV-H9000 Hitachi electron microscope operated at 300kV at Northwestern University. For HREM, the samples were tilted to the zone axis and the images were recorded using a JEOL-4010 electron microscope operated at 400kV at Argonne National Laboratory (ANL).

Diffraction data for the (2x1) reconstruction was collected by recording a series of negatives with exposure times varying from 0.5 to 120s and analyzed using strategies that were developed in Prof. L. D. Marks' group over the last decade (Jayaram, Xu, and Marks 1993). For a description of experimental details, see Chapter 2. The obtained intensities were averaged using a *p2mm* Patterson plane group symmetry to yield 18 independent intensities. Since *p2mm* Patterson symmetry may correspond to *pm*, *pg*, *p2mm*, *p2mg* or *p2gg* plane group symmetries, all were tested in the calculations. Final structure refinement was performed based on a χ^2 calculation.

Fig. 10 shows a bright-field image of the $SrTiO_3$ (001) sample combined with an off-zone axis selected area diffraction pattern. Reflections from both 2x1 and 1x2 domains are present. The diffraction spots can be characterized as follows: (a) strong bulk diffraction spots; (b) weaker bulk spots (present due to the difference in structure factors of Sr and Ti); and (c) relatively weak surface reflections.

The bright-field image shows rapid thickness variation of the sample towards the edge, obvious from the dark/bright contrast change of thickness fringes. The formation of large flat <100> facets on the surface of the sample owing to annealing is also shown in this image. Formation of similar atomically flat terraces was observed in several previous AFM and STM studies (e.g. Jiang and Zegenhagen 1996, 1999; Szot and Speier 1999).

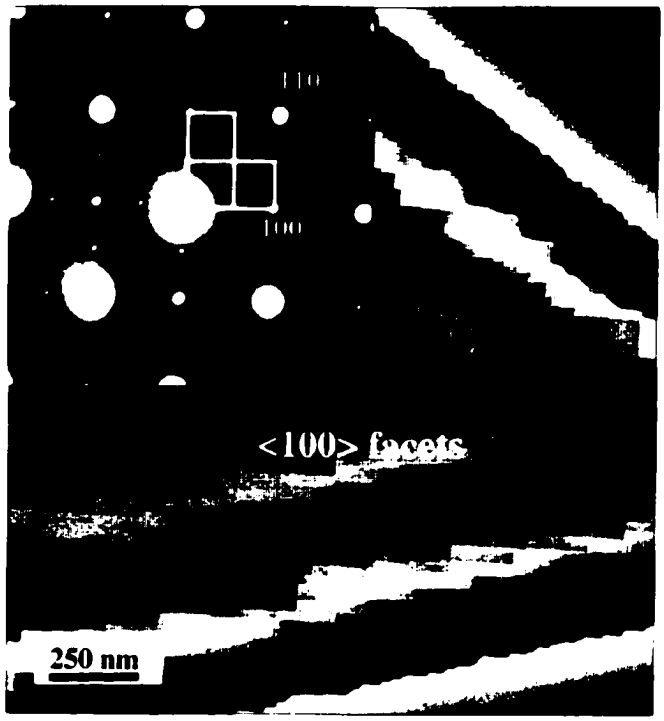

Fig. 10: Bright-field image and corresponding off-zone axis diffraction pattern of the 2x1 $SrTiO_3$ (001) surface. The surface unit cell for both domains of reconstruction is marked.

High-resolution images and Direct Methods calculations yielded the same general solution to the surface structure; for clarity the images will be described first. Fig. 11 shows a high-resolution image of a mainly single domain (2x1) surface and a corresponding power spectrum. The image was noise-filtered using a Wiener filter (Marks 1996) and the bulk contribution was suppressed, employing strategies similar to those used previously (Marks and Plass 1995; Bengu et al. 1996). We have also considered a possible contribution to the image contrast from the reconstruction

occurring on both the top and bottom surfaces. In this case (neglecting any focal difference between the top and bottom surfaces) the image can be written as:

$$I(\mathbf{r}) = S(\mathbf{r}) + S(\mathbf{r} + \mathbf{t}) \tag{9}$$

where $I(\mathbf{r})$ is the resulting image, $S(\mathbf{r})$ and $S(\mathbf{r} + \mathbf{t})$ are the image from top and bottom (translated by some vector $\mathbf{t}$) surfaces respectively. In reciprocal space, equation (9) can be written as:

$$I(\mathbf{k}) = S(\mathbf{k}) \cdot T(\mathbf{k}) + \eta \tag{10}$$

where $T(\mathbf{k}) = 1 + \exp(2 \cdot \pi \cdot i \cdot \mathbf{t} \cdot \mathbf{k})$ and η is the noise in the image. To obtain a single surface image, a Wiener filter is effectively applied in the Fourier space, while trying to avoid $T(\mathbf{k})=0$:

$$S(\mathbf{k}) = I(\mathbf{k}) \cdot T^{*}(\mathbf{k})/(\eta^{2} + |T(\mathbf{k})|^{2}) \tag{11}$$

where $T^{*}(\mathbf{k})$ is the complex conjugate of $T(\mathbf{k})$. Fig. 12 shows the results of calculations with respect to different translation vectors ($\mathbf{t}$) and noise (η). For more details on this type of calculations see Bengu et al. 1996.

Fig. 13 displays the HREM image after lattice averaging (left) and after filtering to separate translation/inversion domains of the structure (right) on the top and bottom surfaces with an image simulation inset in the center. The images show a dominant structural motif, a zig-zag row of features with local *p2mg* symmetry.

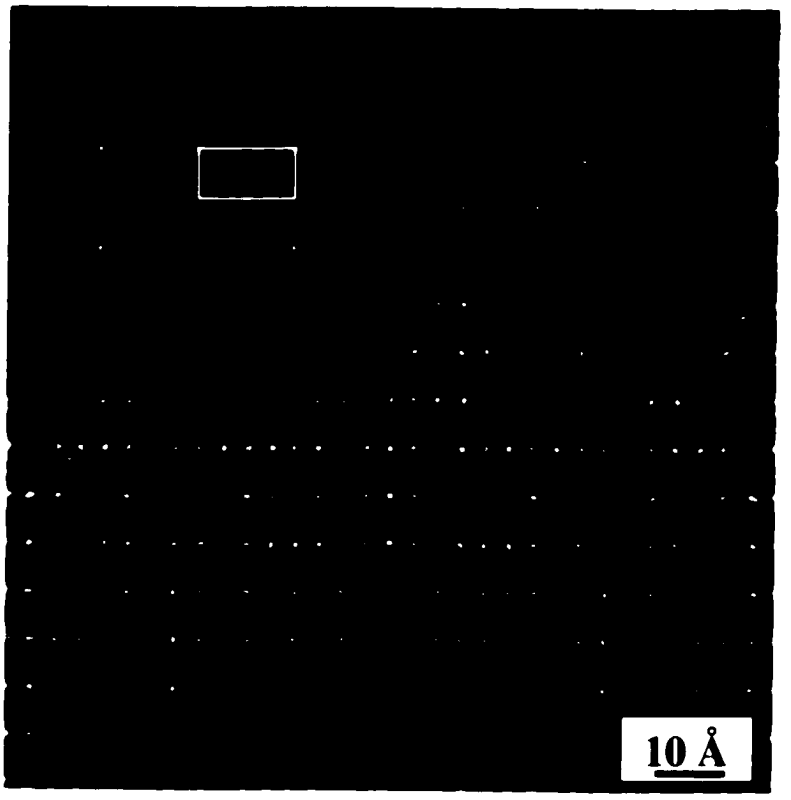

Fig. 11: High-resolution image of the (2x1) $SrTiO_3$ (001) surface, taken using the JEOL-4010 TEM at ANL. The image has been Wiener-filtered (see text) and the bulk spots have been digitally removed. The inset shows the corresponding power spectrum.

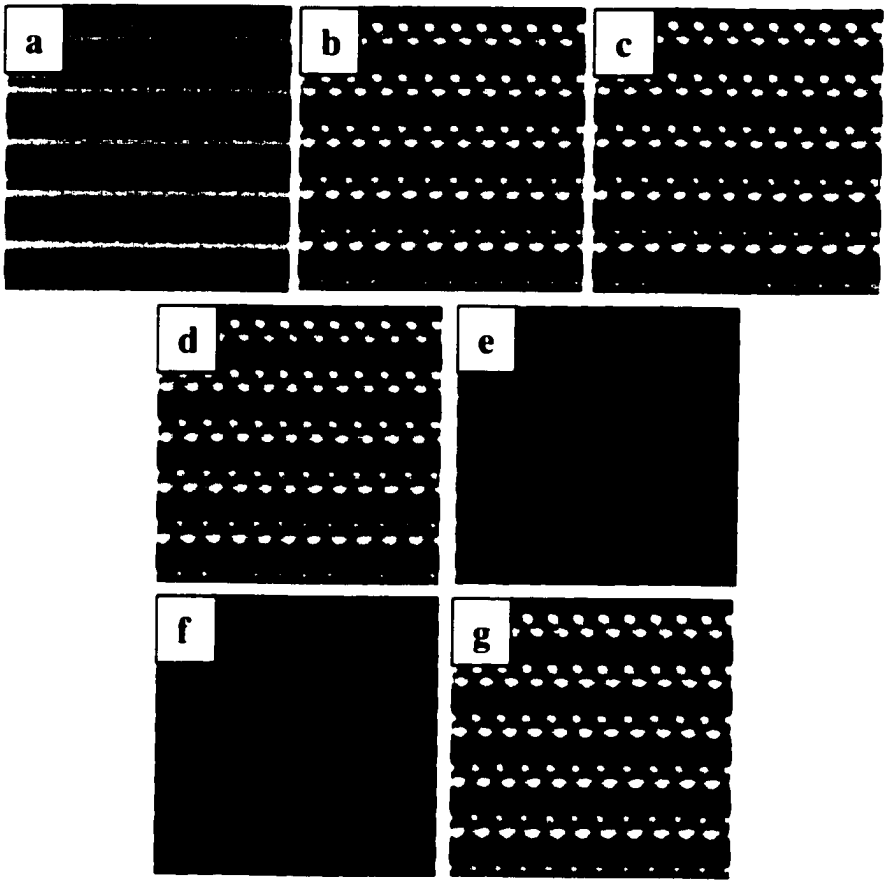

Fig. 12: Results of the calculation of the single surface image with respect to different translation vectors (**t**) and noise (η). (a) η=0.01-0.7, **t**=0.5*[010]; (b) η=0.05, **t**=2*[110]; (c) η=0.05, **t**=1*[110]; (d) η=0.05, **t**=1*[010]; (e) η=0.05, **t**=1*[100]; (f) η=0.05, **t**=0.5*[100]; (h) η=0.05, **t**=2*[1-10].

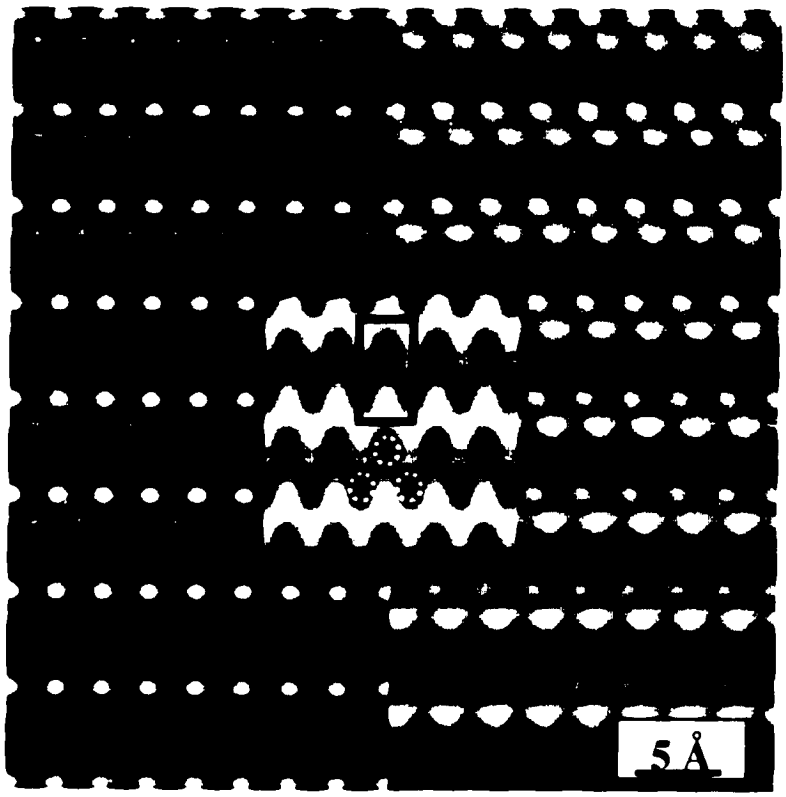

Fig. 13: Enlarged translation-averaged HREM image of the (2x1) structure before (left), and after (right) separation of domains on the top and bottom surface. The inset shows a multislice simulation of the structure (defocus -55 nm) with the unit cell marked. The strong black features correlate with the positions of the surface Ti atoms.

Numerical image simulations calculated using a multislice algorithm (see inset in Fig. 13) were in fairly good agreement with the experimental data, with black dots corresponding to surface Ti sites. Among the plausible solutions determined via direct methods, only those containing the same structural element (e.g. Fig. 14) were stable to

subsequent refinements. Analysis indicated that these were Ti atom sites (not O or Sr), and using conventional Difference Maps combined with χ^2 refinements we were able to determine the oxygen sites.

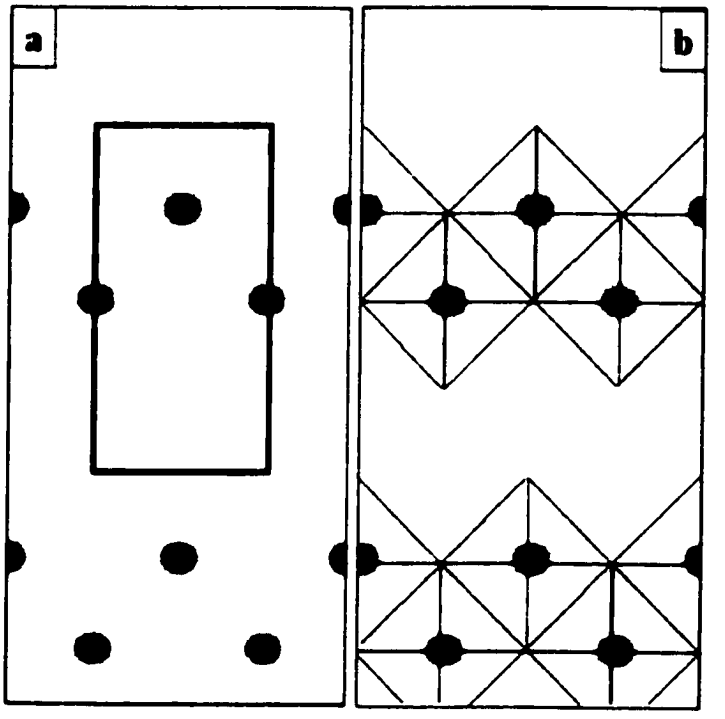

Fig. 14: Direct Methods solution of the (2x1) structure: (a) scattering potential map calculated from 2D code for *pm* symmetry; (b) interpretation of the map in terms of TiO_x units. The primitive unit cell is indicated with solid lines (a= 3.905, b=7.81 Å, α=90°). In both cases regions of high potential, i.e. possible atomic sites are black, and subsequent analysis demonstrated that Ti atoms occupied these sites.

The refinement of the structure against the diffraction data allowed both the Ti and O atom positions to be determined with a χ^2=2.01. Alternative structural models, for example O addition on top of the Ti atoms, were considered, however the refinement results for these models were significantly inferior to the proposed solution.

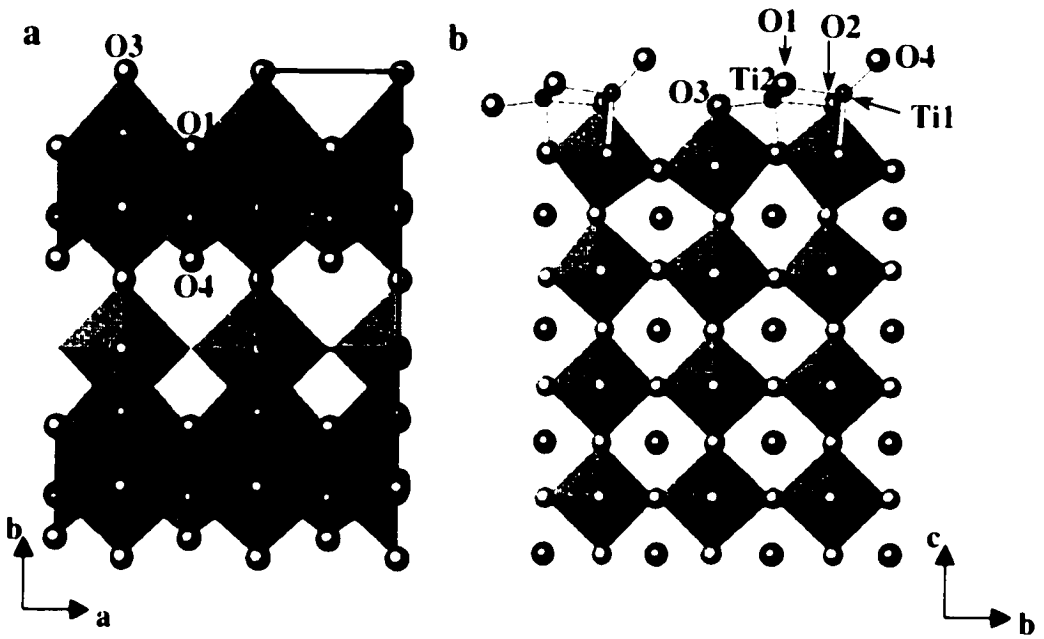

Fig. 15: The (2x1) $SrTiO_3$ (001) surface structure: (a) top view and (b) side view. TiO_x units are shown as partially filled octahedra on the surface; the primitive unit cell is indicated with solid lines (a=3.905, b=7.81 Å).

Table 7: Atom positions obtained from χ^2 refinement and plane-wave DFT calculation for the $SrTiO_3$ (001) (2x1) surface structure (a= 3.905 Å, b= 7.810Å). The X coordinate is given by symmetry. For the Y coordinate we list experimental and theoretical positions (in brackets). The Z position is a result of DFT calculation. The position of the atom marked with * serves a reference point for the Z position of the other atoms.

Layer	Atom	X	Y	$\lvert Y_{exp} - Y_{DFT} \rvert$ (Å)	Z (Å)	$\lvert Z_{bulk} - Z_{DFT} \rvert$ (Å)	Charge (e)
1 (surface)	Ti 1	1/2	0.4989 (0.5011)	0.017	6.213	0.355	+1.90
	Ti 2	0	0.2159 (0.2295)	0.106	6.006	0.148	+1.98
	O 1	1/2	0.2476 (0.2792)	0.247	6.507	0.649	-1.10
	O 2	0	0.5147 (0.4971)	0.137	5.844	0.014	-1.18
	O 3	0	0.0096 (0.0046)	0.039	5.784	0.074	-0.83
	O 4	1/2	0.6904 (0.6798)	0.083	7.344	1.486	-0.66
2	Ti 3	0	0.9900 (0.9860)	0.031	3.975	0.070	+1.98
	Ti 4	0	0.5134 (0.5146)	0.009	3.876	0.029	+2.02
	O 5	1/2	(0.9977)	N/A	3.723	0.182	-1.13
	O 6	1/2	(0.5229)	N/A	4.131	0.226	-1.17
	O 7	0	(0.2507)	N/A	4.2	0.295	-1.16
	O 8	0	(0.7499)	N/A	3.627	0.278	-1.14
3 (bulk)	Sr 1	1/2	(0.2408)	N/A	2.082	0.129	+1.74
	Sr 2	1/2	(0.7597)	N/A	2.007	0.054	+1.67
	O 9	0	(0.4691)	N/A	2.109	0.156	-1.21
	O 10	0	(0.0250)	N/A	1.983	0.030	-1.26
4 (bulk)	Ti 5	0	(0.0023)	N/A	0.156	0.156	+1.95
	Ti 6	0	(0.4979)	N/A	0.114	0.114	+2.02
	O 11	1/2	(0.9995)	N/A	0.096	0.096	-1.24
	O 12	1/2	(0.5000)	N/A	0.186	0.186	-1.20
	O 13	0	(0.2509)	N/A	0*	0*	-1.20
	O 14	0	(0.7485)	N/A	0.267	0.267	-1.23

Due to its 2D nature, the diffraction data cannot be used to refine the atomic positions along the z (i.e. out of plane) axis. Therefore, plane-wave pseudo-potential density functional (DFT) calculations (Kresse and Hafner 1993; Kresse and Furthmuller 1996; Vanderbilt 1990; Perdew 1991) on a 13-layer slab model were performed by Dr. M. Asta as an independent 3D structure refinement. The experimentally obtained atomic positions were used as a starting point for these calculations. In addition to confirming the in-plane (x,y) positions obtained from the χ^2 refinement, the DFT calculations relaxed the structure in z direction. Fig. 15 shows the solution of the (2x1) $SrTiO_3$ surface structure. Atomic positions for the (2x1) structure are listed in Table 7.

The top layer has a TiO_2 stoichiometry, with half of the TiO_5 units displaced along the [110] direction. These displacements result in a row of 5-coordinated TiO_5 units that share edges between them as well as with the underlying layer that forms part of the first full intact TiO_2 layer of $SrTiO_3$ with 6-coordinated Ti atoms. The TiO_6 octahedra in the underlying bulk layers are tilted in order to support the reconstructed surface. In the surface layer we can distinguish between two different types of O atoms: (a) 'internal' O atoms (O1, O2) tightly bound inside the surface rows and shared between the octahedra; (b) 'external' O atoms (O3, O4), not shared between the octahedra. The distances between the surface Ti atoms to the two external oxygens are significantly shorter than the bulk Ti-O distances (1.51 and 1.77 Å vs. 1.95 Å), whereas the distance between the internal oxygens to surface Ti is bulk-like. The detailed bond lengths for the (2x1) structure are presented in Table 8. Apparently the surface Ti atoms compensate for the

lower coordination number by stronger bonding to the external oxygens. Dr. O. Warschkow employed near-minimal basis linear combination of atomic orbitals (LCAO) DFT calculations (Warschkow, Dyke and Ellis 1998) to obtain partial atomic charges for this structure. In support of the above argument, the charge analysis finds that the surface Ti and internal oxygens are bulk-like (Ti +2.0, O –1.2), while the charges on the two external oxygens are significantly reduced (O3 –0.8 and O4 –0.6 compared to –1.2 in the bulk), indicating increased covalence.

Table 8: Bond distances for atoms in the overlayer of the $SrTiO_3$ (2x1) structure.

Bond	Distance (Å)
Ti1-O1	2.02
Ti1-O4	1.51
Ti1-O2	2.01
Ti2-O1	2.05
Ti2-O2	2.10
Ti2-O3	1.77

$SrTiO_3$ is representative of a large class of oxides with the perovskite structure; therefore it is important to understand the basic character of its surfaces because similar considerations will likely be applicable to other materials. It is well established that the coordination chemistry of oxides exhibiting perovskite structures is dominated by the formation of corner-shared octahedral building blocks, along with large cations to achieve the appropriate stoichiometry. In the ABO_3 structure, the presence of the A cation prevents any structural rearrangement in the surface region. When these large cations are absent, however, the ReO_3 - type structure is created. This latter structure can have corner as well as edge-shared octahedra, and consequently possesses additional degrees of freedom that can be exploited for structural rearrangements. On chemical grounds, we therefore expect that the surface of a perovskite will rearrange to a BO_{3-x} configuration, effectively screening the B cations, while also minimizing surface dipoles and maximizing the coordination.

The (2x1) surface structure reflects these concepts and is a hybrid of three components:

1) A linear structure involving two titanium atoms (Ti1 and Ti2) and two oxygens (O1 and O2) with essentially bulk-like electronic structure similar to edge-shared octahedral units, where each O atom is coordinated to 3 or 4 Ti atoms.

2) Two external oxygen atoms (O3 and O4) with much more covalent character, particularly O4 which is double-bonded to Ti1; the coordination number for each of the external O atoms is 1 or 2.

3) A slightly distorted bulk-like TiO_2 sub-surface layer that terminates the underlying $SrTiO_3$ lattice.

Solution of the (4x2) Surface Structure

Samples annealed at lower temperatures (850-930°C) exhibit the c(4x2) surface structure. An example of a typical c(4x2) off-zone axis diffraction pattern as well as a high-resolution bright-field image is presented in Fig. 16. The bright-field image shows several different morphological features – large surface steps (50-200 nm wide) as well as rectangular features ~2-10 nm in size. Whereas the majority of the step edges are oriented along [100] or [010] directions, in some areas it can be clearly seen that <110> type facets are stabilized as a result of annealing. The general morphology of the $SrTiO_3$ surfaces will be discussed in further detail later on in this chapter.

Diffraction data for the c(4x2) reconstruction were collected, analyzed and refined using strategies similar to those employed for the (2x1) surface (see above). The intensities were averaged using a *c2mm* Patterson plane group symmetry to yield 34 independent intensities. Structure refinement was performed based on χ^2.

Figure 17a shows the c(4x2) structure solution obtained using Direct Methods in terms of a scattering potential map. The map shows the dominant structural motif, a block of 4 features. Analysis indicated that these features were Ti atom sites (not O or Sr), and using conventional Difference Maps combined with χ^2 refinements we were able to

determine the oxygen atomic positions in the top layer. The refinement of the structure against the diffraction data gave both the Ti and O atom positions. Figure 17b shows the scattering potential map interpreted in terms of TiO_x pseudo-octahedral units. A number of alternative models of the structure, such as different relative position of the sub-surface layer with respect to the top layer, and the addition of O on top of the Ti atoms, were considered. The refinement results were significantly inferior to the proposed solution.

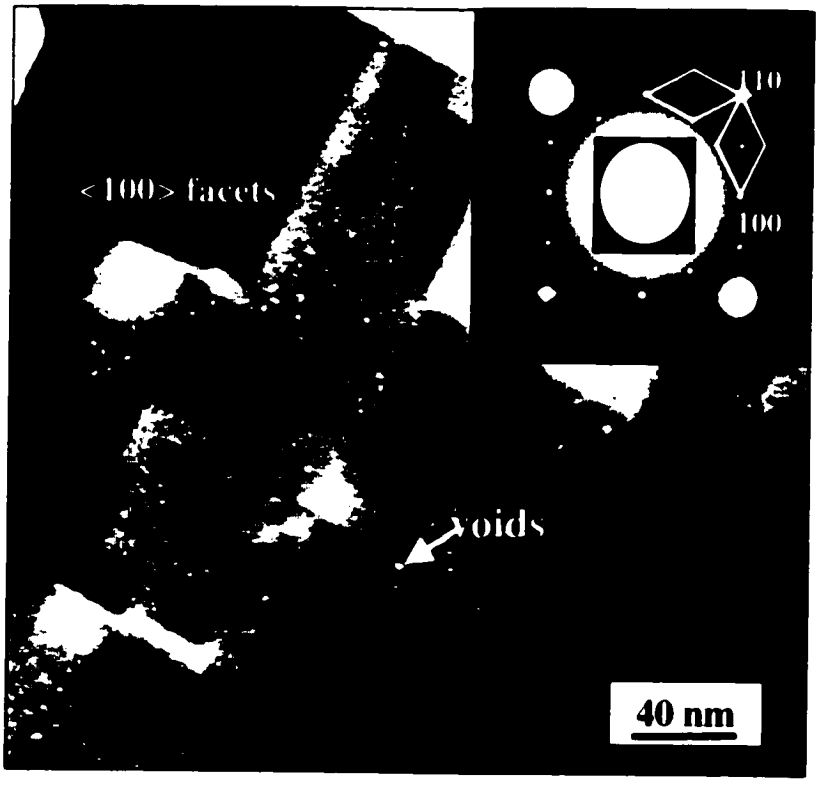

Fig. 16: Bright-field image and off-zone axis diffraction pattern of the c(4x2) $SrTiO_3$ (001) surface. The primitive surface unit cell for both domains of the reconstruction is marked.

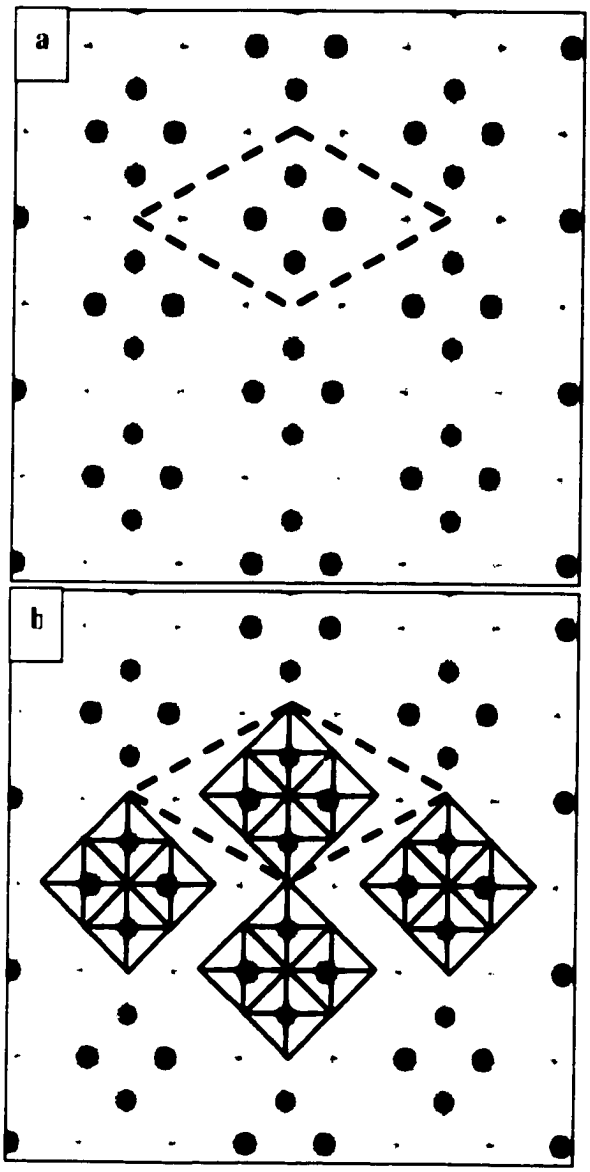

Fig. 17: (a) Solution of the c(4x2) $SrTiO_3$ structure obtained using Direct Methods in terms of a scattering potential map; (b) interpretation of the map in terms of TiO_x pseudo-octahedral units.

The x,y-positions of atoms in the top layer of the structure were deduced quite unambiguously from the scattering potential maps. These positions indicate that the surface structure consists of a combination of edge sharing TiO_x units with 4 Ti atoms in each unit. The manner in which this surface layer could attach to the underlying bulk layers however, presented some ambiguity. Bearing in mind the coordination requirements for perovskite and ReO_3 –type structures as well as the surface structure formation rules outlined for the (2x1) structure previously (Erdman et al. 2002), we have considered two possible structures as starting geometries for DFT geometry optimization.

The two possible configurations are shown schematically in Figure 18; hereafter, for simplicity, we will refer to the structures as 'A' and 'B'. Additional electron diffraction data refinements were performed using these two possible configurations of the subsurface layer with respect to the surface TiO_x overlayer. The results of the refinement suggested that structure 'B' (χ^2=1.9) is favored over structure 'A' (χ^2=2.4).

The DFT geometry optimization (performed by Dr. O. Warschkow using strategies described above for the (2x1) reconstruction) yielded two different surface structures (stationary points on the potential energy surface), shown in Figures 19 and 20 (both top and side views). The atomic positions for both structures are listed in Table 9 (structure A) and Table 10 (structure B). Although the calculated x,y atomic positions for both surfaces are consistent with the experimental data, a distinction between the two possible structures can be made based on the calculated surface energies. The B surface

structure was found to be more stable that the A surface by 2.0 eV per c(4x2) surface unit. We therefore consider the B surface to be the observed c(4x2) surface structure.

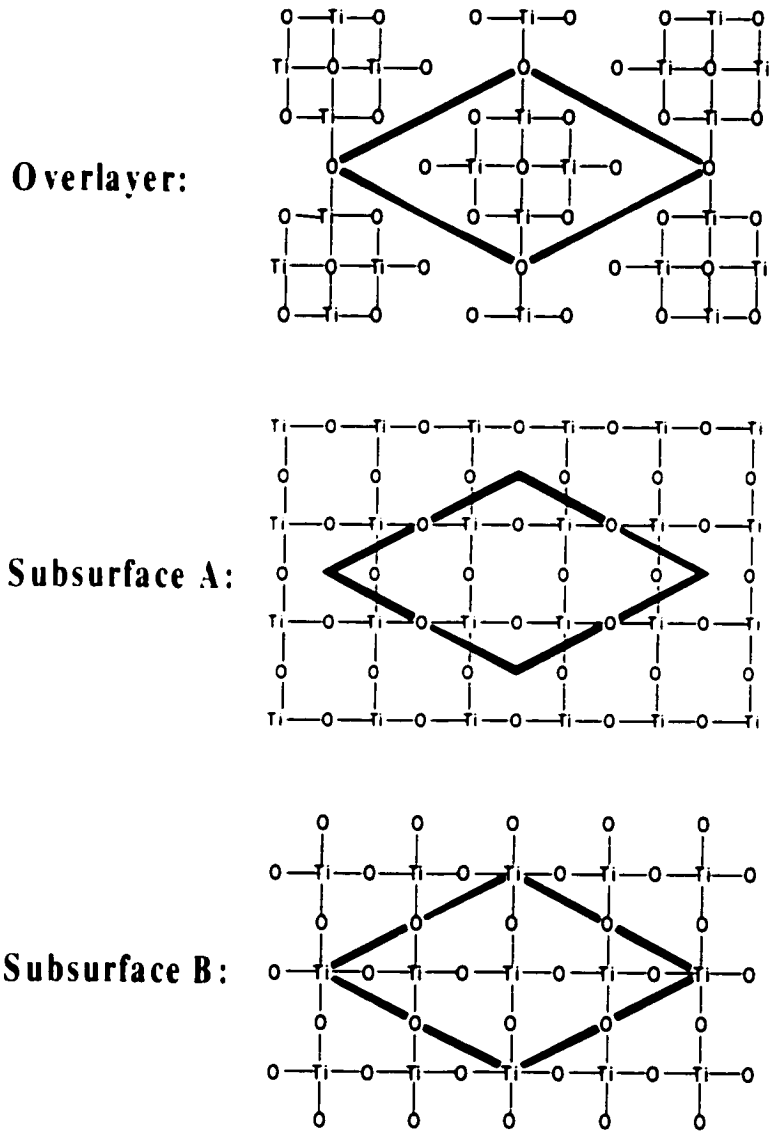

Fig. 18: The overlayer on top of two possible configurations (A and B) of the sub-surface layer in the (4x2) structure.

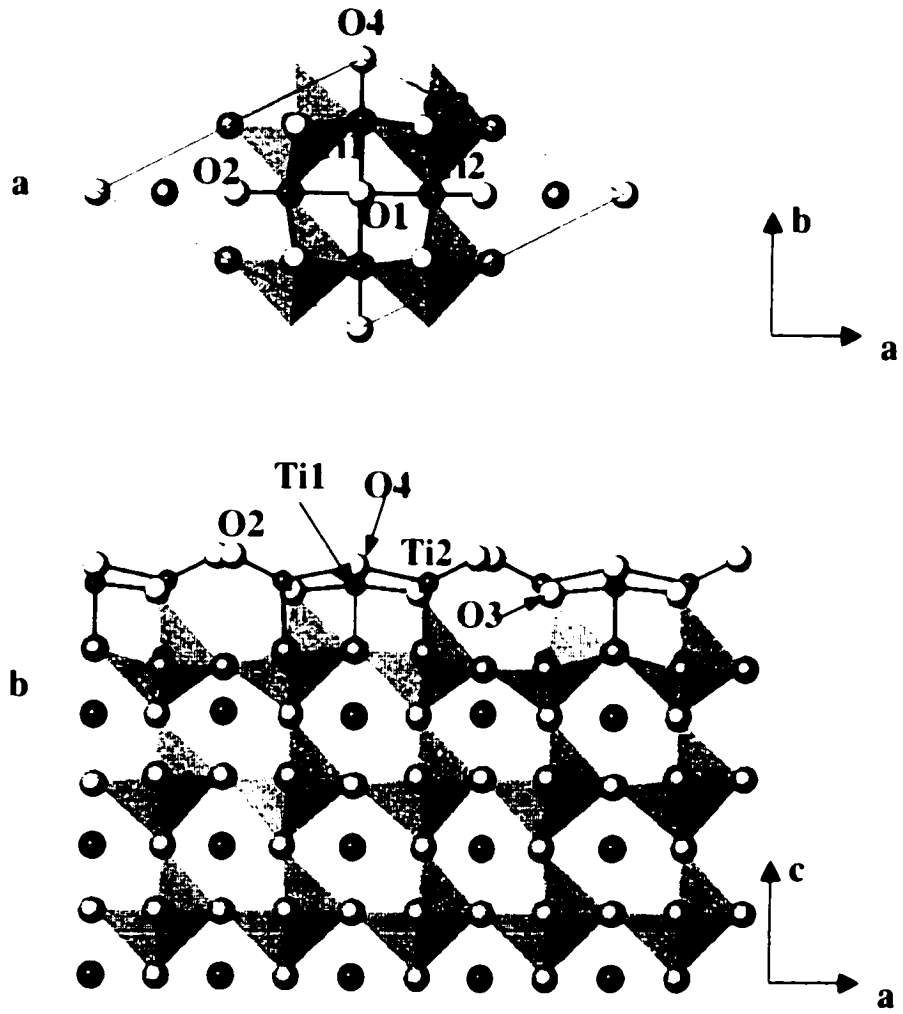

Fig. 19: Structure 'A' obtained through DFT geometry optimization. (a) Top view; (b) Side view. Primitive unit cell is outlined (a=15.62 Å, b=7.81 Å).

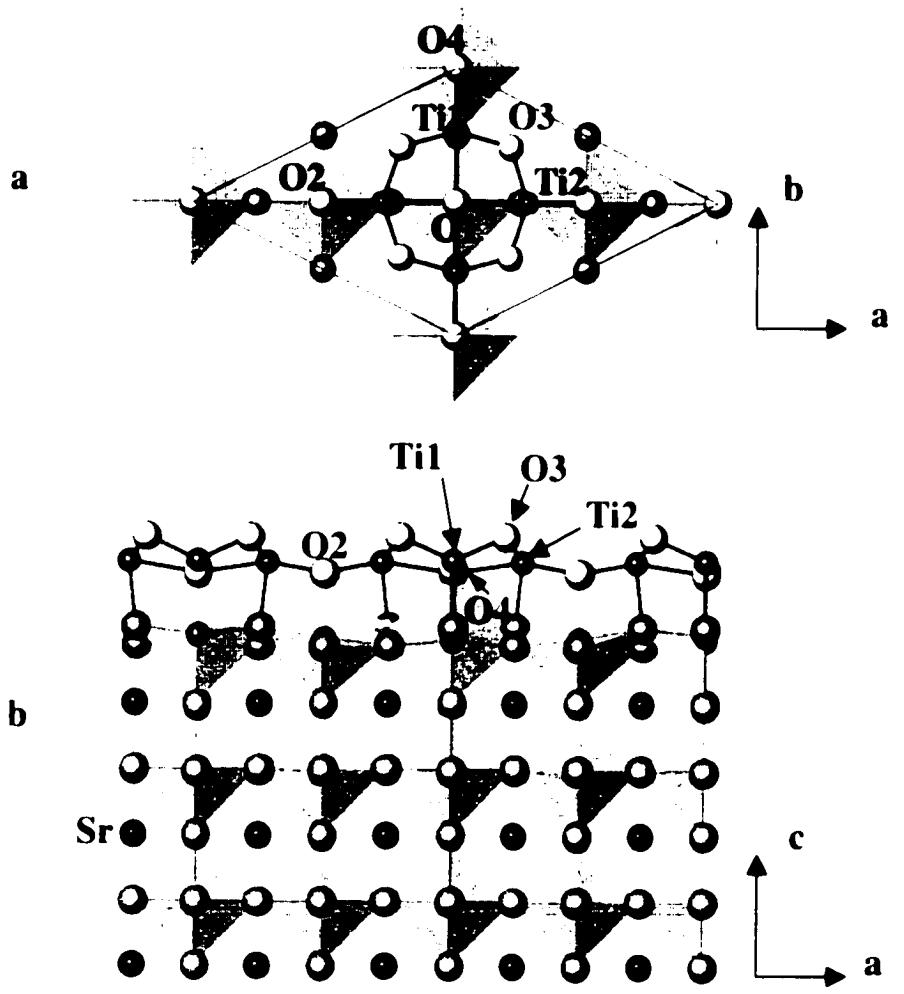

Fig. 20: Solution of the c(4x2) surface structure (Structure 'B'). Primitive unit cell is outlined (a=15.62 Å, b=7.81 Å).

Table 9: Atom positions obtained from χ^2 refinement and plane-wave DFT calculation for the (4x2) surface structure 'A' (a=15.62 Å, b= 7.810Å). The X,Y and Z positions are a result of DFT calculation. Sr atom in the 7th layer serves a reference for Z position.

Layer	Atom	X	Y	Z (Å)	$\lvert Z_{bulk} - Z_{DFT} \rvert$ (Å)
1 (Surface)	Ti	0.3607	0	12.025	0.310
	Ti	1/2	0.2757	11.917	0.202
	O	0	0	12.458	0.743
	O	1/2	0	12.480	0.765
	O	0.2653	0	12.768	1.053
	O	0.3800	0.2465	11.728	0.013
2	Ti	0.3678	0.2608	9.788	0.026
	O	1/4	1/4	9.507	0.256
	O	0.1294	0	9.515	0.248
	O	1/2	0.2686	10.018	0.256
	O	0.3676	0	9.975	0.213
3	Sr	0	0	7.821	0.011
	Sr	1/2	0	7.933	0.123
	Sr	0.2562	0	7.819	0.009
	O	0.3872	0.2289	7.859	0.049

Table 10: Atom positions obtained from χ^2 refinement and plane-wave DFT calculation for the (4x2) surface structure 'B' (a=15.62 Å, b= 7.810Å). For the X and Y coordinates we list experimental and theoretical positions (in brackets). The Z position is a result of DFT calculation. Sr atom in the 7th layer serves a reference for Z position.

Layer	Atom	X	Y	Z (Å)	$\lvert Z_{bulk} - Z_{DFT} \rvert$ (Å)
1 (Surface)	Ti	(0.3622) 0.3761	0	12.168	0.453
	Ti	1/2	(0.2625) 0.2461	12.208	0.493
	O	0	0	11.940	0.225
	O	1/2	0	11.848	0.133
	O	(0.2488) 0.2455	0	11.828	0.113
	O	(0.3962) 0.3771	(0.2064) 0.2077	12.932	1.217
2	Ti	0	0	9.794	0.032
	Ti	1/2	0	9.859	0.097
	Ti	(0.2405)	0	9.969	0.207
	O	1/4	1/4	9.640	0.123
	O	(0.1227)	0	9.633	0.130
	O	1/2	(0.2529)	10.203	0.441
	O	(0.3756)	0	10.179	0.417
3 (bulk)	Sr	(0.3682)	(0.2514)	7.895	0.085
	O	0	0	7.918	0.108
	O	1/2	0	8.019	0.209
	O	(0.2585)	0	7.835	0.025

In both structures A and B (Figures 19 and 20, respectively) we observe some of the features that were characteristic of the (2x1) structure: edge-sharing among the pseudo-octahedral TiO_x units in the top layer and between these units and the full intact TiO_2 bulk-like layer underneath; relaxation and tilting of the octahedra in the bulk and more so in the surface layer to accommodate the reconstruction. Both structures have TiO_2 stoichiometry.

The main difference between the A and B structures is the O coordination. In structure A some of the oxygen atoms in the overlayer are undercoordinated and as a result the structure is significantly distorted. In structure B, however, the coordination is similar to that of the bulk and the relaxation in the z direction readily occurs. The distances between the surface Ti atoms and the surface oxygen atoms are listed in Tables 11 and 12. The bond lengths in structure A, like those in the (2x1) structure, are significantly shorter than bulk bond lengths - the distance between Ti2 and O2 is 1.67 Å vs Ti-O distance of 1.95 Å in the bulk. Structure B, however, shows more bulk-like bond distances – 1.8 Å between Ti2 and O2 and 2.18 Å between Ti2 and O1.

The shift of the underlying bulk between A and B structures, causes oxygen atoms that are 'coordinating' in the A structure to become 'floating' in the B structure. Floating oxygen atoms (i.e. those that are not bound to Ti atoms in the layer underneath) possess a great deal of flexibility in the vertical position. The positions of coordinating oxygen atoms as well as surface Ti atoms, on the other hand, are relatively fixed because they are bound to atoms below. Thus, the A and B surface, differ in how the positional flexibility

provided by the floating oxygen atoms is allocated over the surface. It is convenient, as we have done for the (2x1) reconstruction (Erdman et al. 2002), to identify two different types of surface oxygen. Here, we note the distinction between 'internal' (O1 and O3 in Fig. 19 and 20), that are tightly bound to the block of four edge-shared TiO_5 truncated octahedra, and 'external' (O2 and O4 in Fig. 19 and 20), bound to the periphery of these blocks.

Table 11: Bond distances for atoms in the overlayer of structure A.

Bond	Distance (Å)
Ti1 – O3	1.90
Ti1 – O4	1.83
Ti1 – O1	2.23
Ti2 – O3	1.97
Ti2 – O1	2.22
Ti2 – O2	1.67

Table 12: Bond distances for atoms in the overlayer of structure B.

Bond	Distance (Å)
Ti1 – O3	1.83
Ti1 – O4	1.87
Ti1 – O1	2.08
Ti2 – O3	1.86
Ti2 – O1	2.18
Ti2 – O2	1.80

In the A structure, all external oxygen atoms are floating; among the internal atoms, only the single O1 at the center of the block is floating. In the B structure, only the four internal oxygen atoms at the corner of the block are floating (though they are coordinated to two Ti atoms each), and the external O2, O4 and center O1 atoms are coordinating. In short, in the A structure, most of the vertical positional flexibility of the floating atoms is concentrated on the external atoms, whereas in the B-structure the flexibility is on the internal atoms. In the (2x1) structure, by contrast, 'floating' and 'coordinating' oxygen sites were found to be equally distributed over internal and external sites. In all reconstructions, the positional flexibility of the floating oxygen

atoms certainly plays a critical role in stabilizing the under-coordinated Ti atoms at the surface.

In the (2x1) reconstruction we noted a regular tilting in the (100) direction of subsurface TiO_6 octahedra (Fig. 15), achieved by alternating upwards and downwards displacements of oxygen atoms in the sub-surface layers. The tilting of MO_6 octahedra is a well-known phenomenon in bulk perovskites and results in a variety of different phases. We note in the subsurface of the calculated A reconstruction (Figure 19), an alternating octahedral tilting mode very similar to that found in the (2x1) structure. In contrast, the more stable B reconstruction (Fig. 20) exhibits an irregular distortion of sub-surface TiO_6 octahedra; the only notable similarity between the A and B reconstructions is that sub-surface oxygen atoms bound to Ti in the overlayer are displaced upwards from subsurface layer. Therefore, the overlayer structure determines the degree of tilting or distortion of the TiO_6 octahedra in the sub-surface layers.

Investigation of the (6x2) Surface Structure

Higher annealing temperatures (1050 to 1100°C) can be used to produce a c(6x2) surface structure. Fig. 21 shows a dark-field image obtained from the c(6x2) surface using a (110) reflection and the inset shows an off-zone axis diffraction pattern from the same surface. The image clearly shows surface domains rotated 90° with respect to each

other. The general morphology of the surface is similar to the other $SrTiO_3$ (001) reconstructed surfaces discussed above.

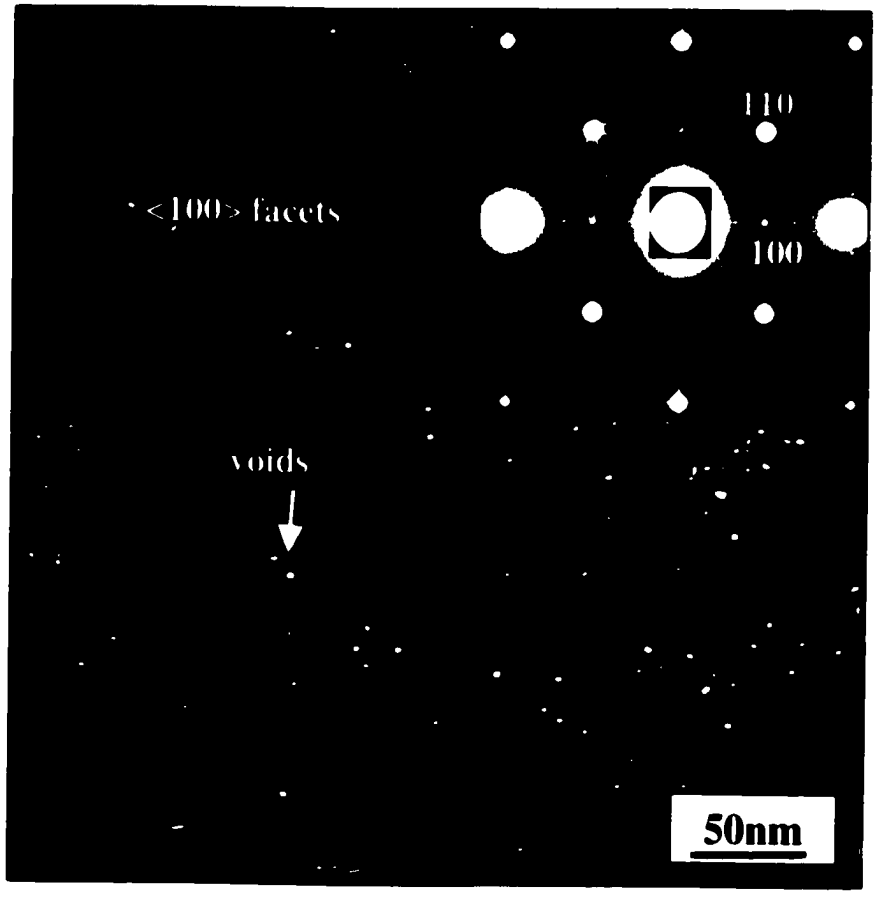

Fig. 21: Dark-field image and off-zone axis diffraction pattern of the c(6x2) $SrTiO_3$ (001) surface. The primitive surface unit cell for both domains of the reconstruction is marked.

We have performed Direct Methods analysis of the electron diffraction data obtained for this reconstruction using the strategies described for the (2x1) and the (4x2) structures above. The intensities were averaged using a *c2mm* Patterson plane group

symmetry to yield 58 independent intensities. The solution of the 6x2 structure in terms of the scattering potential map is presented in Fig. 22. Currently, refinement calculations are under way to determine the structure of the (6x2) $SrTiO_3$ surface.

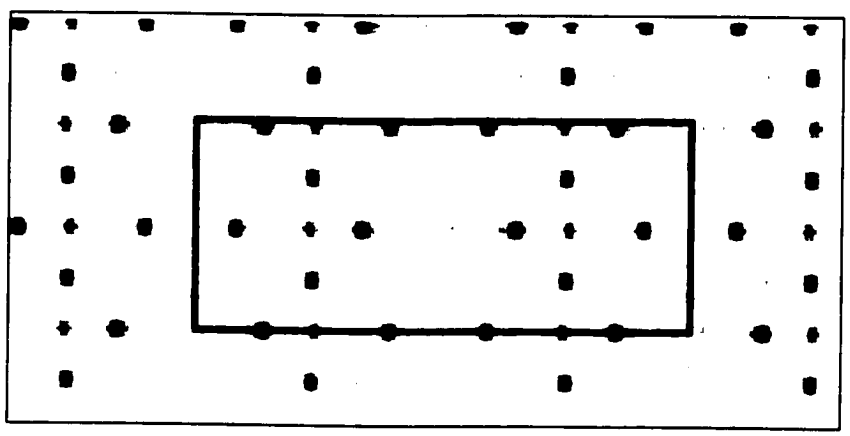

Fig. 22: The solution of the c(6x2) structure using Direct Methods in terms of the scattering potential map. The centered unit cell is outlined.

Surface Morphology

Unannealed Surface

After ion-milling and prior to annealing, the surface of $SrTiO_3$ (001) exhibits some disorder and strain. Fig. 23 shows a bright-field image and corresponding diffraction pattern of a typical sample. The diffraction pattern has two distinct features: bulk diffraction spots as well as an amorphous ring that can be attributed to a disordered

surface layer resulting from ion-milling. The bright-field image shows strain effects such as bend contours. These findings suggest that the unannealed, ion-milled surface is unreconstructed and does not exhibit an ordered 1x1 structure.

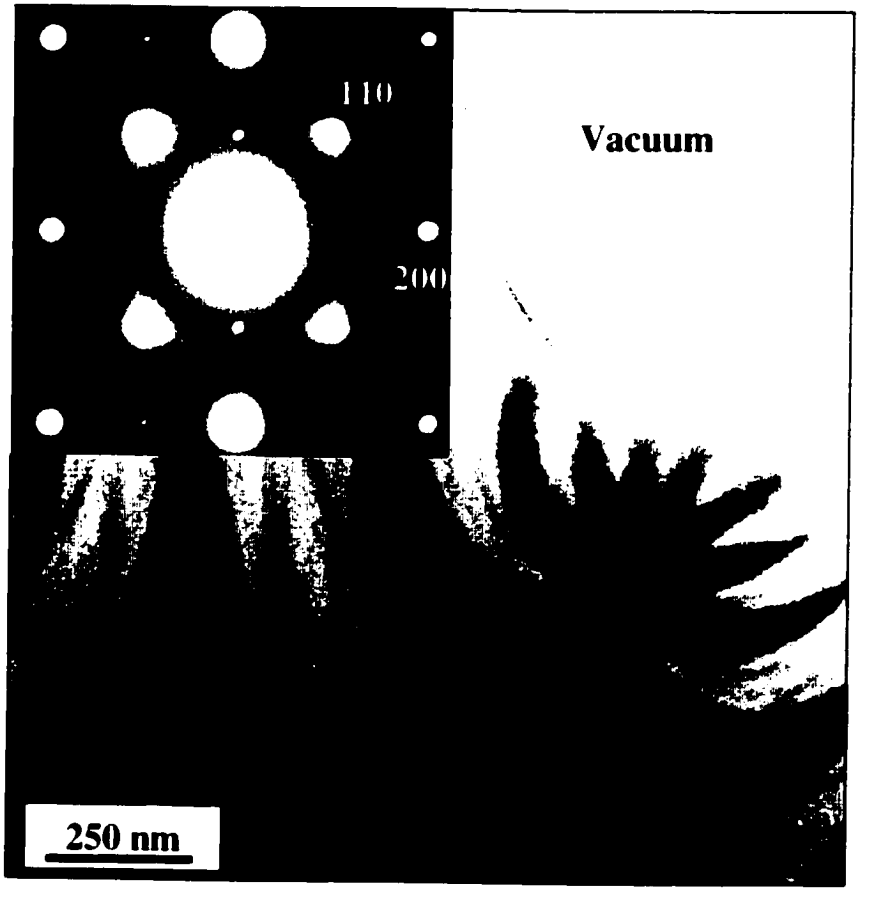

Fig. 23: Bright-field image of the $SrTiO_3$ (001) sample prior to annealing and a corresponding selected area diffraction pattern.

Voids

The small rectangular features that can be clearly seen in Fig. 16 and 21 are attributed to voids. The features show no strain contrast, suggesting that they are neither precipitates nor trapped gas bubbles. They are clearly located in the near-surface region of the sample; if the voids were extremely deep then their density would increase as the sample thickness becomes greater, but no such evidence is observed here. It is important to understand that the voids are unrelated to the reconstruction itself: the steps and surface domains can be seen crossing the voids unperturbed. The number of voids observed per sample area is governed mainly by the sample preparation procedure (i.e. the amount of ion milling prior to annealing, as well as the annealing temperature and time). Similar features, though of larger in dimensions (~20-50 nm in length and width, 12 Å deep) were observed by Jiang and Zegenhagen (1999) and were attributed to holes in the sample due to a thermal etching effect.

Multislice simulations were performed in order to assure that the contrast of these rectangular features seen in HREM images corresponds to voids and is not due to a precipitate of a different phase or a hole on the sample surface. For the purposes of the simulation, a 10x10 unit cell (39.05x39.05 $Å^2$) slab of $SrTiO_3$ with a total thickness of 200 to 250 Å was used. The shape of the void was assumed to be a rectangular parallelepiped positioned in the middle of the slab. The dimensions of the void were 5x5 unit cells in projection (19.525x19.525 $Å^2$). The parameters varied during the calculation were relative position of the void with respect to the surface layer (1 to 5 bulk unit cells)

and the thickness of the void (2 to 5 bulk unit cells). The results of the simulations were compared to the HREM images of the voids obtained using a JEOL 4010 electron microscope at Argonne National Lab operated at 400kV. The experimental HREM image and the multislice simulation of a void, both shown in Fig. 24, are in fairly good agreement with each other. The simulation results suggest that the void is positioned approximately 10 Å below the surface layer.

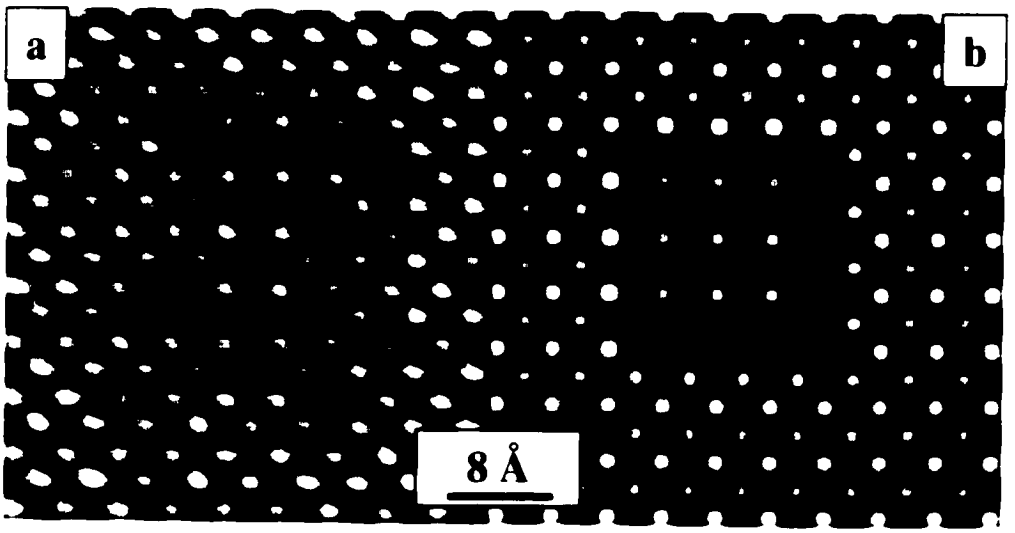

Fig. 24: (a) Experimental HREM image, and (b) multislice simulation (~40nm) of the void. The depth of the voids is about 10 Å with the void positioned approximately 10 Å below the surface layer.

General Morphology of the Reconstructed Surfaces

The $SrTiO_3$ surface structures produced under oxidizing conditions described above are highly reproducible and can be obtained on the same crystal simply by changing the annealing temperature. Independent of the reconstruction achieved on the surface, the morphology of a sample is transformed after annealing as compared to the unreconstructed surface. The temperatures used in these annealing experiments are approximately 1/3 to 1/2 of the melting temperature of $SrTiO_3$, assuring a significant amount of surface diffusion capable of producing well-ordered, faceted surfaces. Faceting, therefore, can be considered a strong indication that the surface has reconstructed. Longer annealing times produce larger facets and reduce the number and size of the surface defects.

The fact that the majority of the step edges are oriented along the [100] and/or [010] directions, the sharpness of the facet edges, and the rectangular shape of the voids all suggest that the {100} facets are the most stable surfaces. On the other hand, an interesting feature common to all of the reconstructions is the formation of the <110> facets in some areas of the samples. The unreconstructed $SrTiO_3$ (110) surface is polar – in this case the repeat unit contains alternating layers of SrTiO (net charge of +4) and O_2 (net charge –4). The layers are unquestionably charged, therefore creating a net dipole moment. Brunen and Zegenhagen (1997) investigated the (110) surface of $SrTiO_3$ under a variety of annealing conditions using LEED, AFM and STM. Their results showed the formation of a large number of reconstructions of the type (n x m); moreover, LEED and

STM data suggested that some of these structures are incommensurate with the underlying bulk lattice. Our preliminary results from TEM analysis of $SrTiO_3$ (110) samples also suggest that the (110) surface does reconstruct upon annealing the sample at 900°C (Fig. 25). Some of the morphological features we observed on the reconstructed (110) surface are similar to those found on the (100) surface – formation of large facets as well as rectangular shaped surface defects.

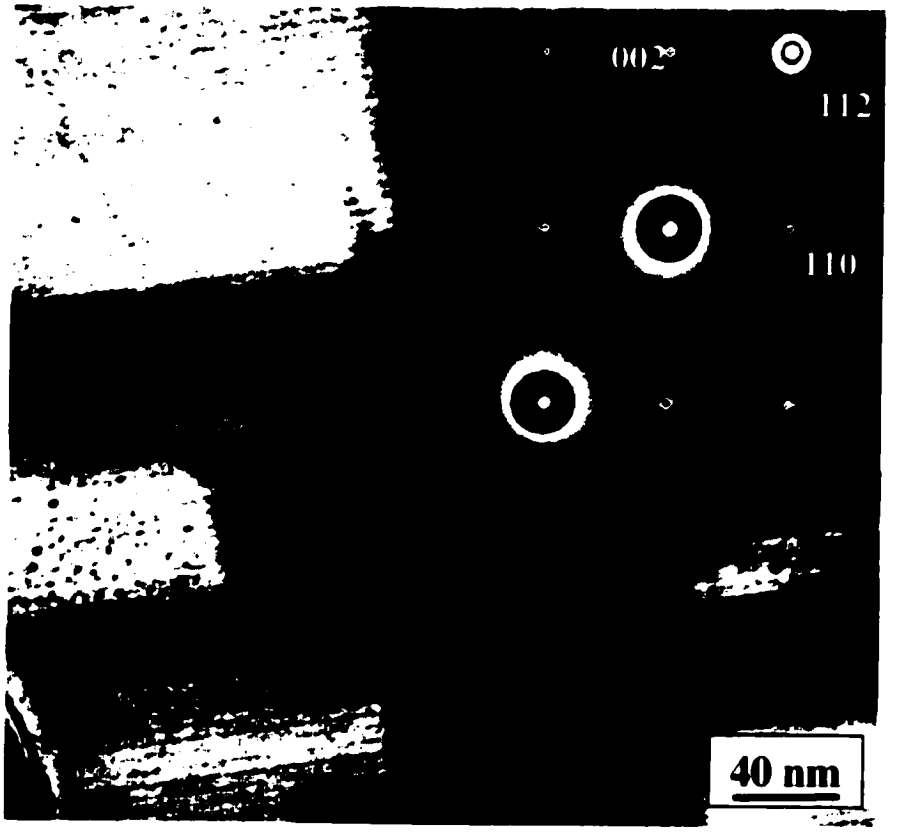

Fig. 25: Dark-field image and off-zone axis diffraction pattern of the (110) $SrTiO_3$ surface.

The diffraction pattern in Fig. 25 shows the presence of surface reconstruction, and the corresponding dark-field image shows a formation of a row-like structure that has formed along the [-110] direction on the surface as a result of annealing. These results are consistent with the investigation of the (110) surface reported by Brunen and Zegenhagen (1997). Our results are particularly interesting because they could potentially provide an insight into the reconstruction of charged oxide surfaces as a way of stabilizing such surfaces.

The type of the reconstruction produced on the $SrTiO_3$ surface is dependent more on the thermodynamics than on the kinetics of the process. Independent of the annealing time (ranging from 0.5 to 5 hrs), any of the reconstructions described above can be achieved on the same sample by simply changing the annealing temperatures. The amount of time necessary to reconstruct an ion-milled surface depends mainly on the degree of disorder and damage inflicted on the surface due to the sputtering process - i.e., increasing the amount of time spent ion-milling a sample consequently increases the length of time necessary to recover the surface. Another experimental aspect to be taken into consideration is the effect of thermal etching on surface stoichiometry. Thermal etching of $SrTiO_3$ surfaces at elevated temperatures was studied extensively by Tomashpolskii et al. (1981, 1985), and their findings suggest that depending on the temperature, SrO or TiO_2 is preferentially removed from the surface. In the range of the temperatures described here, the SrO evaporation is more likely (supported also by the XPS and UPS data from other groups, e.g. Nishimura et al. 1999; Heinrich 1983). This

process results in the essentially TiO_2 stoichiometry that we have observed for the 2x1 and the 4x2 surfaces (see above). Therefore, it is clear that the original unreconstructed (001) surface is extremely unstable at high temperatures, and it rearranges itself through a large amount of mass-transfer as well as surface reconstruction. Note that the experiments described here were conducted only under oxidizing environments; therefore the effect of oxygen partial pressure on this system is yet to be determined. It is unclear at this stage whether the reconstructions with similar dimensions observed under UHV conditions by other groups (see Table 6) are structurally identical to the ones obtained by our group or, or if certain pairs of UHV-annealed and oxidized surfaces just share the same unit cell periodicity.

Radiation Damage

In any HREM experiment involving a radiation sensitive structure (in this case the surface structure) it is important to estimate the extent and nature of radiation damage sustained by the TEM sample. The electrons that pass through a sample in the electron microscope can interact with atomic electrons as well as nuclei (Coulomb interactions). The resulting electron scattering processes involve changes in momentum and the transfer of a significant amount of energy to the sample. Reimer (1984) has discussed in detail possible elastic and inelastic processes occurring in an electron microscope experiment, though for our purposes we will consider only two possible radiation damage

mechanisms: radiolitic and knock-on damage. Thermal effects due to the excitation of phonons are insignificant, since in an electron microscope the temperature rise during the experiment is less than 100 °C (Buckett 1991).

Elastic scattering of electrons at high angles can cause a considerable amount of energy to be transferred to the specimen, although kinetic energy and momenta of the particles involved in the process are conserved. If this amount of energy is greater than a certain threshold energy, an atom can be displaced from its lattice site. This process is typically called knock-on (or ballistic) damage.

If the interaction of electrons with the specimen results in inelastic scattering, the kinetic energy is not conserved and is partially transformed into electronic excitation energy (while total energy and momenta are conserved). This process results in what is usually referred to as electronic excitation (or radiolitic) damage. Although the details of the electron induced damage mechanisms described above are different, their results are alike – in both cases, a significant amount of surface atoms desorb and the initially reconstructed surface becomes disordered; in the bulk, such damage creates point defects.

Radiation damage was not a significant problem in the case of the (2x1) reconstruction, as can be judged from the HREM images of the structure (see Fig. 11) obtained using JEOL 4010 microscope at ANL operated at 400kV. However, the (4x2) and the (6x2) structures damaged under the beam during the HREM experiments. Therefore, a series of experiments at different operating voltages (from 100 to 400 kV) were conducted to understand the nature of the electron beam damage. In each

experiment, the electron beam was focused on a particular area for 5 min (the typical length of time necessary to acquire focal series for HREM analysis), and diffraction patterns were recorded before and after exposure to the electron beam.

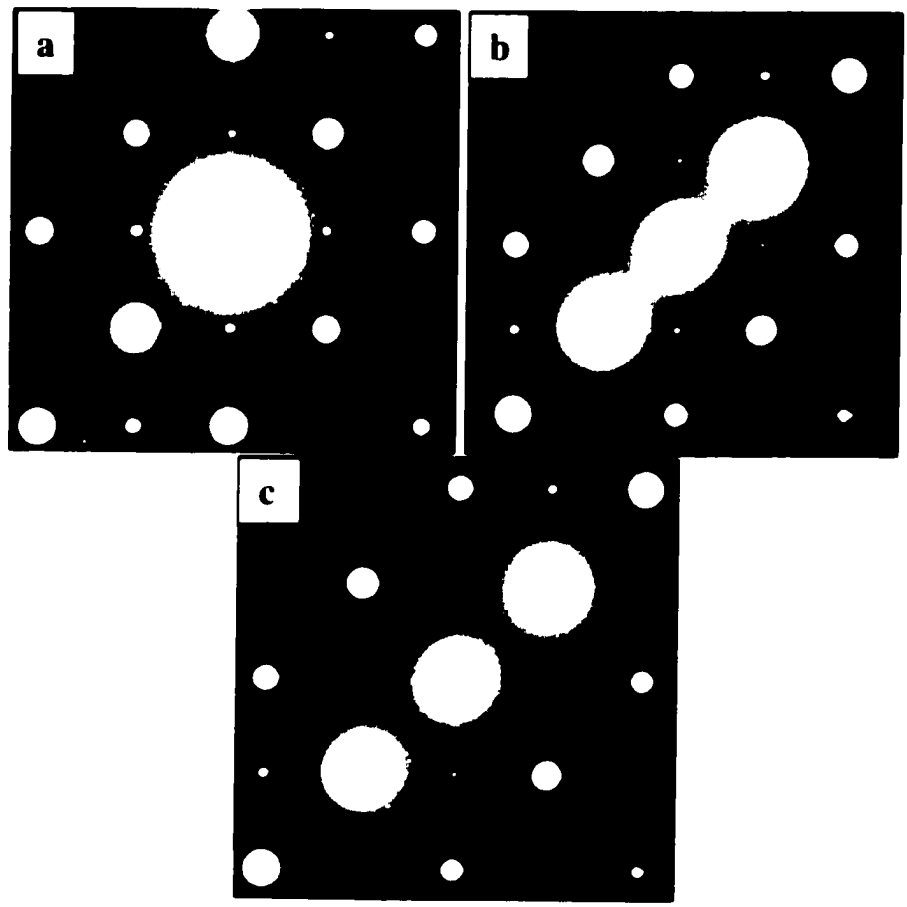

Fig. 26: Undamaged (4x2) surface (a) compared with radiation damage of the (4x2) reconstruction at (b) 100 kV and (c) 400 kV.

Fig. 26 shows radiation damage (discrete surface diffraction spots are replaced by streaks) of the (4x2) reconstruction at 100 kV (b) and 400 kV (c) compared with an undamaged surface (a). Fig. 27 shows similar radiation damage of the (6x2)

reconstruction at 100 kV (b) and 300 kV (c) compared with an undamaged surface (a). The fact that extent of damage experienced by these surfaces during high (300-400 kV) voltage experiments is virtually the same as that suffered during low voltage (100 kV) experiments suggests that the mechanism of electron beam damage is radiolitic. Attempts to obtain HREM images of the (4x2) and the (6x2) structures were unsuccessful due to electron beam damage.

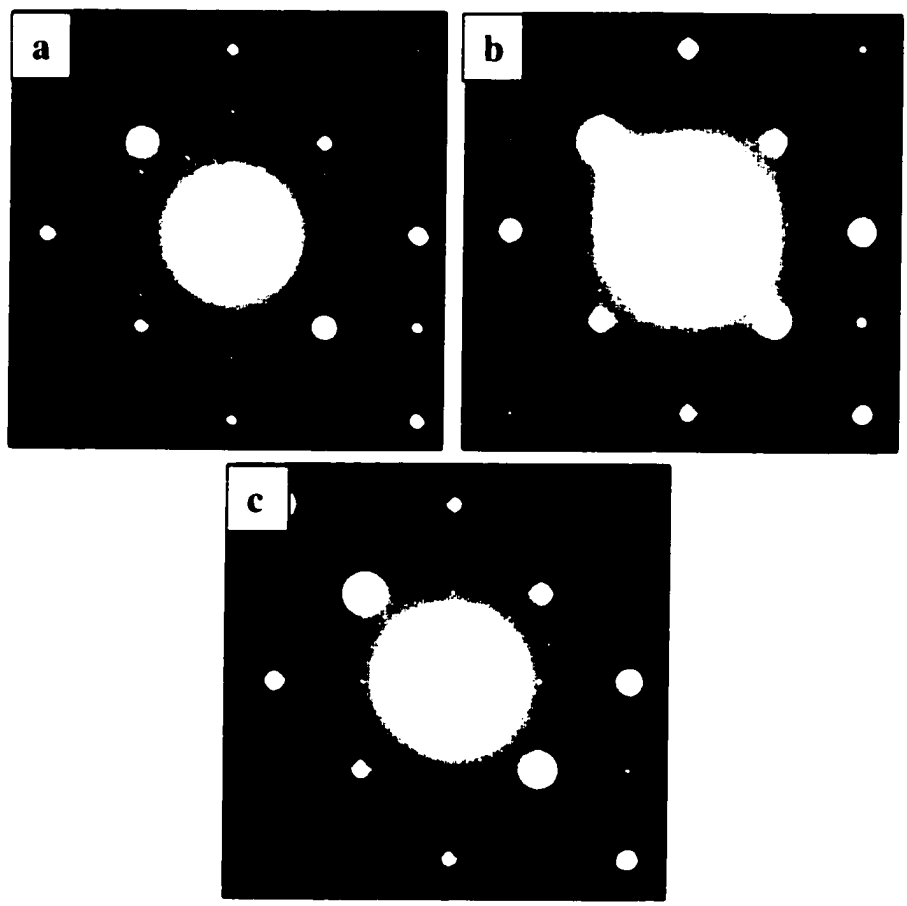

Fig. 27: Undamaged (6x2) surface (a) compared with radiation damage of the (6x2) reconstruction at (b) 100 kV and (c) 300 kV.

Surface Phase Diagram

Consistency and reproducibility of the above results, and most importantly the fact that the above structures can be obtained on the same sample just by changing the temperature of the experiment, suggest that a $SrTiO_3$ (001) surface phase diagram may be readily constructed. Deciding which two variables to use may appear to be somewhat difficult. While temperature must certainly be one variable, both surface stoichiometry and oxygen partial pressure could be considered plausible candidates for the second parameter. Currently, we have identified the stoichiometry of the (2x1) and the (4x2) surfaces (in both cases TiO_2), but are not completely sure about that of the (6x2) surface. Thus, it would be difficult to construct a phase diagram using compositional variations. However, we know that the above structures can be obtained both in air and in a flow of oxygen, suggesting that is a dependence, albeit quite weak, of the obtained structure on the partial pressure of oxygen under oxidizing conditions. Based on these observations and information from Ellingham diagrams of binary and ternary oxides, we propose a surface phase diagram for $SrTiO_3$ shown in Fig. 28.

The (4x2) structure is the most stable of the three structures and forms at low temperatures, whereas the (6x2) surface is the least stable. Although this diagram provides a 'recipe' for obtaining different surface structures under oxidizing conditions, further investigation is required to fully understand the influence of oxygen partial pressure on the system.

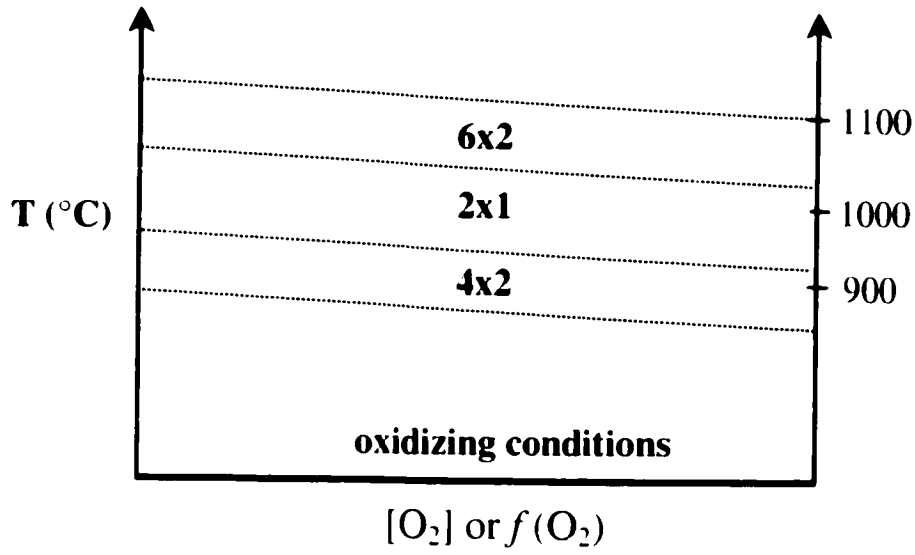

Fig. 28: Surface phase diagram for $SrTiO_3$ (001) surface.

Surface Structure Formation Rule

A bulk-like Ti-terminated $SrTiO_3$ (001) surface can be described in terms of a surface layer in which Ti atoms are coordinated by five oxygen atoms (four in-plane, one below) to form corner-sharing, truncated octahedra. As we have argued earlier for the (2x1) surface structure of $SrTiO_3$ (Erdman et al. 2002), stabilization of the under-coordinated Ti atoms can be accomplished by the formation of a single TiO_2 overlayer in the form of edge-shared (instead of corner-shared in the bulk) TiO_6 units. This new arrangement effectively screens the B-cations (Ti), minimizes surface dipoles and maximizes the coordination The same argument can be extended to the c(4x2) structure, where we find a similar TiO_2 overlayer.

We believe that a common mechanism drives the (4x2) and (2x1) structures to reconstruct in this particular fashion. The understanding of this mechanism would yield empirical rules to help elucidate the structuring and formation of other, related surfaces, and may be applicable not only to $SrTiO_3$ but, quite possibly, to perovskites in general.

While the structure of the overlayer (in particular Ti atom positions) can be unambiguously determined based on the scattering potential maps and refinement of the electron diffraction data, the structural relationship between the overlayer and the surface sub-layer require more careful attention. The stacking sequence of $SrTiO_3$ along [001] is ...-SrO-TiO_2-SrO-TiO_2-..., and the near-surface layer is TiO_2 rich. We will refer in the following discussion to the full TiO_2 bulk-like layer nearest to the surface; the structure of this sub-surface layer is clearly the strongest determinant in the placement of atoms in the overlayer. We consider three types of possible atomic sites:

1) "Coordinating" oxygen sites, which are directly above Ti atoms in the sub-surface layer. In the formation of an overlayer, we can reasonably expect these sites to be occupied so as to provide the Ti underneath with the missing sixth-coordinator and thus complete its octahedral coordination; we considered this fulfillment of octahedral coordination to be the "driving" force of an overlayer formation. For every 1x1 surface unit there is one site of this type.
2) The only reasonable location for Ti atoms in the overlayer is in between two "coordinating" oxygen sites, which further places it above another oxygen atom in the layer below. There are two sites of this type for every 1x1 surface unit.

3) We would expect Ti to possess at least 5 coordinating oxygen atoms. This requirement warrants a second possible oxygen site at the center of each 1x1 cell. We refer to this site as the "floating" oxygen site, because it is has no atom located directly underneath in the sub-surface layer. Thus, an oxygen atom located at this site is not directly bound to the layer below and consequently exhibits a great deal of positional flexibility in the vertical direction. Note that an oxygen atom at this site requires at least one of the adjacent Ti-sites to be occupied. There is one "floating" oxygen per 1x1 surface unit cell.

This list serves as a catalog of possible sites in a single overlayer; but not all of these sites must necessarily be occupied. Note that both the (2x1) and two c(4x2) structures are fully described in terms of these sites. Within this setup, a rationalization of an overlayer reconstruction is reduced to figuring out the occupancy of the possible sites. These occupancies, in turn, will be based on the various interdependencies that exist between the overlayer as well as site interaction with the subsurface layer.

Both the (2x1) and c(4x2) structures have overlayers that have TiO_2 stoichiometry in their overlayers. Further, given the catalog of possible atomic sites, both experimental structures are also characterized by *maximum occupancy*; the number of TiO_2 units in the overlayer is limited by the number of available oxygen sites (2 per 1x1 unit). At maximum occupancy, all oxygen sites (coordinating and floating) are occupied; with 2 cation sites per 1x1 surface unit, one half of all overlayer cation sites are occupied while

the other half is vacant. The advantages of maximum occupancy in the overlayer over partial occupancy are various: (a) the surface is generally more ordered, (b) we expect Ti to be 5-coordinated at least, which suggests tightly packed TiO_x units, and (c) below-maximum occupancy creates vacancies amongst the floating O sites. This in turn results in adjacent Ti-sites being less than 5 coordinated and thus unattractive to Ti occupation. In a below maximum scenario, we would expect the net-effect of (b) and (c) to be the formation of tightly packed islands of TiO_2 units, which would effectively emulate maximum occupancy at a local level.

We note the retention of edge-shared TiO_5 units, yielding a charge neutral reconstructed surface with the stoichiometry Ti_2O_4 in both the (2x1) and (4x2) structures. These results indicate that an edge-shared assembly of TiO_x units on the surface, analogous to creation of 'block-structures' in Nb_2O_{5-x} and other ReO_3-type bulk oxide structures, provides additional modes for rearrangement to lower energy configurations and controls the surface structure of $SrTiO_3$.

We suggest that this structure formation rule can be extended to perovskites in general. One could compare this result for perovskite surfaces to the rules of sp^3 bonding for semiconductor surfaces, an idea that was first suggested for Si surfaces but quickly became widely used to explain surface structure formation in other semiconductors. This suggests that many of the concepts of bulk chemistry can also be applied to surfaces, coupled with minimizing surface dipole moments and maximizing coordination. Different specific results will occur depending upon the bonding character and structural

rules, for instance delocalized electron states in metals, directional sp^2 or sp^3 in many semiconductors and block structures in oxides.

CHAPTER 5

INVESTIGATION OF $Mg_3(VO_4)_2$ SINGLE CRYSTAL SURFACES

The search for new catalysts and an understanding of the selective oxidation of alkanes have been active research areas for a number of years. Alkanes are generally less reactive than alkenes and dienes; therefore, at the high temperatures needed to activate alkanes the following reactions occur (the drawback to this process is production of several by-products):

$$C_nH_{2n+2} + \text{heat} \rightarrow C_nH_{2n} + H_2 \qquad \text{(thermal cracking)}$$

$$C_nH_{2n+2} + O_2 \rightarrow CO_x + H_2O \qquad \text{(combustion)}$$

A more favorable route to the formation of alkenes from alkanes is oxidative dehydrogenation. The oxide catalyst's surface in this case could provide a stable and controlled source of reactive oxygen, which alters the pathways leading to the formation of combustion products by reducing the reaction temperature. Oxidative dehydrogenation uses milder conditions (as compared to thermal cracking) for the selective conversion of alkanes.

The mixed oxides of vanadium, magnesium and molybdenum have been found to be effective catalysts for numerous catalytic reactions. Magnesium ortho-vanadate has been found to be both active and selective in the dehydrogenation of butane and propane

(Chaar et al. 1987; Soenen, Hermann and Volta 1996). The bulk structure of $Mg_3(VO_4)_2$ can be described in terms of chains of edge-sharing MgO_6 units linked together by isolated VO_4^{3-} tetrahedra (Krishnamachari and Calvo 1971) (Fig. 29). The bulk structure can alternatively be described as an orthorhombic Mg-deficient spinel-type structure $(Mg_3\square)^{O}V_2^{T}O_8$ (where T: tetrahedral site, O: octahedral site,□: cation vacancy).

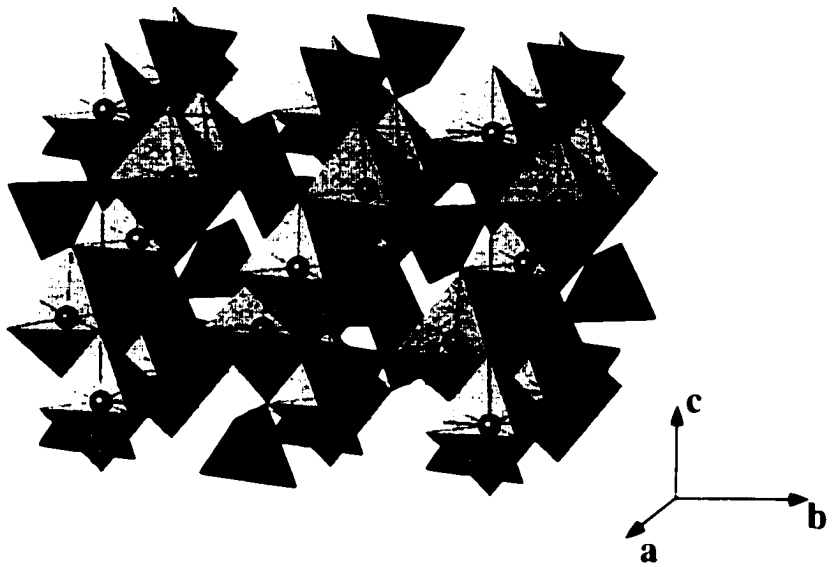

Fig. 29: The bulk structure of $Mg_3(VO_4)_2$ (a=6.0533, b=11.4426, c=8.3303 Å, space group *Cmca*). The chains of edge-sharing MgO_6 octahedra are linked together by isolated VO_4^{3-} tetrahedral. The unit cell is outlined.

Previous studies have provided some insight into important factors which might influence the catalyst's performance. It is apparent that the observed product distribution depends on the nature of the catalyst as well as on the nature of the alkane. Some groups, for instance, have reported that pyrovanadate ($Mg_2V_2O_7$) is more selective than ortho-

vanadate for oxidative dehydrogenation of propane to propene (Soenen, Hermann and Volta 1996; Gao et al. 1994). These authors suggested that the high selectivity of pyrovanadate is due to corner-shared tetrahedral units of $V_2O_7^{-4}$. A majority of the researchers agrees that the rate-limiting step for the dehydrogenation reaction is the alkane activation by breakage of a C-H bond.

In the early study by Chaar et al. (1987) it was proposed that the high selectivity of the Mg-V-O system for oxidative dehydrogenation of butane is due to the presence of both magnesium oxide and vanadium oxide in the magnesium ortho-vanadate compound. The authors proposed a mechanism where the V-O centers are responsible for butane activation, while the MgO component modifies (decreases) the acidity of vanadium oxide. This results in a weak adsorption of butenes and butadienes on the basic oxide surface and reduces their reactivity (they become significant products). Another study by Michalakos et al. (1993) explored selectivity patterns for alkane oxidation over the ortho-vanadate catalyst surface assuming that the reaction occurred on the low-index crystallographic planes of $Mg_3(VO_4)_2$. The authors proposed that the active sites of these catalysts involve isolated VO_4^{3-} tetrahedral units on the surface (which are bonded similarly to the bulk structure), such that the oxygen ions are bridged between V and Mg ions.

In a more recent study, X. Wang et al. (1998a) showed that the structures of $Mg_3(VO_4)_2$ and the reduced phase $Mg_3V_2O_6$ are similar (see Fig. 30). Magnesium ortho-vanadate remains a single crystal upon reduction, suggesting that the catalyst can cycle between oxidized and reduced forms. During reduction, the cation-deficient

orthorhombic spinel, $Mg_3(VO_4)_2$, is reduced to a cation-stuffed *cubic* spinel, $Mg_3V_2O_6$, by a topochemical transformation. In this reaction, the vanadium atoms migrate from tetrahedral sites to octahedral interstices while the octahedral Mg(2) atoms rearrange to equally occupy the tetrahedral 8a and octahedral 16c sites (Wang et al. 1998a). Ruffner et al. (2000) has successfully grown thin films of $Mg_3(VO_4)_2$, that exhibit similar topochemical behavior when reduction occurs via propane.

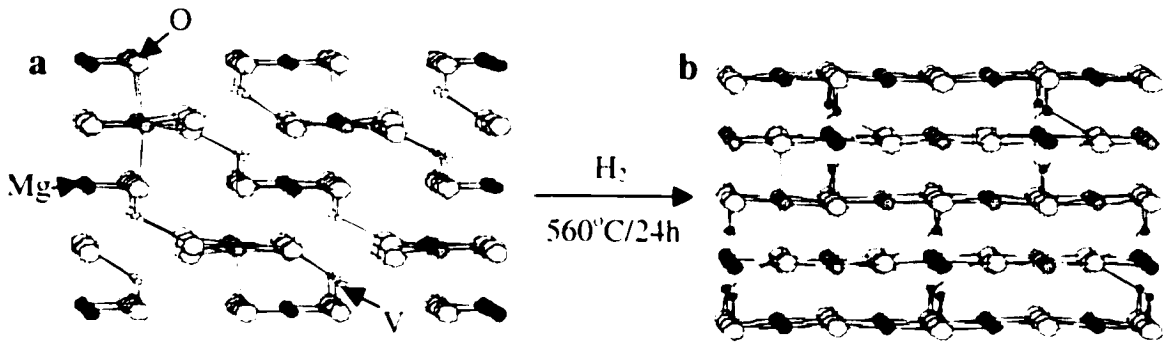

Fig. 30: Comparison between the bulk structure of (a) $Mg_3(VO_4)_2$ viewed along the [100] direction, and (b) the reduced compound $Mg_3V_2O_6$ viewed along the [011] direction.

Other studies by Prof. K.R. Poeppelmeier's group (Harding et al. 1993; Wang et al. 1998b; Wang et al. 1998c) showed that incorporation of molybdenum oxide into $Mg_3(VO_4)_2$ results in the new compound $Mg_{2.5}MoVO_8$ that maintains the high catalytic dehydrogenation selectivity of magnesium ortho-vanadate but has higher conversion rates.

One of the main issues in catalysis is determining the active sites on which the adsorption/desorption and oxidation/reduction reactions occur. Homogeneous catalysis is usually characterized by a single active site, where 'oxidative addition' and 'reductive elimination' reactions proceed. Heterogeneous catalysts, on the other hand, usually exhibit multi-site chemistry (more than a single active metal site), which can promote *'oxidative elimination'* and *'reductive addition'*. Multimetallic systems such as $Mg_3(VO_4)_2$ and $Mg_{2.5}VMoO_8$ oxidize hydrocarbons through incorporation of the above dual function. The general idea is the following: a cation in a high oxidation state (first site) is reduced by *reductive addition* of the hydrocarbon to a metal-oxygen surface (in the absence of gaseous oxygen); a cation in a low oxidation state (second site) controls the reaction with oxygen, and *oxidative elimination* (i.e. alkane is oxidized to alkene and leaves the surface) completes the reaction.

Despite numerous studies, the nature of active sites on the surface and the reaction pathway for oxidative dehydrogenation of alkanes on the surfaces of Mg-V-O catalysts are unknown. Our approach has been to investigate single crystal samples of $Mg_3(VO_4)_2$ using TEM and XPS to obtain both structural/morphological and chemical information, with the ultimate goal of elucidating the surface structure of these samples under various oxidizing conditions. The important objective of this study is to identify connections between the kinetic information obtained by various groups and the understanding of catalytic reactions on the molecular level. Our results for this system were not as successful as those for the previous two oxide systems described in this thesis, i.e. no surface structures were solved or even observed on the single crystals of $Mg_3(VO_4)_2$.

Even so, a significant amount of knowledge and experience has been accumulated on the nature of interactions between the components of this system during high temperature anneals as well as the surface morphology and chemistry produced by these heat treatments.

The structure of this chapter is as follows: first the single crystal growth procedure will be briefly described (single crystals used in the TEM experiments were grown by J.D. Pless in Prof. K.R. Poeppelmeier's lab). Afterwards, the TEM and XPS experiments for various crystal faces and the interpretation of their results will be presented.

Single Crystal Growth

Large single-crystals of $Mg_3(VO_4)_2$ are challenging to grow because this compound melts incongruently (see Fig. 31). Wang et al. (1998a) have grown single crystals using the flux method. The produced crystals were imbedded in flux and are too small ($\leq$ 2mm) for surface characterization. In contrast to the flux method, the optical floating zone method (in the traveling solvent zone configuration) can be used to grow large crystals of incongruently melting systems. Some of the advantages provided by the optical floating zone method include: a crucible free operating mode that minimizes or prevents contamination, and a steep temperature gradient along the vertical direction that allows faster and more stable crystal growth.

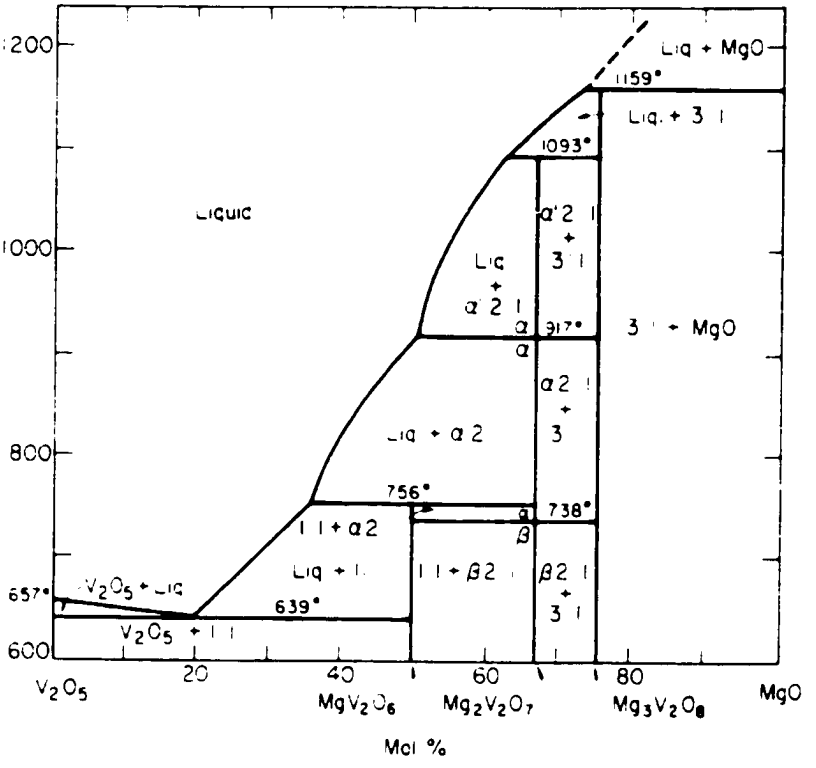

Fig. 31: Phase diagram of MgO – V_2O_5 system (Wollast and Taizart 1969).

The single crystal growth experiments were carried out by J.D. Pless using an optical image furnace (CSI FZ-T-10000-H-VI-VP, Crystal Systems, Inc., Japan), equipped with four 300W tungsten halide lamps and four elliptical mirrors. The general configuration of the experimental setup is shown in Fig. 32a. One of the most important requirements for successful crystal growth is the development of a stable liquid zone, which is achieved by using dense, chemically homogeneous, straight, and precisely aligned feed and support rods. Crystal growth begins by melting the bottom of the feed rod and the top of the support rod, forming a liquid zone between the counter-rotating

feed and support rods. $Mg_3(VO_4)_2$ undergoes peritectic melting, decomposing into crystalline magnesium oxide and a liquid of peritectic liquidus composition (Fig. 32b) as seen in the phase diagram. Reduction of the amount of power supplied to the halogen lamps to a level that permits undisturbed rotation of the rods prevents volatilization of the liquid. The crystal growth starts with MgO crystallization on top of the support rod and proceeds with the upward translation of the mirror stage. The liquid composition continuously changes until a steady state is established between the liquid and the crystallized MgO. Once this steady state is established, $Mg_3(VO_4)_2$ starts crystallizing. The crystallized $Mg_3(VO_4)_2$ is simultaneously replenished from the feed rod. The crystal growth is performed slowly to maintain the equilibrium conditions necessary for the growth of a single crystal of $Mg_3(VO_4)_2$ from a liquid of a different composition. For further experimental details see Pless et al. (2002).

An example of a transparent, orange-brown color single crystal of $Mg_3(VO_4)_2$ grown by this technique is shown in Fig. 33. The obtained single crystals are significantly larger (typical crystals were 5mm in diameter and 55mm long) than the crystals grown by the flux method and develop a single facet during growth (Fig. 33).

EBSD was implemented to verify the crystallographic orientation of naturally occurring facets on $Mg_3(VO_4)_2$ single crystals. The resulting EBSD pattern is shown in Fig. 34. The obtained pattern corresponds to the [20-1] zone axis, confirming the results from Laue diffraction (Pless et al. 2002).

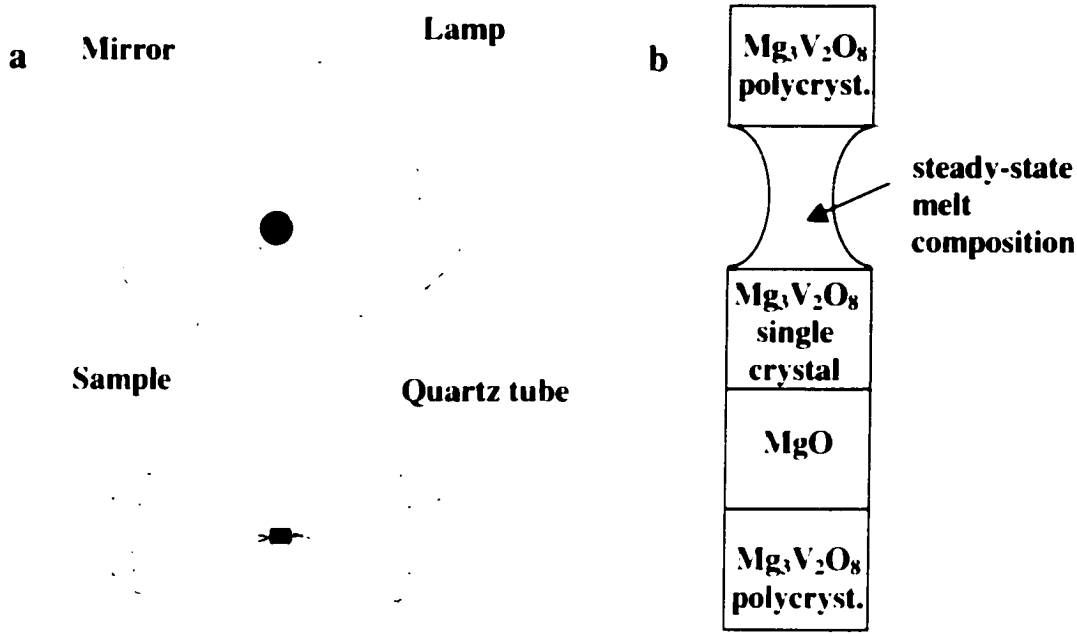

Fig. 32: (a) Schematic of four-mirror furnace and (b) stages of crystal growth (growth direction is upwards) for $Mg_3(VO_4)_2$ single crystal.

Fig. 33: An example single crystal of $Mg_3(VO_4)_2$ grown by floating zone technique. Predominant facet that forms during the crystal growth is clearly seen.

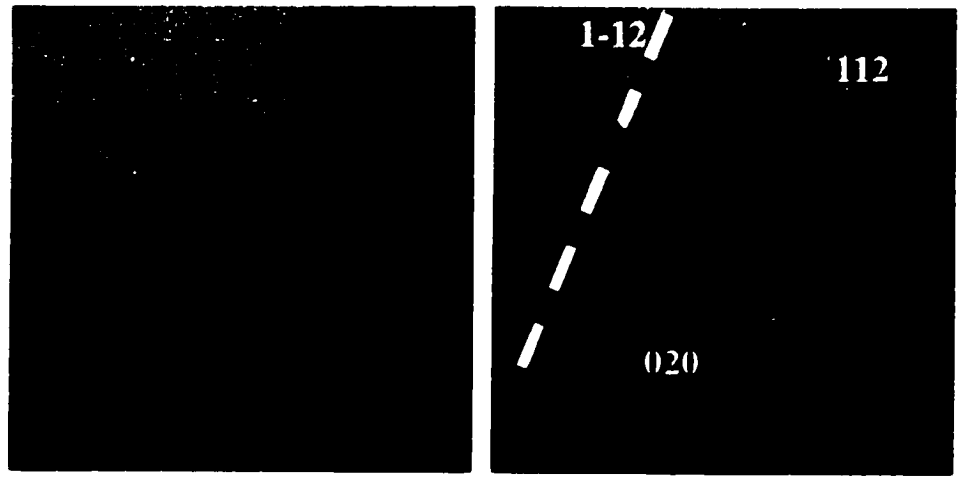

Fig. 34: EBSD pattern of [20-1] orientation of $Mg_3(VO_4)_2$ single crystal: (a) original pattern, (b) interpretation of the Kikuchi lines in terms of crystal directions.

TEM and XPS Studies

The distinct predominant facet of the crystals grown by floating zone method as well as some of the cleavage planes were used to orient the crystals for TEM sample preparation. The resulting TEM samples were annealed in a tube furnace in a flow of oxygen under various conditions to investigate the effects of annealing time, atmosphere and temperature on the surface structure and morphology. An annealing temperature range between 450° and 750°C was chosen in order to assure a significant amount of surface diffusion but limit bulk diffusion. The $Mg_3(VO_4)_2$ crystals were annealed for short and long periods of time (from 2 to 10 hrs) to study both thermodynamic and kinetic effects of the annealing process on the surface restructuring. Off zone-axis electron diffraction patterns, necessary for surface diffraction data analysis, as well as

images of the TEM sample morphology were obtained using a H8100 Hitachi electron microscope operated at 200kV in the EPIC facility at Northwestern University. XPS experiments were performed to determine surface composition and investigate possible segregation of impurities or structure elements on the surface.

[20-1] Crystal Orientation

As was mentioned above, [20-1] is the orientation of the naturally occurring face on the crystals grown by the floating zone technique; therefore, investigation of this particular crystal orientation was a natural choice. After ion milling and prior to annealing, the samples exhibit some disorder and strain on the surface as indicated by an amorphous ring in the diffraction pattern as well as band contours. Samples annealed at 450°C still showed a significant amount of disorder on the surface. Although the subsequent series of annealing experiments at 550°, 650° and 750°C (in each case the annealing lasted 2 hrs) did not produce any surface reconstruction (Fig. 35), these heat treatments did induce recrystallization of the sample surface. Moreover, samples annealed at 750°C showed formation of MgO islands on the surface of the sample (Fig. 36).

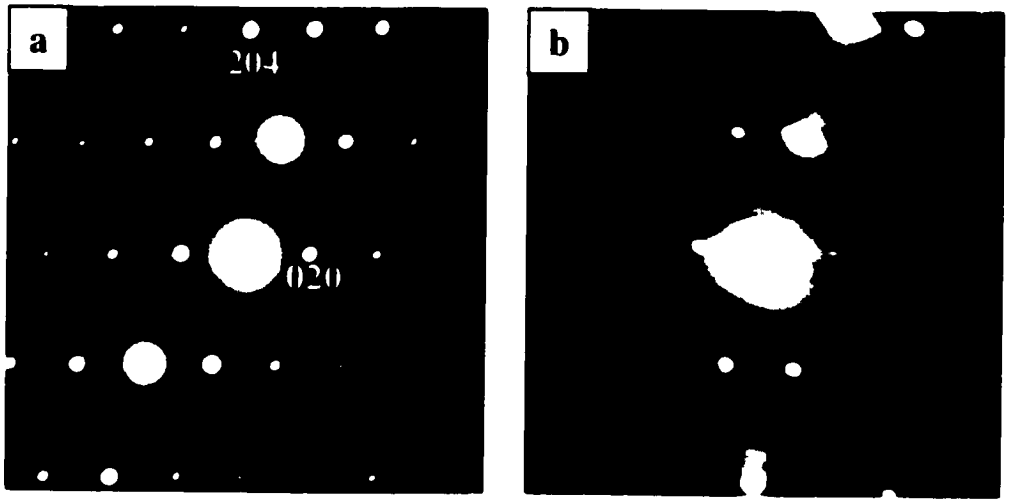

Fig. 35: Off zone axis diffraction patterns of [20-1] $Mg_3(VO_4)_2$ single crystal samples annealed at (a) 550°C and (b) 650°C.

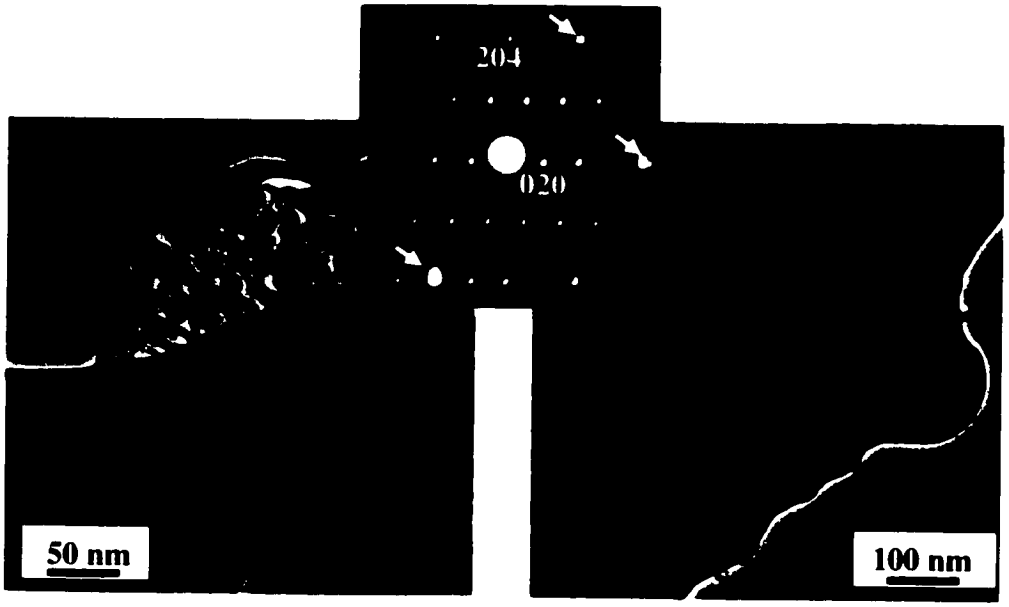

Fig. 36: [20-1] $Mg_3(VO_4)_2$ single crystal samples annealed at 750°C. The images show formation of MgO islands on the surface of the sample; inset shows typical diffraction pattern with extra spots (pointed with arrows) from MgO(111).

The nucleation of MgO islands on the surface suggested that at the elevated temperatures used in our experiments, there is a preferential enrichment of the surface in Mg over V (essentially changing the surface stoichiometry). In order to investigate whether these observations depended on annealing time (long vs. short annealing) and/or temperature several XPS experiments were performed (with Dr. C.Y. Kim in Prof. M.J. Bedzyk's lab). We have also investigated the possibility of modifying the surface stoichiometry back to a stoichiometric surface by annealing the single crystal samples in the presence of $Mg_3(VO_4)_2$ powder or V_2O_5 powder. The idea behind these experiments was to increase the partial pressure of V_2O_5 in the system to prevent enrichment of the surface with Mg (assuming that V_2O_5 or some other type of V_xO_y was the more volatile component of the system). Initial XPS results on the samples annealed for 2 hrs in O_2 (without $Mg_3(VO_4)_2$ or V_2O_5 powder) suggested that there is some enrichment of the surface in Mg over V, essentially confirming the TEM results (see above). To achieve more conclusive results regarding temperature/time effects and ensure equilibrium reaction conditions, samples were also annealed at 550 and 650°C for 10 hrs. The results of the XPS measurements conducted on these samples are shown in Fig. 37-39.

Fig. 37 shows an XPS spectrum from samples annealed in oxygen at 550°C for 10 hrs with (a) V_2O_5 powder and (b) $Mg_3V_2O_8$ powder compared with the spectrum of a sample annealed in (c) only O_2 for 2 hrs. While the presence of Si and C on the surface of the samples can be attributed to the use of silicon carbide as a polishing material during the sample preparation process (carbon is also present due to the adsorption of CO_x), the

presence of Ca is due to impurity of the starting materials (0.007% Ca in MgO and 0.27% Ca in V_2O_5) from which the crystal rods were prepared. It can be clearly seen that the Ca peak grows with longer annealing time, suggesting surface segregation of impurities. Although no quantitative analysis was done on this XPS data, it can be clearly seen from Fig. 37 that in the sample annealed with V_2O_5 powder the ratio of Mg to V is smaller than in the other two samples. This result suggests that annealing with V_2O_5 powder can in fact improve the experimental setup and help obtain a more nearly stoichiometric surface.

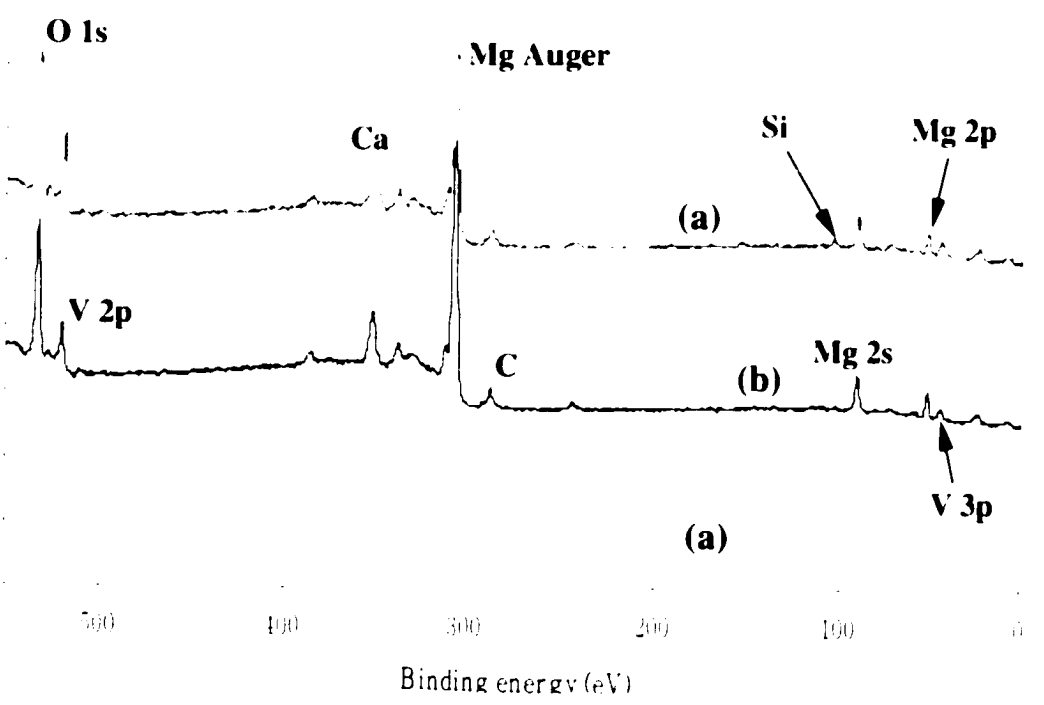

Fig. 37: XPS spectrum from samples annealed in oxygen at 550°C for 10 hrs with (a) V_2O_5 powder and (b) $Mg_3V_2O_8$ powder compared with the spectrum of a sample annealed in (c) only O_2 for 2 hrs.

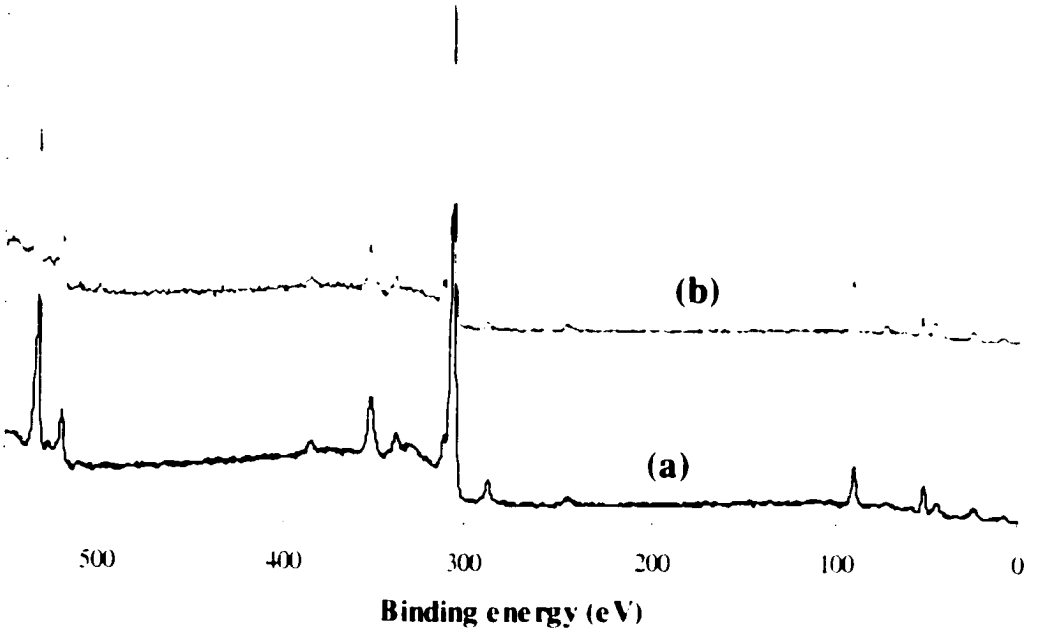

Fig. 38: Effects of different annealing temperatures on the surface stoichiometry of $Mg_3(VO_4)_2$ single crystals: annealing with $Mg_3V_2O_8$ powder at (a) 550 °C and (b) 650 °C.

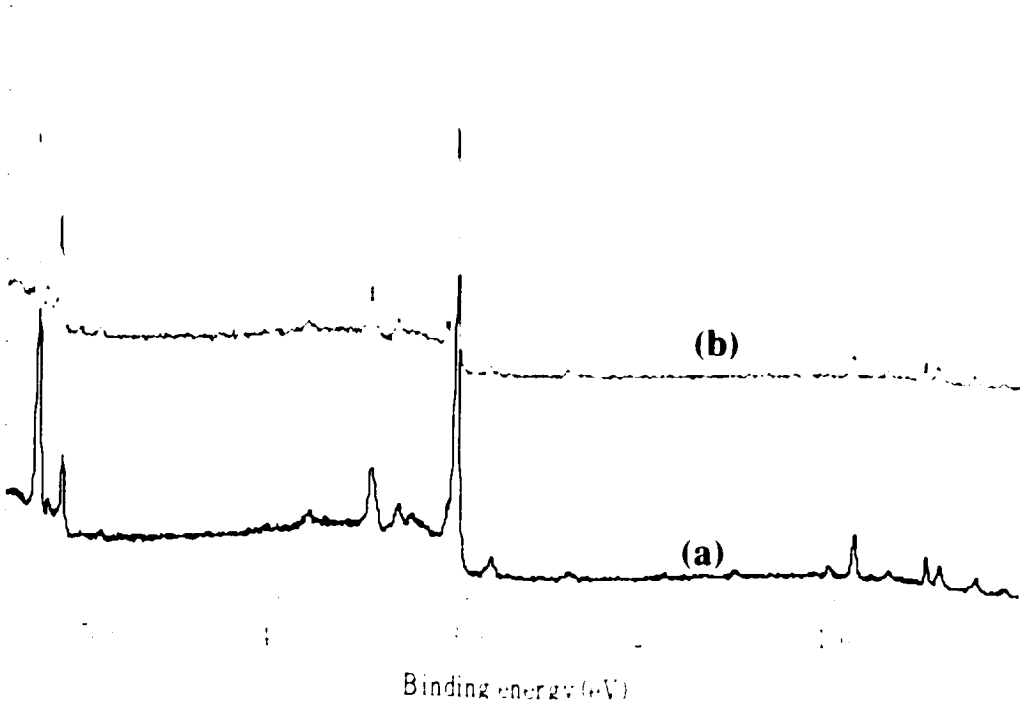

Fig. 39: Effects of different annealing temperatures on the surface stoichiometry of $Mg_3(VO_4)_2$ single crystals: annealing with V_2O_5 powder at (a) 550 and (b) 650 C.

Fig. 38 and 39 show the effects of different annealing temperatures on the surface stoichiometry of $Mg_3(VO_4)_2$ single crystals. In the case of annealing with $Mg_3V_2O_8$ powder (Fig. 38), the loss of V_xO_y is enhanced at higher temperature (which is not surprising since V_2O_5 melts at 657°C in air), increasing the Mg to V ratio on the surface. However, results obtained by annealing with V_2O_5 (Fig. 39) at higher temperatures demonstrate a further change toward surface compositions that are more stoichiometric

than those obtained by lower temperature anneals. This is rationalized by a higher vapor pressure of V_2O_5 at higher temperatures.

[100] Orientation

The [100] oriented surface was obtained from a cleavage plane. As described above, prior to annealing, the sample surface was disordered and strained. The [100] sample was annealed in O_2 for 2 hrs at 550 °C. The resulting off-zone axis diffraction pattern is presented in Fig. 40. No reconstruction was observed on this surface under these annealing conditions. Further annealing experiments (higher temperature/longer annealing time) were not attempted on this sample because of the possible enrichment of the surface with Mg and nucleation of MgO islands, as observed on the [20-1] sample.

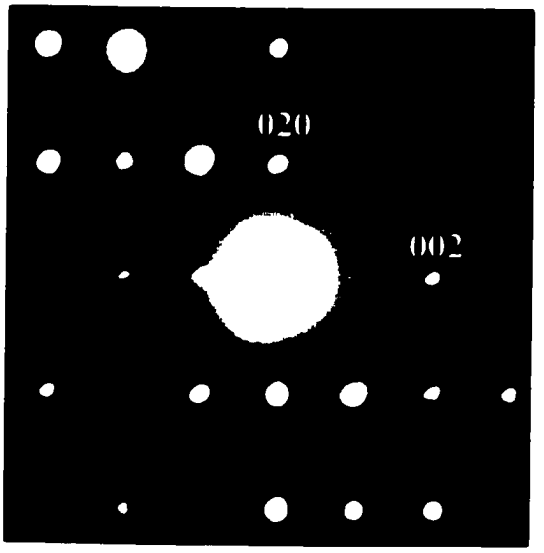

Fig. 40: Off-zone axis diffraction pattern of the [100] $Mg_3(VO_4)_2$ crystal annealed at 550°C.

Growth Direction - [010] Orientation

The [010] orientation was obtained from a plane of the crystal representing the growth direction. The samples were annealed at 550°C and 650°C for 2 hrs in O_2. Neither of the annealing conditions resulted in any surface reconstruction (see Fig. 41), however the sample annealed at 650°C showed once again areas where MgO nucleation and island formation had begun.

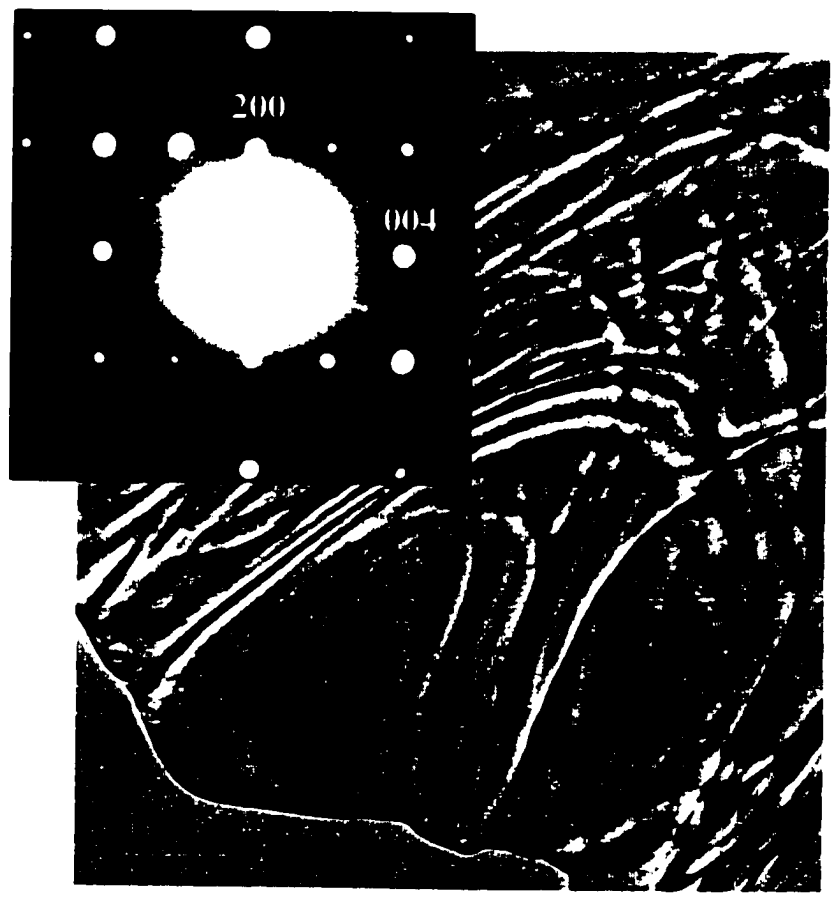

Fig. 41: Image and off-zone axis diffraction pattern of the [010] $Mg_3(VO_4)_2$ single crystal after annealing in O_2. Bend contours are clearly seen on the sample.

The possibility of manipulating the surface stoichiometry of [010] samples was also tested by adding V_2O_5 powder into the system during the annealing as described above. Two different annealing temperatures were tested: above (700°C) and below (600°C) the melting temperature of V_2O_5. First an [010] sample was annealed in a crucible with V_2O_5 powder at 600°C for 10 hrs in O_2. The sample showed no significant changes in surface structure (the diffraction pattern was similar to the ones obtained before, see Fig. 41). However, no nucleation of MgO was seen on the surface after the annealing, suggesting that annealing with V_2O_5 powder (thus increasing V_2O_5 partial pressure in the system) can prevent significant surface enrichment in MgO. On the other hand, annealing an [010] sample with V_2O_5 at 700°C caused the sample to coarsen and become contaminated with V_2O_5 (most probably condensing on the sample during the cool-down) as shown in Fig. 42.

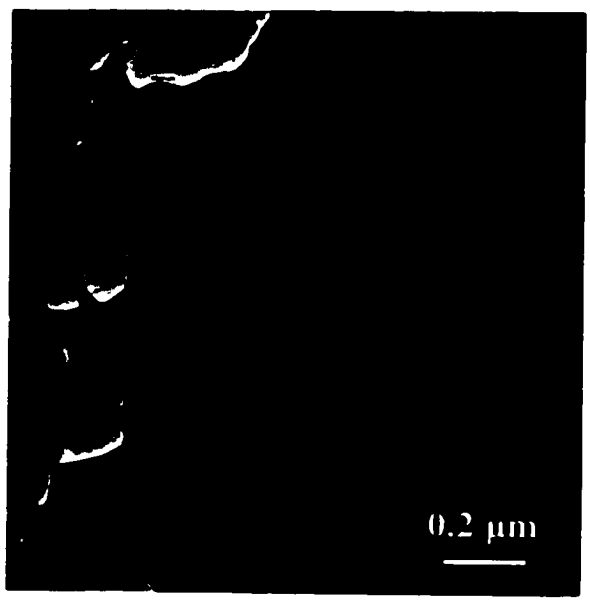

Fig. 42: $Mg_3(VO_4)_2$ sample annealed at 700°C with V_2O_5 powder.

Conclusions

In order to investigate the structure of $Mg_3(VO_4)_2$ single crystal surfaces we have obtained single crystal TEM samples with a well-defined orientations and annealed the samples in various temperature regimes with the intent of obtaining flat, reconstructed surfaces. While this approach has proved successful for other oxide systems (e.g. $SrTiO_3$ (see Chapter 4) and MgO (Plass et al. 1998)), the results presented for $Mg_3(VO_4)_2$ suggest that it will be difficult to obtain a single crystal sample with flat or faceted surface, while simultaneously controlling the surface composition. The XPS results in conjunction with TEM observations showed that during the annealing process, the surface is modified: during prolonged annealing (above 5 hrs) the volatile component in the system, V_xO_y, sublimes from the surface which causes subsequent enrichment of the surface with the more refractory component, MgO. These processes make it particularly difficult to maintain a stoichiometric surface. A possible solution to this problem lies in the use of V_2O_5 powder during the annealing to increase the partial pressure of vanadium oxide in the system. However, care should be taken in choosing the annealing temperature, since annealing above the melting temperature of vanadium oxide will cause sample contamination. Although annealing of the samples with V_2O_5 powder did prevent changes in surface stoichiometry, under the conditions used in these experiments surface reconstruction of $Mg_3(VO_4)_2$ was not observed.

CHAPTER 6

CONCLUSIONS AND SUGGESTIONS OF FUTURE WORK

Surface structures are vital for understanding a variety of technologically important processes such as catalysis, thin film growth and essentially any other reaction that occurs at the interface between a solid and a liquid or gas phase. The research approach described in this manuscript has opened new frontiers in the discovery and characterization of oxide surface structures. The combination of Direct Methods applied to electron/X-ray diffraction data and theoretical DFT calculations for 3D surface structure determination, as well as the morphological and atomic-scale details of the structure obtained with TEM provide a multidimensional method for surface structure determination.

Our solution of the NiO(111) surface structure was a significant step in the understanding of polar oxide surface structure and proved yet again experimentally what theoreticians claimed for many years –polar oxide surfaces are readily stabilized via faceting and reconstruction. Although our structure solution is somewhat different than the oversimplified octopolar reconstruction that has been proposed for an NaCl-type structure before (Wolf 1992), it does exhibit similar features and can be described as a complex arrangement of octopolar units on the surface.

We have developed highly reproducible 'recipes' for preparation of reconstructed and faceted $SrTiO_3$ (001) surfaces and have resolved the 2x1 and the 4x2 surface

structures. Both structures terminate with two surface layers of TiO_2 composition – the subsurface layer is a bulk-like TiO_2 layer whereas the overlayer exhibits significant structural rearrangement. Although the surface structure is very different from the bulk perovskite structure, in the hindsight, it might have been predicted by considering bulk crystallography of related ReO_3 – type structures. The ReO_3 – type structures can exhibit different structures upon reduction by creating blocks of edge-shearing octahedra, the same sort of rearrangement we observe on the surface of $SrTiO_3$. Based on the obtained structure solutions we have formulated the rules for surface reconstruction in $SrTiO_3$ (and perhaps perovskites in general), which are closely related to the concepts of bulk crystallography and include maintaining maximum coordination and minimization of dipole moments.

Future directions for the $SrTiO_3$ system could include investigation of polar surfaces, such as (110) and (111) orientations. Preliminary results (see Chapter 4) suggest that the (110) surface reconstructs under oxidizing environments at high temperatures, and the (111) surface is currently under investigation as well. It would also be interesting to see whether the reconstructions with the same periodicity we observed appear under reducing conditions such as UHV or H_2 environments (in fact several groups have already reported on $SrTiO_3$ reconstructions under these conditions as shown in Table 6). This sort of investigation would answer questions regarding the influence of oxygen partial pressure on surface structure formation.

Investigation of the $Mg_3(VO_4)_2$ single crystal surfaces proved to be extremely complex, which was expected of a material that functions as an oxidation catalyst.

Obtaining adequate TEM specimens with stoichiometric and flat surfaces was found to be particularly difficult. Although TEM and XPS experiments provided insight into changes in surface stoichiometry and morphology upon annealing, no surface reconstruction was observed on any of the three investigated surfaces (different crystallographic orientations treated with a variety of annealing times, temperatures and atmospheric conditions).

With respect to future work on this system, it may be advisable to develop parallel experiments combining the typical single crystal surface diffraction and gas cell experiments with powders. During preliminary studies a significant amount of kinetic data has been obtained by J.D. Pless on $Mg_3(VO_4)_2$ and other variants (with Mo) at Dow Chemical Company. These data provide an opportunity to correlate between the pilot plant reactor and in-situ catalytic reaction experiments conducted in a laboratory environment. One could use alumina or silica film support (instead of carbon films) that do not react or suffer damage at high temperatures. Experiments using a gas cell (attached directly to SPEAR equipment (Collazo-Davila 1995)) would provide more accurate information about the catalytic reactions and would also allow sample chemistry to be monitored by XPS. These experiments would be similar to the in-situ approach used by Gai and coworkers (1997, 1998) at DuPont, although here the investigation would focus on reaction products and intermediates instead of reaction kinetics. While in the experiments performed at DuPont the reaction occurs in the microscope during the imaging process, here the reaction would occur in the gas cell and, through UHV transfer, be investigated with UHV-HREM.

The major obstacle encountered during the work presented here has been obtaining adequate single crystal samples. In some cases, single crystal growth using the traveling zone furnace can provide the single crystals necessary for TEM experiments. As this research moves on to studies of surface structures of more complex oxide systems however, the issue of obtaining good single crystals will always be a challenge. It is thus imperative in the early stages of this research to choose appropriate model systems, e.g. $SrTiO_3$, and relate the knowledge gained about these systems to a wider range of materials with similar structures.

BIBLIOGRAPHY

Ai, X. R. (1992). "Electron-induced surface radiation damage in V_2O_5, ReO_3 and CaF_2," Ph.D. thesis, Northwestern University.

Aruta, C. "Structure of superconducting $[BaCuO_x]_2/[CaCuO_2]_n$ superlattices on $SrTiO_3$ (001) investigated by X-ray scattering." *Phys. Stat. Solidi A* 183 (2001): 353-364.

Banares, M.A. "Supported metal oxide and other catalysts for ethane conversion: a review." *Cat. Today* 51 (1999): 319-348.

Barbier, A., Mocuta, C., Kuhlenbeck, H., Peters, K.F., Richter, B., and Renaud, G. "Atomic structure of the polar NiO(111)-p(2x2) surface." *Phys. Rev. Lett.* 84 (2000): 2897-2900.

Barbier, A., Renaud, G., Mocuta, C., and Stierle, A. "Structural investigation of the dynamics of the NiO(111) surface by GIXS." *Surf. Sci.* 433-435 (1999): 761-764.

Bengu, E., Plass, R., Marks, L.D., Ichihashi, P., Ajayan, M., and Iijima, S. "Imaging the dimers in Si (111) - (7x7)." *Phys. Rev. Lett.* 77 (1996): 4226-4228.

Bertaut, F. "The electrostatic term of surface energy." *Compt. Rend.* 246 (1958): 3447-3450.

Bonnell, D.A. "Scanning tunneling microscopy and spectroscopy of oxide surfaces." *Prog. Surf. Sci.* 57 (1998): 187-252.

Brunen, J., and Zegenhagen, J. "Investigation of the $SrTiO_3$ (110) surface by means of LEED, scanning tunneling microscopy and Auger spectroscopy." *Surf. Sci.* 389 (1997): 349-365.

Buckett, M.I. (1991). "Electron irradiation damage in transition metal oxides," Ph.D. thesis, Northwestern University.

Callahan, J.L., Grasselli, R.K., Milberger, E.C., and Strecker, H.A. "Oxidation and ammoxidation of propylene over bismuth molybdate catalysts." *Ind. Eng. Chem. Prod. Res. Develop.* 9 (1970): 134.

Castell, M.R. "Scanning tunneling microscopy of reconstructions on the $SrTiO_3$ (001) surface." *Surf. Sci.* 505 (2002a): 1-13.

Castell, M.R. "Nanostructures on the $SrTiO_3$ (001) surface studied by STM." *Surf. Sci.* 516 (2002b): 33-42.

Chaar, M.A., Patel, D., Kung, M.C., and Kung, H.H. "Selective oxidative dehydrogenation of butane over V-Mg-O catalysts." *J. Catal.* 105 (1987): 483-498.

Chaudhari, P., Koch, R.H., Laibowitz, R.B., McGuire, T.R., and Gambino, R.J. "Critical current measurements in epitaxial films of $YBa_2Cu_3O_{7-x}$ compound." *Phys. Rev. Lett.* 58 (1987): 2687-2686.

Christoskova, S.G., Danova, N., Georgieva, M., Argirov, O.K., and Mehandzhiev, D. "Investigation of a nickel-oxide system for heterogeneous oxidation of organic compounds." *Appl. Cat. A* 128 (1995): 219-229.

Collazo-Davila, C., Grozea, D., and Marks, L.D. "Determination and refinement of the Ag/Si(111)-(3x1) surface structure." *Phys. Rev. Lett.* 80 (1998a): 1678-1681.

Collazo-Davila, C., Landree, E., Grozea, D., Jayaram, G., Plass, R., Stair, P., and Marks, L.D. "Design and initial performance of an ultrahigh vacuum Sample Preparation Evaluation Analysis and Reaction (SPEAR) system." *J. of the Microscopy Society of America* 1 (1995): 267-279.

Collazo-Davila, D., Grozea, D., Marks, L.D., Feidenhans'l, R., Nielsen, M., Seehofer, L., Lottermoser, L., Falkenberg, G., Johnson, R.L., Gothelid, M., and Karlsson, U. "Solution of Ge(111) - (4x4)/Ag structure using direct methods applied to X-ray diffraction data." *Surf. Sci.* 418 (1998b): 395-406.

Cord, B., and Courths, R. "Electronic study of $SrTiO_3$ surfaces by photoemissions." *Surf. Sci.* 162 (1985): 34-38.

Cowley, J.M. "Electron microscopy of surface structure." *Prog. Surf. Sci.* 21 (1986): 209-250.

Dingley, D.J., and Field, D.P. "Electron backscatter diffraction and orientation imaging microscopy." *Mater. Sci. Tech.* 13 (1997): 69-78.

Dingley, D.J., Longden, M.J., Weinbren, J., and Alderman, J. "Online analysis of electron back-scatter diffraction patterns. 1. Texture analysis of zone refined polysilicon." *Scanning Microsc.* 1 (1987): 451-456.

Dunn, D.N., Ai, R., Savage, T.S., Zhang, J.P., and Marks, L.D. "Preparation and detection of reconstructed plan-view surfaces." *Ultramicroscopy* 38 (1991): 333-342.

Erdman, N., Warschkow, O., Ellis, D.E., and Marks, L.D. "Solution of the p(2x2) NiO(111) surface structure using direct methods." *Surf. Sci.* 470 (2000): 1-14.

Erdman, N., Asta, M., Warschkow, O., Ellis, D.E., Poeppelmeier, K.R., and Marks, L.D. "The structure and chemistry of the TiO_2-rich surface of $SrTiO_3$(001)." *Nature* (2002): 55-58.

Feidenhans'l, R. "Surface structure determination by X-ray diffraction." *Surf. Sci. Rep.* 10 (1989): 105-188.

Freund, H.J. "Metal oxide surfaces: electronic structure and molecular adsorption." *Phys. Stat. Sol. B* 192 (1995): 407-440.

Freund, H.J., Kuhlenbeck, H., and Staemmler, V. "Oxide surfaces." *Rep. Prog. Phys.* 59 (1996): 283-347.

Gai, P.L., and Kourtakis, K. "Solid-state defect mechanism in vanadyl pyroposphate catalysts: implications for selective oxidation." *Science* 267 (1995): 661-663.

Gai, P.L., Kourtakis, K., Coulson, D.R., and Sonnichsen, G.C. "HREM microstructural studies on the effect of steam exposure and cation promoters on vanadium phosphorus oxides: New correlations with n-butane oxidation reaction chemistry." *J. Phys. Chem. B* 101 (1997): 9916-9925.

Gao, H.X., Peng, L.M., and Zuo, J.M. "Lattice dynamics and Debye-Waller factors of some compounds with the sodium chloride structure." *Acta Cryst. A* 55 (1999): 1014-1025.

Gao, X.T., Ruiz, P., Xin, Q., Guo, X., and Delmon, B. "Effect of coexistence of magnesium vanadate phases in the selective oxidation of propane to propene." *J. Catal.* 144 (1994): 56-67.

Gibson, A., Haydock, R., and LaFemina, J.R. "Electronic structure and relative stability of the MgO(001) and MgO(111) surfaces." *J. Vac. Sci. Technol. A* 10 (1992): 2361-2366.

Gilmore, C.J., Marks, L.D., Grozea, D., Collazo, C., Landree, E., and Twesten, R.D. "Direct solutions of the Si(111) 7x7 structure." *Surf. Sci.* 381 (1997): 77-91.

Grozea, D., Bengu, E., Collazo-Davila, C., and Marks, L.D. "Structure determination of the Ge(111)-(3x1)Ag surface reconstruction." *Surf. Rev. Lett.* 6 (1999): 1061-1065.

Grozea, D., Landree, E., Collazo-Davila, C., Bengu, E., Plass, R., and Marks, L.D. "Structural investigations of metal-semiconductor surfaces." *Micron* 30 (1998): 41-49.

Hamnett, A., and Goodenough, J.B. "Binary transition metal oxides." In *Physics of non-tetrahedrally bonded compounds*. O. Madelung, ed., Berlin: Springer, 1984.

Harding, W.D., Kung, H.H., Kozhevnikov, V.L., and Poeppelmeier, K.R. "Phase equilibria and butane oxidation studies of the MgO-V_2O_5-MoO_3 system." *J. Catal.* 144 (1993): 597-610.

Heifets, E., Dorfman, S., Fuks, D., Kotomin, E., and Gordon, A. "Atomistic simulation of $SrTiO_3$ (001) surface relaxation." *J. Phys. Cond. Matt.* 10 (1998): L347-L353.

Henrich, V.E. "The nature of transition metal oxide surfaces." *Prog. Surf. Sci.* 44 (1983): 175-199.

Henrich, V.E., and Cox, P.A. *The surface science of metal oxides*. Cambridge: Cambridge University Press, 1994.

Henrich, V.E., Desselhaus, G., and Zeiger, H.J. "Surface defects and the electronic structure of $SrTiO_3$ surfaces." *Phys. Rev. B* 17 (1978): 4907-4921.

http://www.chem.purdue.edu/ccr/v2020/cat.html.

Ikeda, A., Nishimura, T., Morishita, T., and Kido, Y. "Surface relaxation and rumpling of TiO_2-terminated $SrTiO_3$ (001) detrermined by medium ion scattering." *Surf. Sci.* 433-435 (1999): 520-524.

Isabell, T.C., and Dravid, V.P. "Resolution and sensitivity of electron backscattered diffraction in a cold field emission gun SEM." *Ultramicroscopy* 67 (1997): 59-68.

Jayaram, G., Xu, P., and Marks, L.D. "Atomic structure of the Si (001) 2x1 surface." *Phys. Rev. Lett.* 71 (1993): 3489-3492.

Jiang, Q.D., and Zegenhagen, J. "$SrTiO_3$ (001) - c(6x2) : a long range atomically ordered surface stable in oxygen and ambient air." *Surf. Sci.* 367 (1996): L42-L46.

Jiang, Q.D., and Zegenhagen, J. "c(6x2) and c(4x2) reconstruction of $SrTiO_3$ (001)." *Surf. Sci.* 425 (1999): 343-354.

Jonhson, D.A. *Some thermodynamic aspects of inorganic chemistry*. Cambridge: Cambridge University Press, 1982.

Kawasaki, M., Takahashi, K., Maeda, T., Tsuchiya, R., Shinohara, M., Ishiyama, O., Yonezawa, T., Yoshimoto, M., and Koinuma, H. "Atomic control of the $SrTiO_3$ crystal surface." *Science* 266 (1994): 1540-1542.

Kresse, G., and Furthmuller, J. "Efficient iterative schemes for ab-initio total-energy calculations using a plane-wave basis set." *Phys. Rev. B* 54 (1996): 11169-11186.

Kresse, G., and Hafner, J. "Ab-initio molecular dynamics for liquid metals." *Phys. Rev. B* 47 (1993): 558-561.

Krishnamachari, N., and Calvo, C. "Refinement of the structure of $Mg_3(VO_4)_2$." *Canad. J. Chem.* 49 (1971): 1629-1637.

Kumpf, C., Marks, L.D., Ellis, D., Smilgies, D., Landemark, E., Nielsen, M., Feidenhans'l, R., Zegenhagen, J., Bunk, O., Zeysing, J.H., Su, Y., and Johnson, R.L. "Subsurface dimerization in III-V semiconductor (001) surfaces." *Phys. Rev. Lett.* 86 (2001): 3586-3589.

Landree, E., Marks, L.D., Zschack, P., and Gilmore, C. "Structure of the TiO_{2-x}(100)-1x3 surface by direct methods." *Surf. Sci.* 408 (1998): 300-309.

Liang, Y., and Bonnell, D.A. "Atomic structures of reduced $SrTiO_3$ (001) surfaces." *Surf. Sci.* 285 (1993): L510-516.

Liang, Y., and Bonnell, D. A. "Structures and chemistry of the annealed $SrTiO_3$ (001) surface." *Surf. Sci.* 310 (1994): 128-134.

Madelung, E. "The atomic constitution of a crystal surface." *Phys. Z.* 20 (1919): 494-496.

Marks, L.D. "Direct imaging of carbon-coated and clean gold (110) surfaces." *Phys. Rev. Lett.* 51 (1983): 1000-1002.

Marks, L.D. "Registry and UHV transmission electron diffraction of surfaces." *Ultramicroscopy* 45 (1992): 145-154.

Marks, L.D. "Wiener-filter enhancement of noisy HREM images." *Ultramicroscopy* 62 (1996): 43-52.

Marks, L.D. "General solution for three-dimensional surface structures using direct methods." *Phys. Rev. B* 60 (1999): 2771-2780.

Marks, L.D., Bengu, E., Collazo-Davila, C., Grozea, D., Landree, E., Leslie, C., and Sinkler, W. "Direct methods for surfaces." *Surf. Rev. Lett.* 5 (1998): 1087-1106.

Marks, L.D., Erdman, N., and Subramanian, A. "Crystallographic direct methods for surfaces." *J. Phys. Condens. Matter* 13 (2001): 10677-10688.

Marks, L.D., Grozea, D., Feidenhans'l, R., Nielsen, M., and Johnson, R.L. "Au 6x6 on Si(111): Evidence for a 2D pseudoglass." *Surf. Rev. and Lett.* 5 (1998a): 459-464.

Marks, L.D., and Plass, R. "Atomic-structure of Si(111)-(5x2)-Au from high resolution electron microscopy and heavy-atom holography." *Phys. Rev. Lett.* 75 (1995): 2172-2175.

Marks, L.D., Plass, R., and Dorset, D. "Imaging surface structures by direct phasing." *Surf. Rev. Lett.* 4 (1997): 1-8.

Marks, L.D., Sinkler, W., and Landree, E. "A feasible set approach to the crystallographic phase problem." *Acta Cryst.* 55 (1999): 601-612.

Marks, L.D., and Smith, D.J. "Direct surface imaging in small metal particles." *Nature* 303 (1983): 316-317.

Marks, L.D., Xu, P., Dunn, D.N., and Zhang, J.P. "Atomic imaging of surfaces in plan view." *EMSA Bulletin* 22 (1992): 65-69.

Martin-Gonzalez, M.S., Aguirre, M.H., Moran, E., Alario-Franco, M.A., Perez-Dieste, V., Avila, J., and Asensio, M.C. "In situ reduction of (100) $SrTiO_3$." *Sol. State Sci.* 2 (2000): 519-524.

Matsumoto, T., Tanaka, H., Kawai, T., and Kawai, S. "STM-imaging of a $SrTiO_3$ (001) surface with atomic scale resolution." *Surf. Sci. Lett.* 278 (1992): L153-L158.

Matsumoto, T., Tanaka, H., Kouguchi, K., Kawai, T., and Kawai, S. "A scanning tunneling microscopy study of laser molecular beam epitaxy on $SrTiO_3$ (100) surface." *Surf. Sci.* 312 (1994): 21-30.

Mavroides, J.G., Kafalas, J.A., and Kolesar, D.F. "Photoelectrolysis of water in cells with $SrTiO_3$ anodes." *Appl. Phys. Lett.* 28 (1976): 241-243.

Men'shikov, A.Z., Dorofeev, Y.A., Teplykh, A.E., Gizhevskii, B.A., and Mironova, N.A. "Neutron diffraction investigation of structural and magnetic states of lithium-doped antiferromagnet NiO." *Phys. Sol. State* 42 (2000): 315-320.

Mitchell, R. (2002). *Perovskites: Modern and Ancient*. Thunder Bay, Ontartio: Almaz, 2002.

Mitsui, C., Nishiguchi, H., Fuckamachi, K., Ishihara, T., and Takita, Y. "Photocatalytic decomposition of pure water over NiO supported on $KTa(M)O_3$ (M=Ti+4, Hf+4, Zr+4) perovskite oxide." *Chem. Lett.* 12 (1999): 1327-1328.

Naito, M., and Sato, H. "Reflection high-energy electron diffraction study on the $SrTiO_3$ surface structure." *Physica C* 229 (1994): 1-11.

Nassau, K., and Miller, A. E. "Strontium titanate: an index to the literature on properties and the growth of single crystals." *J. Cryst. Growth* 91 (1988): 373-381.

Nishimura, T., Ikeda, A., Namba, H., Morishita, T., and Kido, Y. "Structure change of TiO_2-teminated $SrTiO_3$ (001) surfaces by annealing in O_2 atmosphere and ultra-high vacuum." *Surf. Sci.* 421 (1999): 273-278.

Oliver, P.M., Parker, S.C., and Mackrodt, W.C. "Computer simulation of the crystal morphology of NiO." *Mod. Simul. Mater. Sci. Eng.* 1 (1993): 755-760.

Padilla, J., and Vanderbilt, D. "Ab initio study of $SrTiO_3$." *Surf. Sci.* 418 (1998): 64-70.

Pashley, M.D. "Electron counting model and its application to island structures on molecular-beam epitaxy grown GaAs(001) and ZnSe(001)." *Phys. Rev. B* 40 (1998): 10481-10487.

Plass, R., Egan, K., Collazo-Davila, C., Grozea, D., Landree, E., Marks, L.D., and Gajdardziska-Josifovska, M. "Cyclic ozone identified in magnesium oxide (111) surface reconstruction." *Phys. Rev. Lett.* 81 (1998): 4891-4894.

Pless, J.D., Erdman, N., Ko, D.G., Marks, L.D., Stair, P.C., and Poeppelmeier, K.R. "Large single crystal growth of magnesium orthovanadate, $Mg_3(VO_4)_2$, by the optical floating zone technique." *J. Cryst. Growth and Design* (2002), submitted.

Reimer, L. (1984). *Transmission electron microscopy*. New York: Springer-Verlag, 1984.

Robinson, I.K., and Tweet, D.J. "Surface X-ray diffraction." *Rep. Prog. Phys.* 55 (1992): 599-651.

Rodriguez, J.A., and Goodman, D.W. "High pressure catalytic reactions over single-crystal metal surfaces." *Surf. Sci. Rep.* 14 (1991): 1-107.

Ruddlesden, S.N., and Popper, P. "The compound $Sr_3Ti_2O_7$ and its structure." *Acta Cryst.* 11 (1958): 54-55.

Ruffner, J.A., Sault, A.G., Rodriguez, M.A., and Tissot, R.G. "Deposition and characterization of highly oriented $Mg_3(VO_4)_2$ thin film catalysts." *J. Vac. Sci. Tech. A* 18 (2000): 1928-1932.

Sheldrick, G.M. "SHELX-97." University of Goettingen, 1997.

Shi, A.C., and Wortis, M. "Equilibrium shape of NaCl crystals: a first principles calculation." *Phys. Rev. B* 37 (1988): 7793-7805.

Shwartz, L.H., and Cohen, J.B. *Diffraction from materials*. Berlin: Springer, 1987.

Sinfelt, J.H. "Influence of technology on catalytic science." *Ind. Eng. Chem. Fundam.* 25 (1986): 2-9.

Soenen, V., Herrmann, J.M., and Volta, J.C. "In-situ electrical characterization of magnesium vanadate reference phases (meta-MgV_2O_6, pyro-$Mg_2V_2O_7$, and ortho-$Mg_3V_2O_8$) used in oxidative dehydrogenation of propane to propene." *J. Catal.* 159 (1996): 410-417.

Somorjai, G.A., and Zaera, F. "Heterogeneous catalysis on the molecular scale." *J. Phys. Chem.* 86 (1982): 3070-3078.

Sorensen, O.T. ed. *Non-stoichiometric oxides*. New York: Academic Press, 1981.

Srolovitz, D.J., and Safran, S.A. "Capillary instabilities in thin films." *J. Appl. Phys.* 60 (1986): 247-260.

Szot, K., and Speier, W. "Surfaces of reduced and oxidized $SrTiO_3$ from atomic force microscopy." *Phys. Rev. B* 60 (1999): 5909-5926.

Tanishiro, Y., and Takayanagi, K. "Validity of the kinematical approximation in transmission electron diffraction for analysis of surface structures." *Ultramicroscopy* 27 (1989): 1-8.

Thayer, A.M. "Catalyst suppliers face changing industry." *Chem. Eng. News* 70 (1992): 27.

Tomashpol'skii, Y.Y., Kolotyrkin, I.Y., and Lubnin, E.N. "Thermosimulated segregation on oxide surfaces: Auger spectroscopy and model views." *J. Microsc. Spectrosc. Electron.* 10 (1985): 521-537.

Tomashpol'skii, Y.Y., Lubnin, E.N., Sevost'yanov, M.A., and Kukuev, V.I. "Structure of crystal surfaces of complex oxides (100) $BaTiO_3$, (100), (110) $SrTiO_3$ between room temperature and 1200°C." *Sov. Phys. Crystallogr.* 27 (1981): 691-694.

Twesten, R.D., and Gibson, J.M. "Kinematic analysis of transmission electron diffraction data from Si(111) - 7x7." *Ultramicroscopy* 53 (1994): 223-235.

Vanderbilt, D. "Soft self-consistent pseudopotentials in a generalized eigenvalue problem." *Phys. Rev. B* 41 (1990): 7892-7895.

Venables, J.A., and Harland, C.J. "Electron backscattering patterns - new technique for obtaining crystallographic information in scanning electron microscope." *Philos. Mag.* 27 (1973): 1193-1200.

Ventrice, C.A., Bertrams, T., Hannemann, H., and Brodde, A. "Stable reconstruction of the polar (111) surface of NiO on Au(111)." *Phys. Rev. B* 49 (1994): 5773-5776.

Wang, L.Q., Ferris, K.F., and Herman, G.S. "Interactions of H_2O with $SrTiO_3$(100) surface." *J. Vac. Sci. Tech. A* 20 (2002): 239-244.

Wang, L.Q., Ferris, K.F., Herman, G.S., and Engelhard, M.H. "Interaction of HCOOH with stoichiometric and reduced $SrTiO_3$(100) surfaces." *J. Vac. Sci. Tech. A* 18 (2000): 1893-1899.

Wang, X., Heier, K.R., Stern, C.L., and Poeppelmeier, K.R. "Structural comparison of iron tetrapolyvanadate $Fe_2V_4O_{13}$ and iron polyvanadomolybdate $Fe_2V_{3.16}Mo_{0.84}O_{13.42}$: a new substitution mechanism of molybdenum (VI) for vanadium (V)." *Inorg. Chem.* 37 (1998a): 3252-3259.

Wang, X., Heier, K.R., Stern, C.L., and Poeppelmeier, K.R. "Crystal growth and structure of $Mn_{2.47}V_{0.94}Mo_{1.06}O_8$." *J. Alloys Comp.* 267 (1998b): 79-85.

Wang, X., Zhang, H., Sinkler, W., Poeppelmeier, K.R., and Marks, L.D. "Reduction of magnesium orthovanadate $Mg_3(VO_4)_2$." *J. Alloys Comp.* 270 (1998c): 88-94.

Warschkow, O., Dyke, J.M., and Ellis, D.E. "A divide and conquer impelentation of he discrete variational DFT method for large molecular and solid systems." *J. Comp. Phys.* 143 (1998): 70-89.

Williams, E.D., and Marks, L.D. "New and emerging techniques for imaging surfaces." *Crit. Rev. Surf. Chem.* 5 (1995): 275-303.

Wolf, D. "Reconstruction of NaCl surfaces from a dipolar solution to the Madelung problem." *Phys. Rev. Lett.* 68 (1992): 3315-3318.

Wollast, R., and Taizart, A. *Silicates Ind.* 34 (1969): 42.

Xu, P., Jayaram, G., and Marks, L.D. "Cross-correlation method for intensity measurement of transmission electron-diffraction patterns." *Ultramicroscopy* 53 (1994): 15-18.

Xu, P., and Marks, L.D. "Intensities of surface diffraction spots in plan view." *Ultramicroscopy* 45 (1992): 155-157.

APPENDIX I

Diffraction Data for the NiO (111) - p(2x2) Reconstruction

The table below presents the diffraction rods data (observed, calculated intensities and the error) after the refinement using SHELX-97 program. The data were the source for Figure 7 in the main text. The diffraction data was recorded by Dr. A. Barbier.

Table 13: Grazing incidence X-ray diffraction data for the NiO (111) - p(2x2) reconstruction.

h	k	l	Calculated Intensity	Observed Intensity	Error (sigma)
-1	1	2	2123.92	2747.98	645.94
-1	1	3	2332.32	2724.48	675.87
-1	1	4	2496.44	2701.13	635.36
-1	1	6	2619.09	2525.36	594.46
-1	1	8	2412	2117.68	499.28
-1	1	10	1929.65	1669.67	394.56
-1	1	12	1333.2	1268.44	300.9
-1	1	14	796.71	911.56	217.77
-1	1	16	417.74	518.05	126.23
-1	1	18	194.1	293.81	74.39
-1	1	20	72.49	55.27	19.23
-1	1	24	44.98	40.28	16.7
-1	1	28	442.05	469.84	117.26
-1	1	30	739.4	646.82	159.57
-1	1	32	966.94	723.61	180.96
-1	1	34	1032.94	1338.43	325.74
-1	1	36	919.87	960.2	236.47
-1	1	38	690.73	579.77	146.64
-1	2	3	149.86	238.53	59.31
-2	3	3	1614.91	1573.14	390.7
-3	3	2	161.67	191.3	50.87
-3	3	3	253.66	238.53	66.06
-3	3	4	364.47	458.83	119.34
-3	3	5	489.97	499.77	131.57
-3	3	6	624.57	680.03	175.33

-3	3	7	761.25	729.68	188.41
-3	3	8	892.01	852.79	218.95
-3	3	9	1008.72	932.46	239.07
-3	3	10	1104.21	1189.41	300.17
-3	3	11	1173.29	1142.37	291.01
-3	3	12	1213.54	1502.98	375.54
-3	3	13	1225.55	1356.86	343.47
-3	3	14	1212.67	1402.81	356.39
-3	3	15	1180.15	1413.57	360.51
-3	3	16	1134.04	1005.83	266.83
-3	3	17	1079.9	1240.34	322.43
-3	3	18	1021.78	1134.93	299.15
-3	3	19	961.58	1410.87	360.94
-3	3	20	898.98	1174.63	309.47
-3	3	21	832.06	704.33	203.38
-3	3	22	758.09	1071.29	286.04
-3	3	23	674.87	886.91	245.48
-3	3	25	480.42	788.35	241.59
-3	3	26	375.08	515.38	176.07
-3	3	27	272.13	218.15	110.47
-3	3	28	179.23	220.81	110.41
-3	3	35	163.99	87.75	88.53
-3	3	37	271.3	243.43	133.03
-3	3	38	307.55	370.84	171.07
-3	3	39	326.63	439.16	183.59
-3	4	2	368.52	535.26	134.58
-3	4	3	324.71	516.34	132.72
-3	4	4	286.74	371.85	102.1
-3	4	5	250.9	248.92	74.37
-3	4	6	213.82	157.59	64.87
-3	4	7	173.54	189.38	57.43
-3	4	8	130.19	85.52	40.57
-3	4	9	86.25	50.29	34.98
-3	4	10	46.25	17.07	25.22
-3	4	11	15.99	32.38	23.32
-3	4	12	1.49	24.4	22.16
-3	4	13	7.84	4.33	22.17
-3	4	14	38.1	43.62	30.79
-3	4	15	92.58	83.12	43.88
-3	4	16	168.55	72.82	36.9
-3	4	17	260.46	289.09	97.72
-3	4	18	360.56	349.11	111.95
-3	4	19	459.96	446.88	152.77
-3	4	20	549.74	494.39	158.78
-3	4	21	622.09	645.83	198.26
-3	4	22	671.29	649.17	198.34
-3	4	23	694.27	724.96	223.51
-3	4	24	690.85	746.3	229.56
-3	4	25	663.53	537.38	212.58
-3	4	26	616.99	774.51	229.82

-3	4	27	557.28	548.44	211.78
-3	4	28	490.95	400.13	154.8
-3	4	29	424.18	274.45	114.74
-3	4	30	362.11	314.43	123.72
-3	4	31	308.24	232.97	103.58
-3	4	32	264.32	240.23	105.5
-3	4	33	230.35	295.95	112.86
-3	4	34	204.88	283.15	114.41
-3	4	35	185.5	164.21	83.81
-3	4	36	169.43	172.68	104.82
-3	4	37	154.05	180.12	126.34
-3	4	38	137.47	132.95	75.5
-3	4	39	118.78	34.98	70.17
-3	5	2	479.16	282.44	70.11
-3	5	3	596.38	557.98	137.51
-3	5	4	710.67	613.44	152.14
-3	5	5	807.33	748.11	185.24
-3	5	6	873.26	830.47	205.65
-3	5	7	899.11	880.59	218.38
-3	5	8	880.81	840.91	210.36
-3	5	9	820.13	658.32	168.73
-3	5	10	724.29	712.67	181.48
-3	5	11	604.55	633.25	163.56
-3	5	12	474.27	382.94	104.64
-3	5	13	346.73	330.19	93.73
-3	5	14	233.13	181.61	58.58
-3	5	15	141.13	135.6	47.53
-3	5	16	74.13	99.31	40.31
-3	5	17	31.49	94.94	39.58
-3	5	19	1.8	116.97	46.76
-3	5	20	2.86	3.71	21.64
-3	5	21	7.32	26.82	25.68
-3	5	24	19.55	45.29	32.17
-3	5	26	37.74	8.87	21.83
-3	5	27	56.9	76.97	40.63
-3	5	28	84.24	56.53	37.62
-3	5	29	118.76	75.57	42.26
-3	5	30	157.76	223.31	79.08
-3	5	31	197.29	188.64	71.81
-3	5	32	232.9	237.33	83.52
-3	5	33	260.46	479.4	142.51
-3	5	34	276.96	353.44	113.16
-3	5	35	280.92	509.81	151.89
-3	5	36	272.66	515.51	154.01
-3	5	37	254.02	295.72	102.78
-3	5	38	227.98	475.76	147.1
-3	5	39	198	82.36	51.04
-3	6	3	57.22	26.02	16.56
-3	6	5	74.92	68.44	32.67
-3	6	6	95.8	76.7	37.18

-3	6	7	125.76	123.95	51.33
-3	6	8	163.47	203.51	72.17
-3	6	9	205.82	142.52	62.8
-3	6	10	248.38	280.53	95.15
-3	6	11	286.06	255.62	91.36
-3	6	12	314.02	332.21	112.17
-3	6	13	328.56	318.76	111.8
-3	6	14	327.83	344	121.1
-3	6	15	312.14	249.87	101.37
-3	6	16	283.91	131.52	68.57
-3	6	17	247.25	230.32	100.89
-3	6	18	207.14	189.76	92.46
-3	6	19	168.52	122.65	76.55
-3	6	20	135.41	128.22	79.05
-3	6	21	110.22	163.88	88.58
-3	6	23	83.79	12.74	56.96
-3	6	24	78.52	3.57	78.43
-3	6	26	68.26	35.52	51.59
-3	6	28	44.4	8.94	57.43
-3	6	29	28.06	8.97	60.86
-4	5	2	5.4	5.69	5.93
-4	5	3	18.55	15.96	4.1
-4	5	4	47.65	35.74	24.04
-4	5	5	94.44	124.14	46.8
-4	5	6	158.95	225.04	77.62
-4	5	7	239.02	265.68	88.12
-4	5	8	329.99	525.42	159.59
-4	5	9	425.03	546.48	159.58
-4	5	10	515.82	801.95	233.85
-4	5	11	593.59	1044.3	285.26
-4	5	12	650.42	959.71	255.64
-4	5	13	680.49	1367.96	368.43
-4	5	14	681.05	1046.07	298.74
-4	5	15	652.89	1005.72	289.04
-4	5	16	600.3	822.45	260.07
-4	5	17	530.38	402.1	148.17
-4	5	18	451.98	867.17	265.8
-4	5	19	374.18	700.97	222.11
-4	5	20	304.97	368.91	145.59
-4	5	21	250	528.25	182.41
-4	5	22	211.85	460.4	175.47
-4	5	23	189.9	201.82	98.65
-4	5	24	180.71	316.03	162.78
-4	5	25	178.98	161.03	87.42
-4	5	26	178.8	221.2	128.65
-4	5	27	174.88	56.21	61.41
-4	5	28	163.71	313.68	135.4
-4	5	29	144.27	109.56	77.31
-4	5	30	118.22	106.12	71.54
-4	5	31	89.58	106.01	72.45

-4	5	32	63.9	91.31	194.33
-4	5	33	47.2	55.97	61.13
-4	5	34	44.72	45.81	58.15
-4	5	35	59.94	104.25	87.83
-4	5	36	93.75	166.69	122.06
-4	5	37	144.24	207.89	126.3
-4	5	38	206.88	355.33	193.23
-4	5	39	275.14	313.94	166.27
-4	7	3	435.24	695.23	173.03
-5	5	2	759.97	762.59	202.66
-5	5	3	632.87	620.17	153.97
-5	5	4	490.39	655.98	197.24
-5	5	5	348.8	421.75	146.37
-5	5	6	223.41	244.77	102.42
-5	5	7	126.28	122.63	78.28
-5	5	8	64.55	132.56	89.99
-5	5	9	39.58	103.33	79.33
-5	5	13	166.04	252.96	134.77
-5	5	15	216.86	233.51	140.91
-5	5	16	214.3	86.63	103.85
-5	5	17	194.44	547.98	218.54
-5	5	18	163.42	587.06	234.96
-5	5	19	129.96	267.84	159.81
-5	5	20	103.51	356.99	190.03
-5	5	21	92.34	262.5	168.73
-5	5	22	101.92	869.36	305.88
-5	5	23	133.84	796.62	295.74
-5	5	24	185.53	795.72	300.7
-5	5	25	250.71	1060.21	370.96
-5	5	26	320.51	1032.14	364.91
-5	5	27	385.06	717.81	301
-5	5	28	435.14	855.93	336.48
-5	5	29	463.7	1070.77	392.74
-5	5	30	466.93	689.45	318.87
-5	5	31	444.72	435.36	252.79
-5	5	32	400.42	268.33	218.31
-5	5	33	340.14	319.21	242.95
-5	5	34	271.53	469.25	287.18
-5	5	35	202.45	214.84	212.51
-5	5	36	139.8	189.85	226.67
-5	5	37	88.49	132.81	210.09
-5	5	38	51	101.73	196.24
-5	6	3	336.96	487.3	121.37
-5	7	3	75.18	77.73	21.46
-5	8	3	65.84	152.22	40.59
-5	9	3	124.27	360.13	90.47
-6	7	2	55.24	33.58	15.42
-6	7	3	72.11	251.32	63.54
-6	7	4	92.47	138.56	55.16
-6	7	6	123.2	122.92	55.56

-6	7	8	116.07	234.77	88.3
-6	7	10	70.51	75.69	50.64
-6	7	14	6.9	70.71	58.97
-6	7	16	57.26	164.6	91.78
-6	7	18	156.04	436.62	166.05
-6	7	20	257.26	197.34	113.34
-6	7	22	310.84	348.68	162.16
-6	7	24	292.14	491.7	212.09
-6	7	26	214.66	406.26	195.85
-6	7	28	119.21	453.55	208.54
-6	7	30	48.41	93.76	111.12
-6	7	32	23.41	101.16	113.97
-6	7	34	36.53	123.29	121.5
-6	7	36	61.98	143.21	131.28
-6	7	38	75.35	153.39	138.89
-6	9	3	2.29	55.67	20.85
-6	11	3	166.06	308.25	78.24
-7	7	2	120.49	129.23	40.9
-7	7	3	181.33	305.95	102.39
-7	7	5	308.13	365.38	130.73
-7	7	6	357.49	201.82	95.37
-7	7	7	388.01	568.24	174.34
-7	7	8	395.63	446.11	151.72
-7	7	9	379.56	551.63	176.52
-7	7	10	342.31	496.96	163.93
-7	7	11	289.17	221.66	102.16
-7	7	12	227.2	375.41	133.99
-7	7	13	163.98	44.51	58.39
-7	7	14	106.42	146.72	85.96
-7	7	15	59.7	87.88	77.49
-7	7	16	26.66	3.99	79.64
-7	7	17	7.65	27.8	52.33
-7	7	18	0.84	38.14	58.03
-7	7	24	25.99	113.24	98.56
-7	7	27	21.54	89.86	93.9
-7	7	28	25.98	43.11	72.32
-7	7	29	35.63	17.96	88.33
-7	7	30	50.34	19.23	87.27
-7	7	31	68.83	188.88	121.35
-7	7	32	88.97	119.24	103.77
-7	7	33	108.22	230.74	135.89
-7	7	34	124.04	261.52	146.37
-7	7	35	134.45	114.88	107.77
-7	7	36	138.27	193.06	137.54
-7	7	37	135.31	191.16	140.81
-7	7	38	126.33	336.39	175.36
-7	7	39	112.79	296.27	173.86
-7	8	8	51.28	71.75	57.7
-7	8	10	97.62	204.56	101.53
-7	8	12	136.22	113.68	86.94

-7	8	14	144.73	182.81	113.76
-7	8	18	70.61	116.39	95.68
-7	9	3	236.93	191.37	49.33
-7	11	3	32.21	22.46	15.46
-8	11	3	35.47	109.51	31.84
-9	9	11	48.13	29.5	25.15
-9	9	12	47.89	77.9	39.47
-9	9	13	50.73	60.23	34.95
-9	9	14	57.12	48.8	31.17
-9	9	15	66.95	37.61	28.93
-9	9	16	79.56	75.1	38.93
-9	9	17	93.71	40.24	35.97
-9	9	18	107.74	61.41	42.68
-9	9	22	127.32	76.65	48.78
-9	9	26	64.67	45.32	44.17
-9	9	38	72.5	84.15	70.87
-9	10	20	71.33	217.98	150.11